ORNL/NUREG/TM-147

Heavy-Section Steel Technology Program Quarterly Progress Report for April–June 1977

G. D. Whitman

Prepared for the U.S. Nuclear Regulatory Commission
Office of Nuclear Regulatory Research
Under Interagency Agreements ERDA 40-551-75 and ERDA 40-552-75

OAK RIDGE NATIONAL LABORATORY
OPERATED BY UNION CARBIDE CORPORATION · FOR THE DEPARTMENT OF ENERGY

Printed in the United States of America. Available from
National Technical Information Service
U.S. Department of Commerce
5285 Port Royal Road, Springfield, Virginia 22161
Price: Printed Copy $6.50; Microfiche $3.00

ORNL/NUREG/TM-147
Dist. Category NRC-5

Contract No. W-7405-eng-26

Engineering Technology Division

HEAVY-SECTION STEEL TECHNOLOGY PROGRAM QUARTERLY PROGRESS REPORT FOR APRIL—JUNE 1977

G. D. Whitman

Manuscript Completed — November 23, 1977
Date Published — December 1977

NOTICE: This document contains information of a preliminary nature. It is subject to revision or correction and therefore does not represent a final report.

Prepared for the
U.S. Nuclear Regulatory Commission
Office of Nuclear Regulatory Research
Under Interagency Agreements ERDA 40-551-75 and ERDA 40-552-75

Prepared by the
OAK RIDGE NATIONAL LABORATORY
Oak Ridge, Tennessee 37830
operated by
UNION CARBIDE CORPORATION
for the
DEPARTMENT OF ENERGY

CONTENTS

PREFACE

The Heavy-Section Steel Technology (HSST) Program, which is sponsored by the Nuclear Regulatory Commission (NRC), is an engineering research activity devoted to extending and developing the technology for assessing the margin of safety against fracture of the thick-walled steel pressure vessels used in light-water-cooled nuclear power reactors. The program is being carried out in close cooperation with the nuclear power industry. This report covers HSST work performed April through June 1977, except for subcontractor contributions which may cover the three-month period ending in May. The work performed by Oak Ridge National Laboratory (ORNL) and by subcontractors is managed by the Engineering Technology Division. Major tasks at ORNL are carried out by the Engineering Technology Division and the Metals and Ceramics Division. Prior progress reports on this program are ORNL-4176, ORNL-4315, ORNL-4377, ORNL-4463, ORNL-4512, ORNL-4590, ORNL-4653, ORNL-4681, ORNL-4764, ORNL-4816, ORNL-4855, ORNL-4918, ORNL-4971, ORNL-4655 (Vol. II), ORNL/TM-4729 (Vol. II), ORNL/TM-4805 (Vol II), ORNL/TM-4914 (Vol. II), ORNL/TM-5021 (Vol. II), ORNL/TM-5170, ORNL/NUREG/TM-3, ORNL/NUREG/TM-28, ORNL/NUREG/TM-49, ORNL/NUREG/TM-64, ORNL/NUREG/TM-94, and ORNL/NUREG/TM-120.

SUMMARY

1. PROGRAM ADMINISTRATION AND PROCUREMENT

The Heavy-Section Steel Technology (HSST) Program is an engineering research activity being conducted by the Oak Ridge National Laboratory (ORNL) for the Nuclear Regulatory Commission (NRC) in coordination with other research sponsored by the federal government and private organizations. The program comprises studies relating to all areas of the technology of the materials fabricated into thick-section primary-coolant containment systems of light-water-cooled nuclear power reactors. The principal area of investigation is the behavior and structural integrity of steel pressure vessels containing cracklike flaws. Current work is organized into the following tasks: (1) program administration, (2) fracture mechanics analyses and investigations, (3) effect of high-temperature primary reactor water on the subcritical crack growth of reactor vessel steel, (4) investigations of irradiated materials, (5) pressure vessel investigations, (6) thermal shock investigations, (7) foreign research, and (8) prestressed concrete reactor vessel (PCRV) tendon corrosion studies.

The work performed under the four existing research and development subcontracts is included in this report.

During this quarter, a purchase order was issued to acquire additional A533, grade B, class 1 plate for use as project control material. Also, comments were transmitted to the chairman of the Subcommittee on Nuclear Inservice Inspection on the proposed revisions to the weld repair procedures in Section XI of the ASME Boiler and Pressure Vessel Code. In addition, 15 program briefings or presentations were made during the quarter.

2. FRACTURE MECHANICS ANALYSES AND INVESTIGATIONS

The results to date of photoelastic studies on interior nozzle corner cracks show that the stress-intensity factor distributions along the small flaws are strongly influenced by the inner fillet radius and the resulting high-stress gradient in this region. The stress-intensity factor distributions along moderately deep flaws are influenced by the outer-surface

geometry as well. In deep flaws the outer-surface geometry strongly influences the stress-intensity factor distribution.

3. EFFECTS OF HIGH-TEMPERATURE PRIMARY REACTOR WATER ON THE FATIGUE CRACK GROWTH OF REACTOR VESSEL STEELS

Fatigue crack growth properties of pressure vessel steels are being studied in five environmental chambers. The effects of high ΔK values, cyclic frequency, and ramp and hold time are being investigated. Data are also being obtained on the crack growth rate in weldments.

Results of the first test on a 4T CT specimen were surprising in that significantly lower rates of crack growth were observed with a higher starting ΔK level.

The frequency effect on environmental enhancement of crack growth is believed to be a ramp-time or loading-rate effect, which can best be studied through ramp-time and hold-time tests, and more emphasis is to be placed in this area of investigation.

Crack growth rates observed in weld metal, although somewhat erratic, tend to be lower than those in base metal.

4. INVESTIGATIONS OF IRRADIATED MATERIALS

Analysis of the dosimeters used in the second 4T CT irradiation study has been initiated. Preparations for slow-bend and Charpy impact testing in a hot cell were completed. The assembly of the capsules for the third 4T CT irradiation study is under way.

J-R curve results determined by the unloading compliance method with 0.394T compact specimens agree quite closely with results previously obtained by multiple-specimen techniques. Results from Charpy V geometry specimens tested in four-point bend also showed good agreement. The tests were conducted at 121°C (250°F) on ASTM A533, grade B, class 1 steel.

5. PRESSURE VESSEL INVESTIGATIONS

Preparations for testing intermediate test vessel V-7B are nearly complete with the completion of the flawing, instrumentation, and transport of the vessel to the test site. The restoration work on the test facility has been completed, and the data-acquisition and control systems are being checked prior to the pressure-overload test of the vessel.

Residual stress measurements and material property determinations are being made on in-service repair welds to further characterize the process. This information will be used to establish the feasibility of performing a transition temperature regime test on intermediate test vessel V-8.

A third crack-arrest model was tested. Unstable crack extension occurred without arrest, as expected.

6. THERMAL SHOCK INVESTIGATIONS

Studies were continued to investigate the feasibility of using cryogenic quenching to demonstrate warm prestressing. On the basis of studies conducted to date, it appears that the degree of warm prestressing increases with increasing initial temperature, with ∿130°C (265°F) as an upper limit due to the coating that is applied to the specimen. Analyses made on a 991-mm-OD (39-in.) cylinder, assuming a long axial flaw in quenched and tempered material, indicate that acceptable mimimum values of $(K_I)_{max}/(K_I)_I$ could probably be achieved. The thermal-hydraulic performance of a large specimen is to be checked using a 533-mm-OD (21-in.) cylinder.

7. FOREIGN RESEARCH

Lists of foreign reports published in *Nuclear Safety* through Vol. 18, Issue No. 4 have been reviewed to identify topics of interest in the materials area. Arrangements have been made to obtain translated copies of 18 of these reports.

8. PCRV TENDON CORROSION STUDIES

An analysis of the corrosion of prestressing steel tendons in concrete pressure vessels was completed. Areas in which there is incomplete information on the corrosion of tendon steels are:

1. effect of cathodic polarization, either from internal or external sources, on hydrogen embrittlement;
2. effect of acidifying dilute chloride and sulfate solutions (as would exist in pits) on stress corrosion cracking;
3. general corrosion rate of high-strength steels in dilute aqueous salt solutions and in pure water.

HEAVY-SECTION STEEL TECHNOLOGY PROGRAM QUARTERLY PROGRESS REPORT FOR APRIL—JUNE 1977

G. D. Whitman

ABSTRACT

The Heavy-Section Steel Technology (HSST) Program is an engineering research activity conducted by the Oak Ridge National Laboratory for the Nuclear Regulatory Commission. It comprises studies related to all areas of the technology of the materials fabricated into thick-section primary-coolant systems of light-water-cooled nuclear power reactors. The principal area of investigation is the behavior and structural integrity of steel pressure vessels containing cracklike flaws. Current work is organized into eight tasks: (1) program administration and procurement, (2) fracture mechanics analyses and investigations, (3) effect of high-temperature primary reactor water on subcritical crack growth, (4) investigations of irradiated materials, (5) pressure vessel investigations, (6) thermal shock investigations, (7) foreign research, and (8) prestressed concrete reactor vessel (PCRV) tendon corrosion studies.

Stress-intensity factors at nozzle corner cracks, which are measured using photoelastic models, are strongly influenced by the depth of the crack. Fatigue crack growth in pressure vessel steel is being investigated in water reactor environments to evaluate ramp- and hold-time effects. Preparations for testing irradiated weld metal with low ductile shelf toughness are being made using unloading compliance techniques. Preparations have been completed for the testing of vessel V-7B to validate the strength of a vessel containing a large flaw located in the heat-affected zone of an in-service repair weld. Residual stress levels and material properties are being investigated to determine the feasibility of performing an additional intermediate vessel test to evaluate the integrity of in-service weld repairs in the transition temperature regime. A third crack-arrest model was tested. The feasibility of performing cryogenic experiments with pressure vessel steels in cylindrical geometry to study warm-prestressing effects is being evaluated.

1. PROGRAM ADMINISTRATION AND PROCUREMENT

G. D. Whitman

The Heavy-Section Steel Technology (HSST) Program, which is a major safety program sponsored by the Nuclear Regulatory Commission (NRC), is

concerned with the structural integrity of the primary systems, particularly the reactor pressure vessel, of light-water-cooled nuclear power reactor stations. The structural integrity of nuclear reactor pressure vessels is ensured by designing and fabricating them according to the standards set by the code for nuclear pressure vessels, by detecting flaws of significant size that occur during fabrication and in service, and by developing methods capable of producing quantitative estimates of conditions under which fractures could occur. The program is concerned mainly with developing pertinent fracture technology. It deals with the development of knowledge of the material used in these thick-walled vessels, the rate of growth of flaws, and the combination of flaw size and load that would cause fracture and thus limit the life and/or operating conditions for this reactor plant.

The program is coordinated with other government agencies and the manufacturing and utility sectors of the nuclear power industry in the United States and abroad. The overall objective is a quantification of safety assessments for regulatory agencies, professional code-writing bodies, and the nuclear power industry. Several of the activities are conducted under subcontracts by research facilities in the United States and through informal cooperative efforts on an international basis. Four research and development subcontracts are currently in force.

Administratively, the program is organized into eight tasks, as reflected in this report: (1) program administration and procurement, (2) fracture mechanics analyses and investigations, (3) effect of high-temperature primary water on subcritical crack growth of reactor vessel steel, (4) investigations of irradiated material, (5) pressure vessel investigations, (6) thermal shock investigations, (7) foreign research, and (8) prestressed concrete reactor vessel (PCRV) tendon corrosion studies. The last task, instituted this fiscal year, is included in the HSST program for administrative convenience.

Arrangements have been completed for the procurement of A533, grade B, class 1 plate for use as project control material. This material is 240 mm (9.4 in.) thick and is approximately 3.05 × 3.05 m (10 × 10 ft) square. A block of A533 quenched only plate was sent to David Taylor Naval Research and Development Center for the preparation of twelve 1T

compact specimens to be used for the development of the unloading compliance testing method.

Comments were sent to the chairman of the Subcommittee on Nuclear Inservice Inspection on proposed revisions to the weld repair procedures in Section XI of the ASME Boiler and Pressure Vessel Code.

During this quarter, 15 program briefings, reviews, or presentations were made by the HSST staff at technical meetings and at program reviews for NRC staff or for visitors.

2. FRACTURE MECHANICS ANALYSES AND INVESTIGATIONS

2.1 Stress Intensities for Nozzle Cracks in Reactor Vessels*

C. W. Smith† W. H. Peters†

2.1.1 Introduction

The stress-intensity factor (SIF) determination for a crack emanating from the inside juncture of a reactor vessel cylinder with an inlet nozzle has been a problem in the reactor vessel industry for many years due to the complex and widely varying geometries involved. To date, only approximate analytical solutions (such as those of Hellen and Dowling,[1] Reynen,[2] Broekhoven and Spaas,[3] and Schmitt[4]) are available in the open literature, but substantial additional efforts are also under way.

As a result of the degree of analytical intractability of the problem and the need for experimental correlation of approximate analytical methods, such as finite-element methods (FEM), the authors have undertaken several experimental investigations. The experimental technique employed has been developed by the authors over a period of years[5-12] and consists of a marriage between the "frozen stress" photoelastic analysis of cracked bodies and a simplified digital computer analysis of the experimental data for extracting the SIF.

This study has consisted of two phases to date. The first phase consisted of applying the above technique to a cracked-nozzle geometry identical to that studied by Derby.[13] Results showed good agreement with Derby's residual static strength fracture data, except for shallow flaws (a/T = 0.25) where the SIFs from the present tests were 15% below Derby's results, which showed a scatter of about ±7%. Results of the first phase of the study are found in Ref. 14.

After the Derby residual static strength technique was verified, the present study entered phase II, which involved frozen stress photoelastic

---

*Research performed by the Photoelasticity and Fracture Laboratory in the Engineering Science and Mechanics Dept. at Virginia Polytechnic Institute and State University under Subcontract No. 7015 between Union Carbide Corporation and Virginia Polytechnic Institute and State University.

†Engineering Science and Mechanics Dept., Virginia Polytechnic Institute and State University.

determination of SIF distributions for a scale model of a cracked inlet nozzle for an existing boiling-water reactor vessel design. After a brief review of the analytical phases of the technique, the results to date will be discussed and compared with other studies.

2.1.2 Analytical considerations

One can express the maximum shearing stress in the n-z plane along $\theta = \pi/2$ (Fig. 2.1) near the crack tip in the form:[9]

$$\tau_{max} = \frac{A}{r^{1/2}} + B \ , \qquad (2.1)$$

where $A = K_I/(8\pi)^{1/2}$, K_I = SIF, and B is the leading term of a Taylor Series expansion of the regular stress field near the crack tip. Data are taken along $\theta = \pi/2$, since fringes tend to spread in that direction

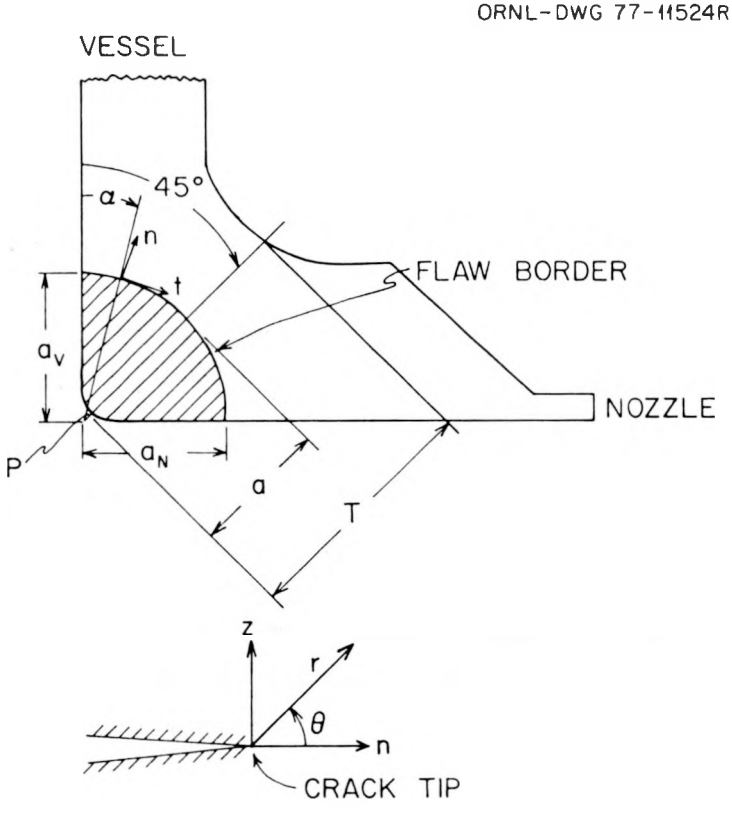

Fig. 2.1. Local problem geometry and notation.

(Fig. 2.2). Then, from the Stress Optic Law,

$$\tau_{max} = \frac{Nf}{2t'} , \tag{2.2}$$

where N is the stress fringe order, f is the material fringe value, and t' is the slice thickness parallel to the crack front, one can determine experimentally the zone in which Eq. (2.1) is valid. This can be done by rewriting Eq. (2.1) in the normalized form:

$$\frac{\tau_{max}(8\pi r)^{1/2}}{p(\pi a)^{1/2}} = \frac{K_I}{p(\pi a)^{1/2}} + \frac{B(8\pi r)^{1/2}}{p(\pi a)^{1/2}} \tag{2.3}$$

or

$$\frac{K_{AP}}{p(\pi a)^{1/2}} = \frac{K_I}{p(\pi a)^{1/2}} + \frac{B(8)^{1/2}}{p}\left(\frac{r}{a}\right)^{1/2} , \tag{2.4}$$

where $K_{AP} = \tau_{max}(8\pi r)^{1/2}$ is defined as the "apparent" SIF and p is the internal pressure. When plotted as $K_{AP}/p(\pi a)^{1/2}$ vs $(r/a)^{1/2}$, Eq. (2.4) yields a straight line which, when extrapolated to the origin, will yield $K_I/p(\pi a)^{1/2}$, the normalized SIF.

The above approach for mode I loading has been extended to cover the mixed mode[6,11] situation also.

In general, when mode I loads are applied to the crack tip, blunting at the crack tip occurs, producing a nonlinear zone that extends roughly out to a distance $r/a = 0.04$ from the crack tip along $\theta = \pi/2$. Moreover, the linear zone described by Eq. (2.4) tends to extend substantially from the crack tip in problems with slowly varying effects along the flaw border (as in the two-dimensional case). Conversely, a constriction of the singular zone occurs in problems with strong three-dimensional effects. However, if a linear zone is present in the raw data plot of normalized apparent SIF vs $(r/a)^{1/2}$, the presence of the desired data zone is assured.

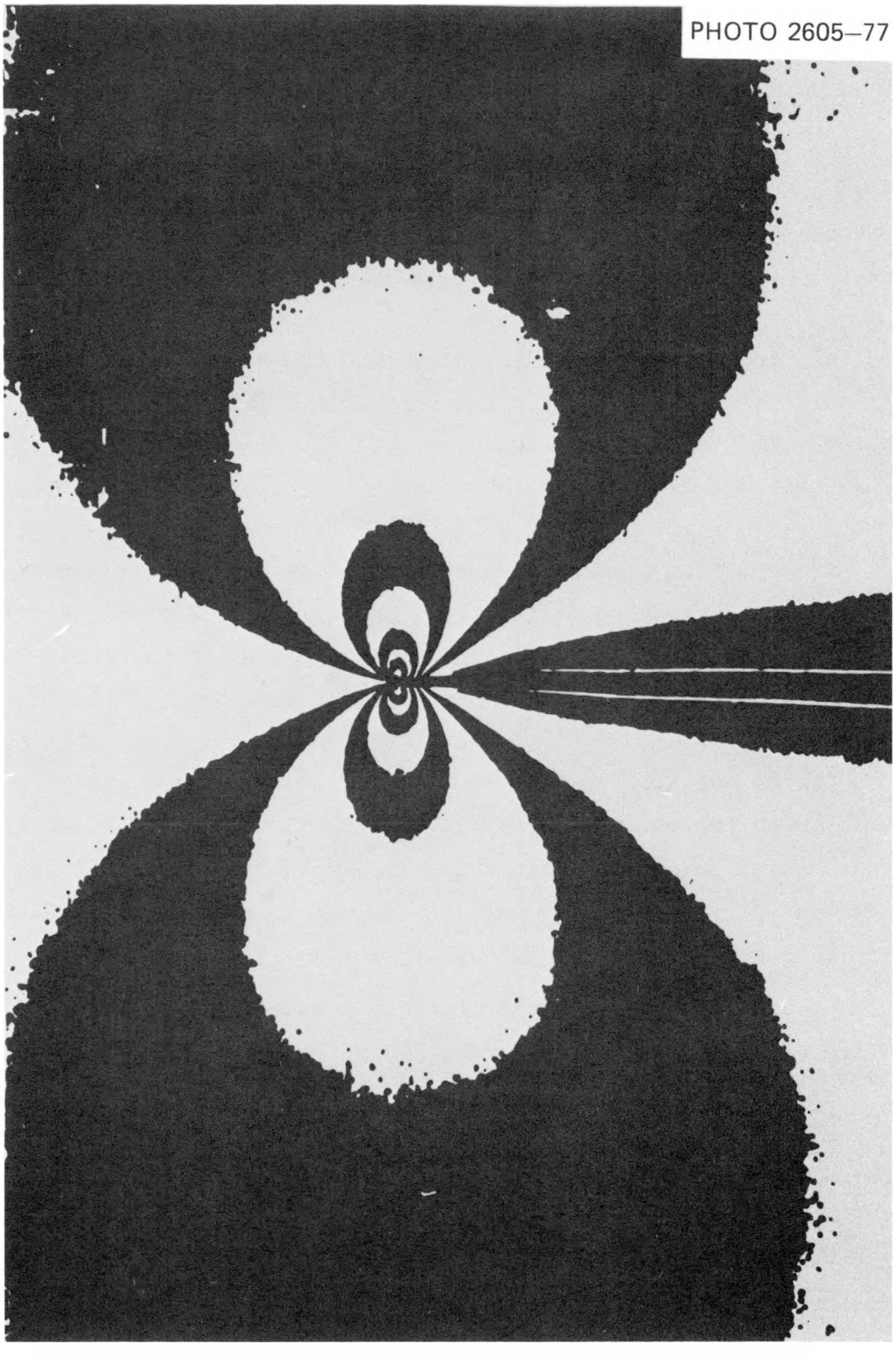

Fig. 2.2. Typical mode I fringe pattern.

2.1.3 Experiments

The present contract calls for the manufacture and testing of a sufficient number of models to accumulate eight valid sets of test data (including near replications) for nozzles of a BWR inlet design containing different size flaws. Model geometry is given in Fig. 2.3, and an assembled model is pictured in Fig. 2.4. Two nozzles are located at diametrically opposite positions on each model. The test procedure is as follows:

1. Starter cracks were introduced into the "inner" surface of the juncture of the vessel wall with the nozzle at point P (Fig. 2.1); then the photoelastic models were glued together and placed in a test rig in a stress-freezing electric oven where they were heated to a critical temperature.

2. The vessels were then pressurized while being supported in soft, surface-matching part-spherical bases. Pressure was increased until the flaws had grown to the desired dimensions, after which the models were cooled under reduced load to room temperature, freezing in both fringe and deformation fields.

3. Slices mutually orthogonal to the flaw border and the flaw surface were then removed at intervals along the flaw border. These slices were coated with a matching refractive index fluid and analyzed via the Tardy method in a crossed circular polariscope at about 10×, utilizing a white-light field and reading tint of passage.

4. Optical data were introduced into a least-squares computer program which extracted estimates of the SIF.

2.1.4 Data and results to date

Three models (six nozzles) have been tested to date. However, the data from one nozzle (nozzle III-B) did not exhibit a linear region (probably because the crack shape was not planar) and were consequently discarded. Data on valid tests obtained to date are given in Table 2.1 (tests IA and IB may be regarded as exact replications.) Figure 2.5 shows a typical set of data, revealing the desired linear zone, and Fig. 2.6 shows the actual flaw geometries studied.

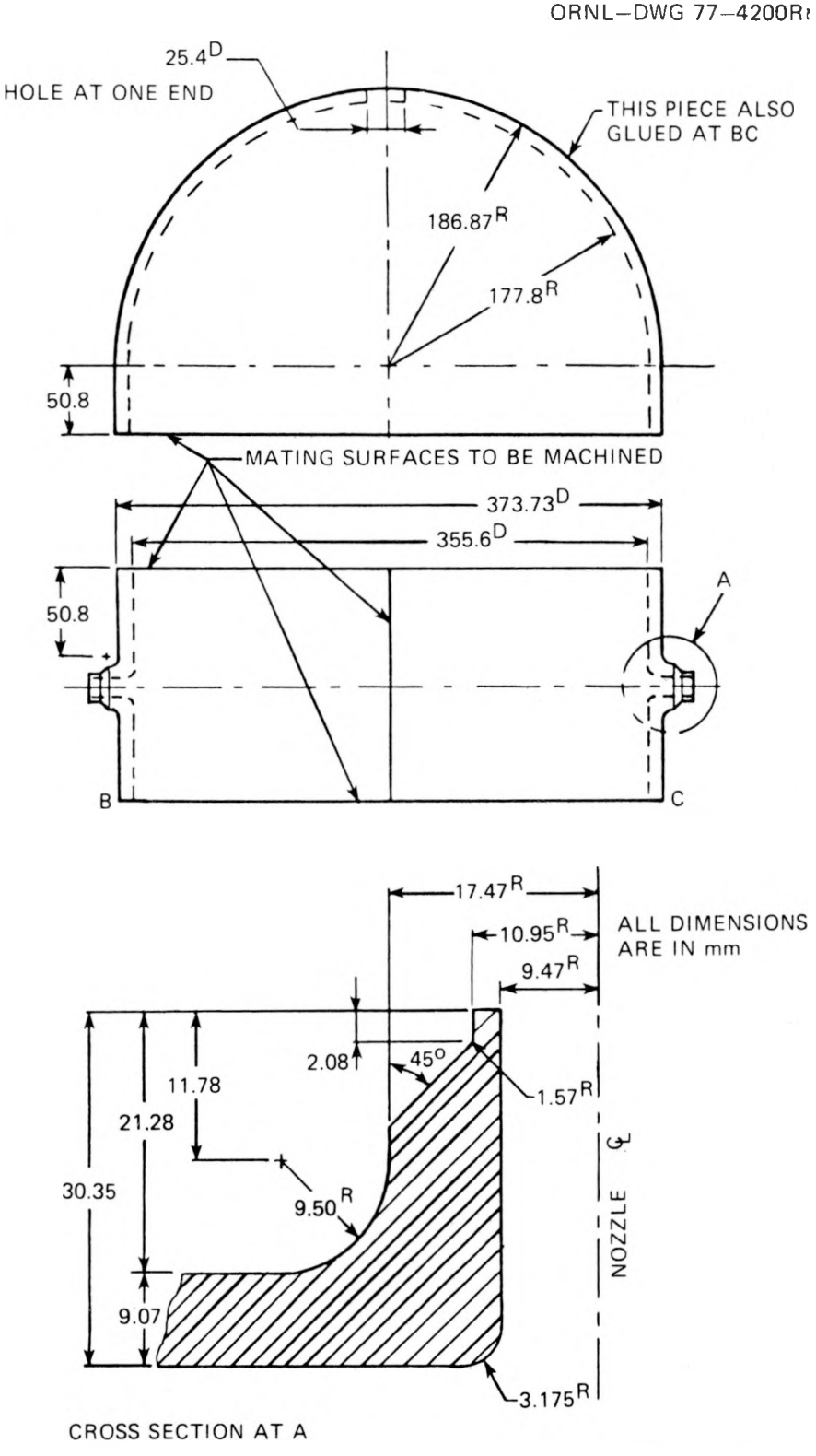

Fig. 2.3. Reactor model and nozzle detail (1 mm = 0.039 in.).

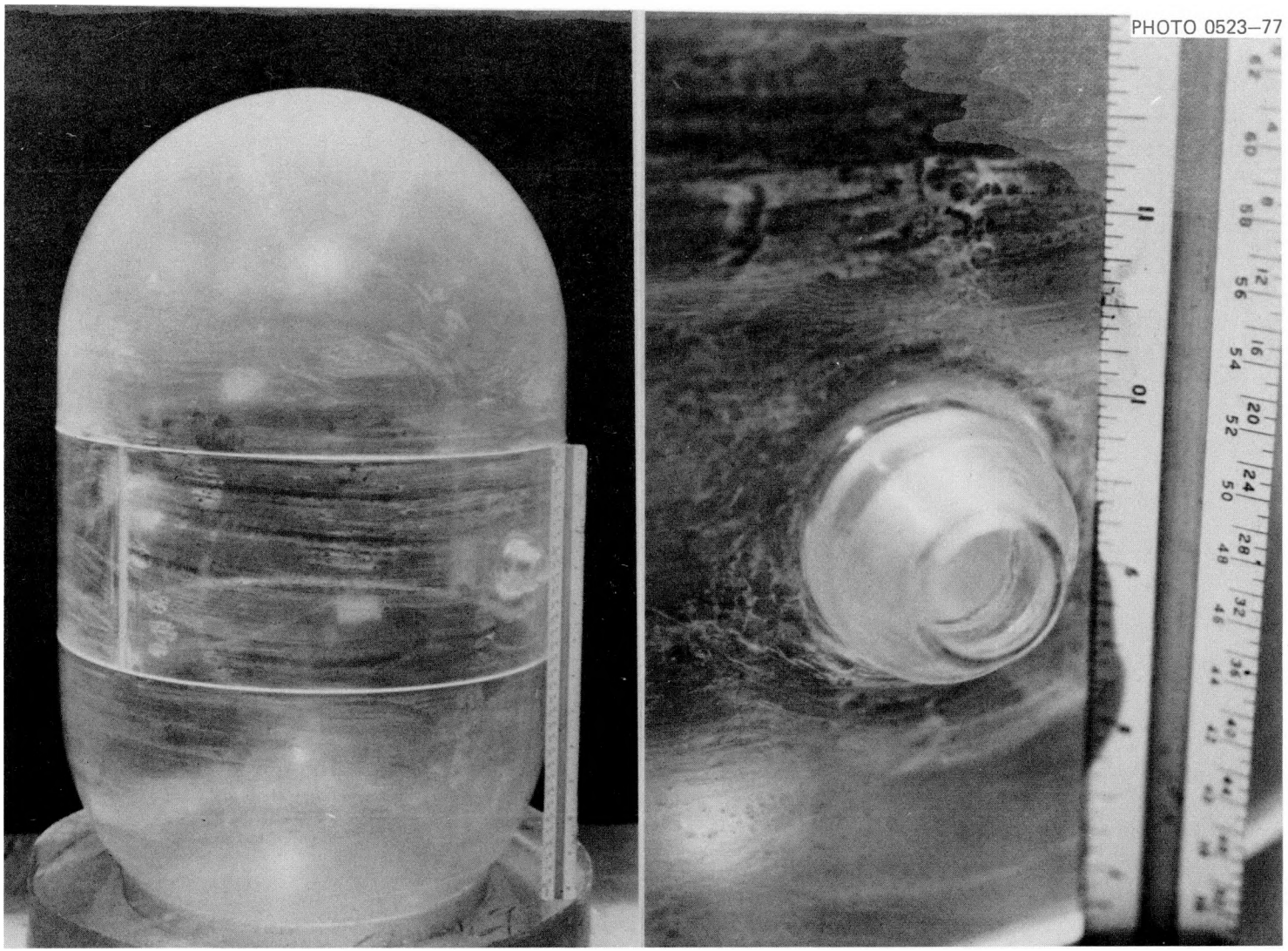

Fig. 2.4. Assembled BWR model and close-up of nozzle.

Table 2.1. Data from tests of six BWR model nozzles[a]

Test[b]	IA	IB	IIA	IIB	IIIA	IIIB[c]
p (kPa)	3.12	3.12	2.76	2.76	2.62	2.62
a_V (mm)	2.54	2.54	10.67	10.16	16.51	6.60
a_N (mm)	4.06	4.06	10.67	10.16	13.72	5.59
a (mm)	2.28	2.28	8.56	7.96	12.19	4.57
a/T	0.15	0.15	0.57	0.53	0.81	0.30

[a]Note that the test (nozzle) designations used in the last progress report (ORNL/NUREG/TM-120) have been changed as follows: 1 has been changed to II and 2 has been changed to III.

[b]T = 15.1 mm for all tests.

[c]Initial flaw inclined to plane of flaw geometry.

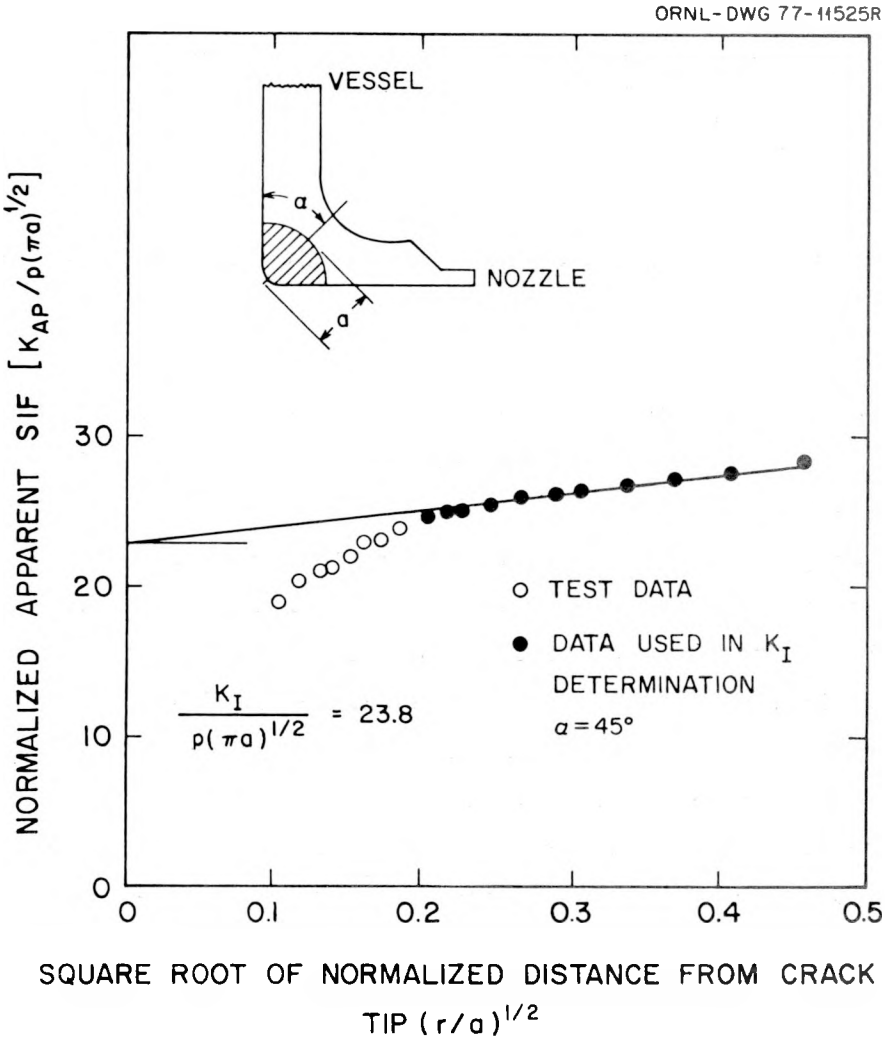

Fig. 2.5. Typical raw fringe data and K_I estimation.

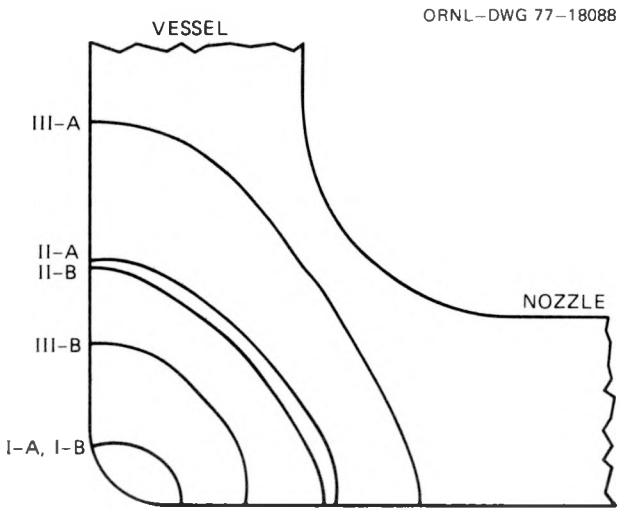

	TEST					
	I-A	I-B	II-A	II-B	III-A	III-B
a_V (mm)	2.54	2.54	10.67	10.16	16.51	6.60
a_N (mm)	4.06	4.06	10.67	10.16	13.72	5.59
a (mm)	2.28	2.28	8.56	7.96	12.19	4.57
a/T	0.15	0.15	0.57	0.53	0.81	0.30

T = 15.1 mm FOR ALL TESTS

Fig. 2.6. Actual flaw geometries for BWR models (1 mm = 0.039 in.).

The SIF distributions obtained to date (Fig. 2.7) are normalized with respect to both p and $\overline{\sigma}$ for comparison with results on the thick-walled vessels (phase I).

These results show the same trends as the results from phase I for the flaws enveloping the inner nozzle fillet, which indicates that the maximum SIF occurs near the center of the flaw border for moderate-to-deep flaws. (The $\overline{\sigma}$ for the thick-walled vessel in Fig. 2.7 is the integrated average Lamé hoop stress across the wall thickness.) These results appear to show that, even for moderately deep flaws, the effects of the back-surface geometry (Fig. 2.8) are less than the T'/r effect in the pressure vessel, which therefore appears to dominate the SIF level in the nozzle. However, for the small cracks where the flaw border begins and/or ends within the inner fillet radius, the flaw shape is different from that of the deep flaws, and the SIF distribution peaks near the nozzle and vessel boundaries. This type of variation has been noted in

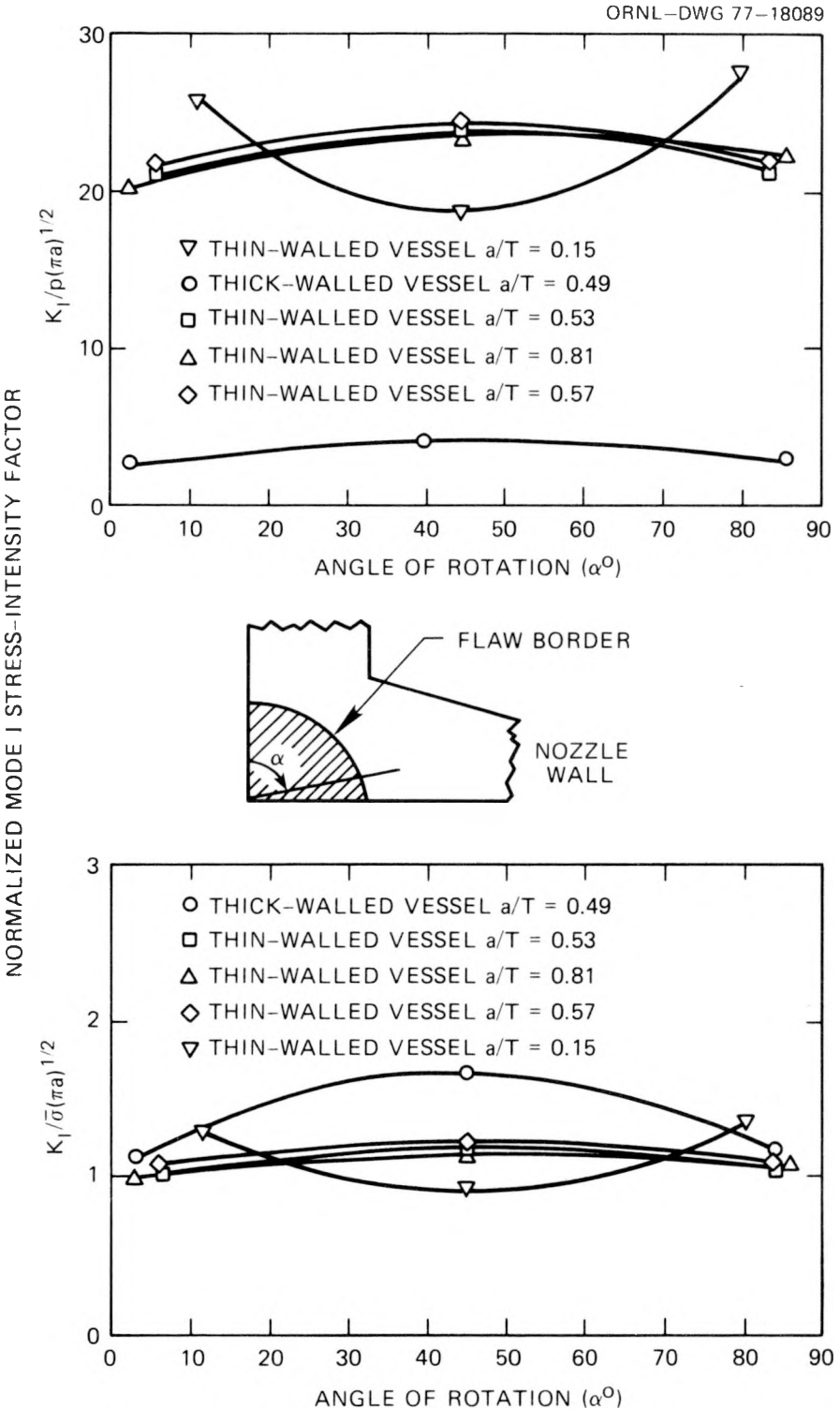

Fig. 2.7. Normalized mode I stress-intensity factor.

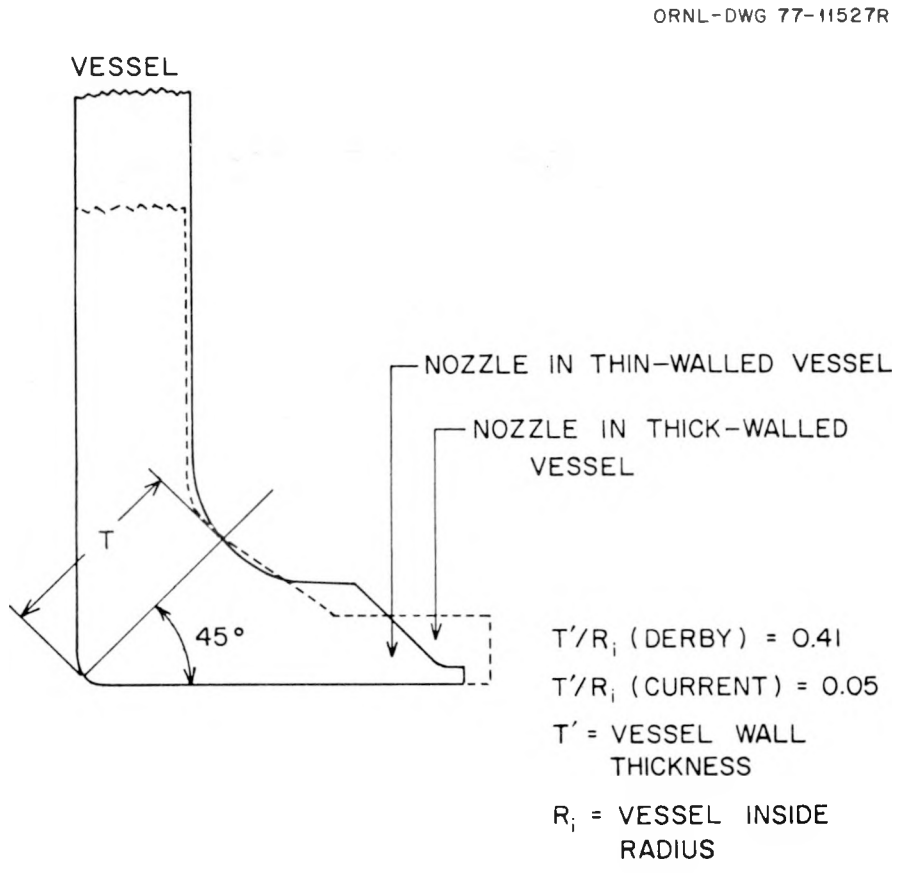

Fig. 2.8. Current geometry and Derby's geometry (Ref. 13) normalized to the same T.

several analytical solutions.[1-3] The writers conclude that the results of phase II to date (Fig. 2.7) imply that very small flaws are quite different from those which are large enough to have grown away from the inner nozzle fillet. We conjecture that the SIF distributions along the small flaws are strongly influenced by the inner fillet radius and the resulting high stress gradient there, while SIF distributions along moderately deep flaws are influenced by the outer-surface geometry as well. It follows that SIF distributions in deep flaws would be expected to be strongly influenced by outer-surface geometry.

The authors wish to emphasize that the above remarks are based upon results from only three sets of data and should be regarded as conjectural pending completion of phase II of the project. Testing of the fourth and fifth models is currently under way.

References

1. T. K. Hellen and A. H. Dowling, "Three Dimensional Crack Analysis Applied to an LWR Nozzle-Cylinder Intersection," *Int. J. Pressure Vessel Piping* 3, 57–74 (1975).

2. J. Reynen, "On the Use of Finite Elements in the Frature Analysis of Pressure Vessel Components," *Trans. ASME, Pressure Vessel Technol.* 98(1), 8–16 (February 1976).

3. M. G. J. Broekhoven and H. A. C. M. Spaas, *Application of the Finite Element Technique to a Complex 3-D Elastic Problem (Nozzle Junction with Cracks)*, Report MMPP101, Laboratory for Nuclear Engineering, Delft University of Technology (August 1974).

4. W. Schmitt et al., "Calculation of Stress Intensity Factors for Cracks in Nozzles," *Int. J. Fract. Mech.* 12(3), 381–90 (June 1976).

5. D. G. Smith and C. W. Smith, "A Photoelastic Investigation of Closure and Other Effects upon Local Bending Stresses in Cracked Plates," *Int. J. Fract. Mech.* 6(3), 305–18 (September 1970).

6. D. G. Smith and C. W. Smith, "Photoelastic Determination of Mixed Mode Stress Intensity Factors," *Eng. Fract. Mech.* 4(73), 357–66 (1972).

7. C. W. Smith, J. J. McGowan, and M. Jolles, "Effects of Artificial Cracks and Poisson's Ratio upon Photoelastic Stress Intensity Determination," *Exp. Mech.* 16(5), 188–93 (May 1976).

8. J. J. McGowan and C. W. Smith, "Stress Intensity Factors for Deep Cracks Emanating from the Corner Formed by a Hole Intersecting a Plate Surface," *Mechanics of Crack Growth*, ASTM STP 590, pp. 460–76, American Society for Testing and Materials, 1976.

9. M. Jolles, J. J. McGowan, and C. W. Smith, "Use of a Hybrid Computer Assisted Photoelastic Technique for Stress Intensity Determination in Three-Dimensional Problems," pp. 63–82, *Computational Fracture Mechanics*, E. F. Rybicki and S. E. Benzley, eds., ASME, New York, 1975.

10. C. W. Smith, M. Jolles, and W. H. Peters, "Stress Intensity Determination in Three-Dimensional Problems by the Photoelastic Method," *Proceedings of the Second International Conference on Mechanical Behavior of Materials*, pp. 235–39, 1976.

11. C. W. Smith, M. Jolles, and W. H. Peters, "Stress Intensities for Cracks Emanating from Pin Loaded Holes," to be published in Proceedings of 10th National Symposium on Fracture Mechanics, 1976.

12. C. W. Smith, M. Jolles, and W. H. Peters, "Stress Intensities in Flawed Pressure Vessels," to be published in Third International Conference on Pressure Vessel Technology, 1977.

13. R. W. Derby, "Shape Factors for Nozzle Corner Cracks," *Exp. Mech.* 12(12), 580–84 (December 1972).

14. C. W. Smith, M. Jolles, and W. H. Peters, *Stress Intensities for Nozzle Cracks in Reactor Vessels*, V.P.I.-E-76-25, 21 pp. (November 1976).

3. EFFECT OF HIGH-TEMPERATURE PRIMARY REACTOR WATER ON THE FATIGUE CRACK GROWTH OF REACTOR VESSEL STEELS*

W. H. Bamford† L. J. Ceschini†
D. M. Moon† K. V. Scott†

3.1 Introduction

The objective of this continuing program is to characterize the fatigue crack growth rate properties of ferritic vessel steels exposed to PWR primary coolant environments. Five environmental chambers continue in use, and the following areas are being investigated:

1. Ramp-time and hold-time effects [2T wedge opening loading (WOL) specimens]	2 chambers [14 MPa, 288°C (2000 psi, 550°F)] 1 chamber [0.14 MPa, 93°C (20 psi, 200°F)]
2. Crack growth rate at high ΔK (4T CT, WOL specimen, 1 cpm)	1 chamber [14 MPa, 288°C]
3. Cyclic frequency effects (2T WOL specimens at 0.1 cpm)	Testing now suspended pending completion of tests on ramp- and hold-time effects
4. Crack growth in weldments (2T WOL specimens)	1 chamber (14 MPa, 288°C)

3.2 Crack Growth Rates at High ΔK Values

The environmental chamber for testing large specimens at high ΔK values has been plagued with hardware problems, but the first test has been completed. The chamber still experienced some sealing problems during this first test, so the environment was maintained at 177°C (350°F) and 14 MPa (2000 psi) rather than the optimum 288°C (550°F). The sealing problems have now been corrected, and the second specimen is now being tested at 288°C and 14 MPa. The first specimen tested (F-23) was a 4T CT specimen made of the same heat of A508 class 2 forging steel as the

*Work sponsored by HSST Program under UCCND Subcontract 3290 between Union Carbide Corporation and Westinghouse Electric Corporation.

†Westinghouse Electric Corporation.

other "F" series specimens previously reported. A sinusoidal tension-tension loading was applied at 1 cpm.

Results of this first test of a 4T CT specimen [4 in. (101.6 mm) thick] revealed a somewhat surprising behavior, as shown in Fig. 3.1. The crack growth rates were found to be significantly slower than other

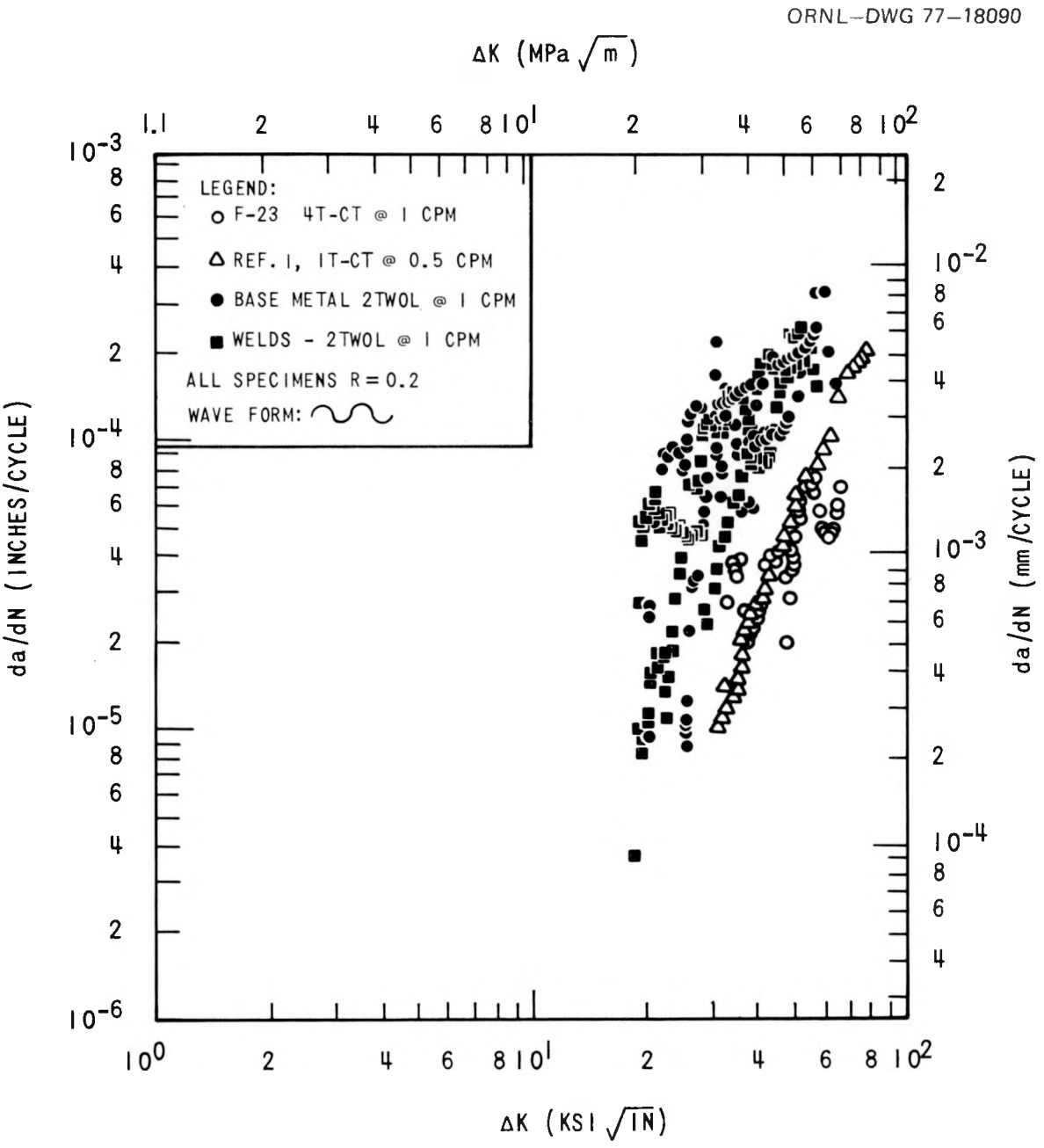

Fig. 3.1. Effect of starting ΔK value on fatigue crack growth in a PWR environment (R = 0.2).

data for smaller specimens at a similar R ratio of 0.2 and the same cyclic frequency. This behavior appears to be caused by the high value of the initial applied ΔK for the test. Consider the other data shown in Fig. 3.1. The majority of the data were produced on 2T WOL specimens, both weld and base metal, a 1 cpm, at a starting ΔK of about 22.1 MPa $\sqrt{m}$ (20 ksi $\sqrt{in.}$). Recent data obtained at the Naval Research Laboratory (NRL) on a 1T CT specimen,[1] also shown in Fig. 3.1, reflect the same initial ΔK effect. Note that this NRL specimen test was begun at a ΔK value of about 33.1 MPa $\sqrt{m}$ (30 ksi $\sqrt{in.}$). The NRL specimen was tested under slightly different conditions (a saw-tooth wave form at 0.5 cpm), but these differences appear to be less influential than the starting ΔK value.

In all cases, the data remain essentially parallel, but in the tests begun at higher ΔK values, the crack growth rate is never able to accelerate to match the environmental enhancement in the tests begun at lower ΔK values. Although this is the first time such behavior has been noted, it can be seen to have occurred in earlier tests, but was not nearly so obvious. Consider, for example, the open circular symbols in Fig. 3.1. These represent two different tests — one started at ΔK = 22.1 MPa $\sqrt{m}$ (20 ksi $\sqrt{in.}$) and another started at ΔK = 27.6 MPa $\sqrt{m}$ (25 ksi $\sqrt{in.}$). Note that the same parallel bahavior is occurring, but is somewhat obscured by the inherent scatter of the data.

The behavior identified here is not well known, but it has occurred in a number of tests at two independent laboratories and could have important consequences. Further testing and study are under way to clarify the phenomenon and adequately explain it. Presently, another 4T CT specimen is being tested under conditions identical to those for specimen F-23, starting at $\Delta K \simeq$ 22.1 MPa $\sqrt{m}$ (20 ksi $\sqrt{in.}$).

It is also noteworthy that specimen F-23 was tested with an internally mounted linear variable differential transformer (LVDT) to monitor crack length. All previous tests have utilized externally mounted LVDT devices, and it may be speculated that the internal LVDT may have contributed somewhat to the larger scatter observed in this first test, as seen in Fig. 3.1. This will be studied during future tests by monitoring the crack length with both internal and external LVDT devices.

3.3 Cyclic Frequency Effects

For a constant-amplitude sinusoidally applied loading, it is now well known that crack growth rates increase as frequency is decreased. A significant increase is observed in changing the frequency from 60 to 1 cpm, which gives the environment more time to influence the crack growth rate. It has long been of interest to determine whether crack growth rates are further enhanced at lower cyclic frequencies, but the required tests are very time consuming. A second low cyclic frequency test has now been completed on specimen F-5 at 0.1 cpm and R = 0.2. Figure 3.2 shows the results of both tests along with the 1-cpm data on 2T WOL specimens shown in Fig. 3.1.

Results show that the two specimens (one A508 forging and one A533B class 1 plate) displayed similar crack growth rates through the range of ΔK of the tests, but in both cases no data were obtained at ΔK values which exceeded 44.1 MPa $\sqrt{m}$ (40 ksi $\sqrt{in.}$). It may be seen from the figure that the crack growth is slightly lower at 0.1 cpm than at 1 cpm, which indicates that a saturation effect has indeed occurred. These conclusions are somewhat clouded by the effect of the starting ΔK, as may be seen from the figure, but it appears that the saturation is real. Studies are now under way to substantiate this statement. This result agrees with data recently published by Atkinson and Lindley,[2] which showed that the maximum environmental enhancement in a material-environment combination very similar to ours occurred at test frequencies from 0.5 to 1 cpm.

It is believed that the so-called frequency effect on environmental enhancement of crack growth is actually a ramp-time or loading-rate effect, which can best be studied through ramp- and hold-time tests, so more emphasis is now being placed on this subject area.

3.4 Crack Growth in Weldments

One further test has been completed on a 2T WOL specimen taken from a production weldment of A533B class 1 plate material. The weldment was made by the submerged-arc process and was described fully in the previous quarterly progress report.[3] The specimen, C-5, was tested under a sinusoidal tension-tension loading at a value of R (K_{min}/K_{max}) equal to 0.2.

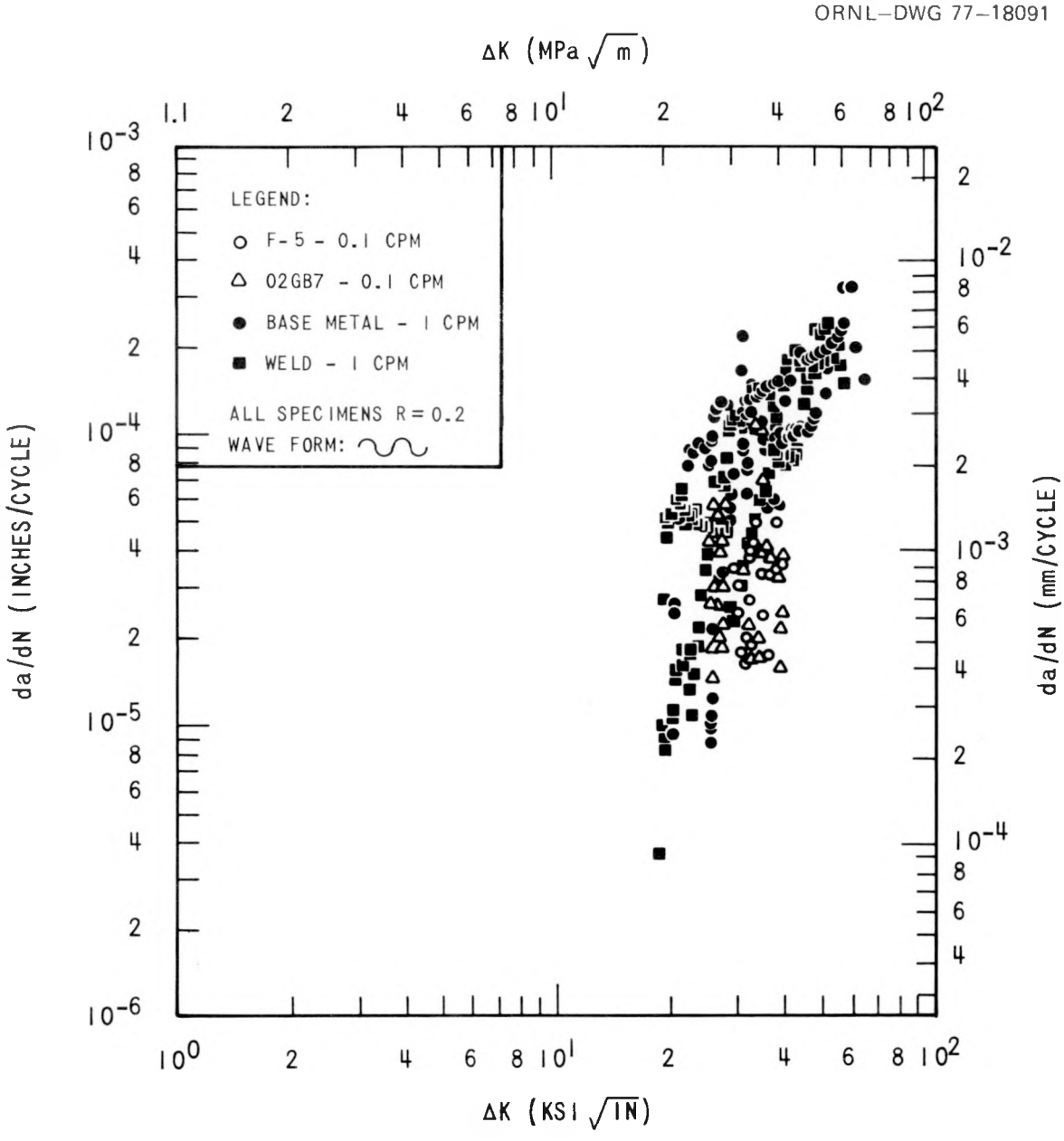

Fig. 3.2. Effect of cyclic frequency on fatigue crack growth in a PWR environment (R = 0.2).

The test was conducted at a cyclic frequency of 5 cpm, and results are presented in Fig. 3.3.

Results of this test are very similar to two previous tests conducted under the same conditions,[3] as shown in Fig. 3.4, with the crack growth rate showing a number of small reversals while continuing the upward trend

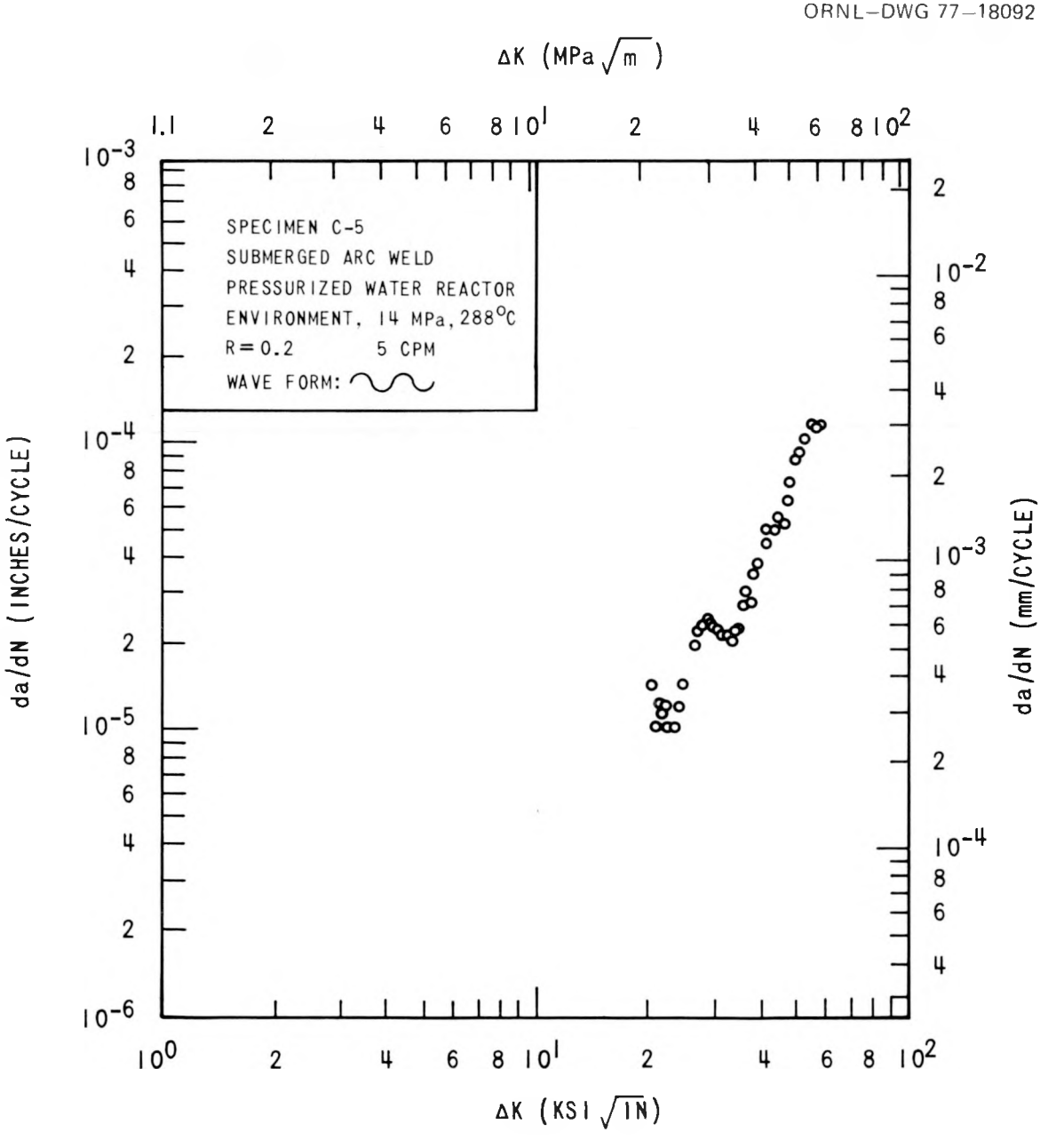

Fig. 3.3. Fatigue crack growth results for specimen C-5.

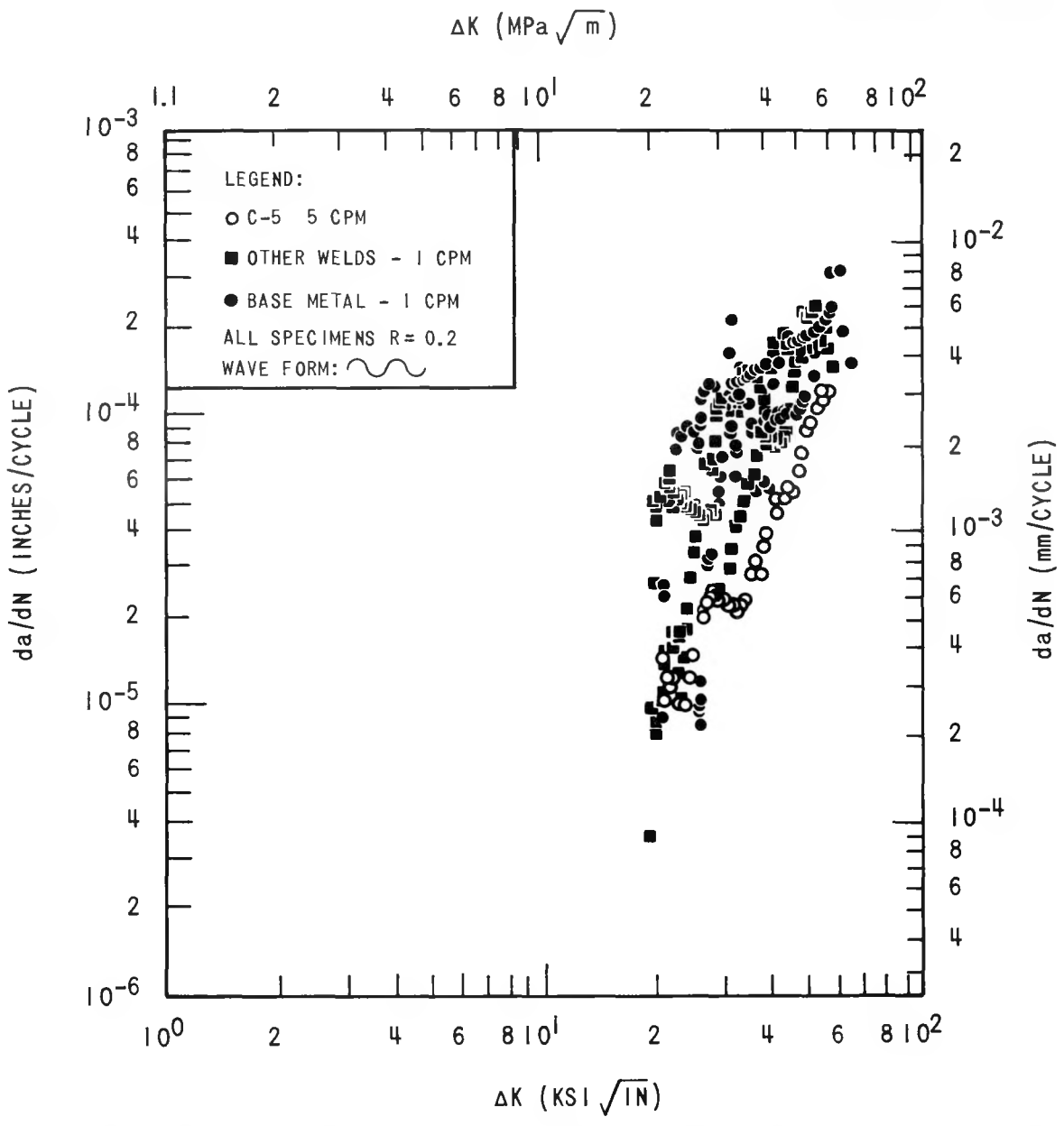

Fig. 3.4. Comparison of weld and base metal crack growth rate results — low R ratio.

as ΔK increases. The crack growth rate data for specimen C-5 fall somewhat lower than that for the other welds, since this test was conducted at 5 cpm as opposed to 1 cpm for the earlier tests. This shows the same trend as previous tests of base metal specimens have shown; that is,

the crack growth rate decreases with an increase in cyclic frequency, which gives the environment less time to influence the crack growth.

3.5 Ramp- and Hold-Time Effects

This area of investigation involves a series of tests with trapezoidal loading forms consisting of programmed ramp and hold times, as summarized in Table 3.1. Identical tests are being conducted at NRL in tandem with this investigation, and the results are being compared as a check on consistency. Results of test series "a" showed excellent agreement between the two laboratories, and so the very long tests planned under "c" and "d" will be split between the two laboratories.

Table 3.1. Projected ramp-time and hold-time tests of 2T WOL specimens in PWR environment, A508 class 2 forging material

Test[a]	Ramp time (min)	Hold time (min)
2a1	Rapid (1 sec)	1
2a2	Rapid (1 sec)	3
2a3	Rapid (1 sec)	12
2a4	Rapid (1 sec)	60
2b1	1	1
2b2	1	3
2b3	1	12
2b4	1	60
2c1	5	1
2c2	5	3
2c3	5	12
2c4	5	60
2d1	30	1
2d2	30	3
2d3	30	12
2d4	30	60

[a]Tests 2a4, 2b4, 2c3, 2c4, 2d2, 2d3, 2d4, which are very long time tests, will be conducted after the others are complete.

At the present time, tests are under way on part "b" of the test series. Some of the tests have been completed, but further studies are under way to ensure that any effect of starting ΔK does not influence the conclusions reached. A complete summary of the results of part "b" will appear in the progress report for next quarter.

3.6 Fatigue Crack Growth in a Hydrogen Sulfide Environment

Since the fatigue crack growth rate tests in a PWR environment require extremely long test times, it would be extremely advantageous to find another test medium which would produce the same environmental effect in a shorter time. Since the primary mechanism in the fatigue process in a PWR environment is believed to be hydrogen embrittlement, a medium which provides free hydrogen in a similar manner to the water environment is required. Pure hydrogen gas is a possibility, but extreme care is necessary to ensure the purity of the hydrogen test environment. A better candidate may be hydrogen sulfide gas (H_2S), which is much easier to use experimentally and involves a reaction with the iron in the steel that is similar to that which occurs in a water environment:

In water: $y\ H_2O + x\ Fe \rightarrow Fe_xO_y + y\ H_2$,

In H_2S: $H_2S + Fe \rightarrow FeS + H_2$.

Three pilot tests have been completed on 2T WOL specimens in an environment of 60 psi H_2S, and the results show behavior which is remarkably similar to that in a water environment. The tests each required about two to three days to complete, as compared with two to three months for a test in the water environment.

Results of two of the tests are shown in Fig. 3.5. These tests were conducted under a sinusoidal tension-tension loading with an R ratio equal to about 0.1 and were done at a frequency of 60 cpm. The two tests were identical except that one was conducted at room temperature and the other at 93°C (200°F). The crack growth data show a definite temperature dependence, with the room-temperature test results following the data for

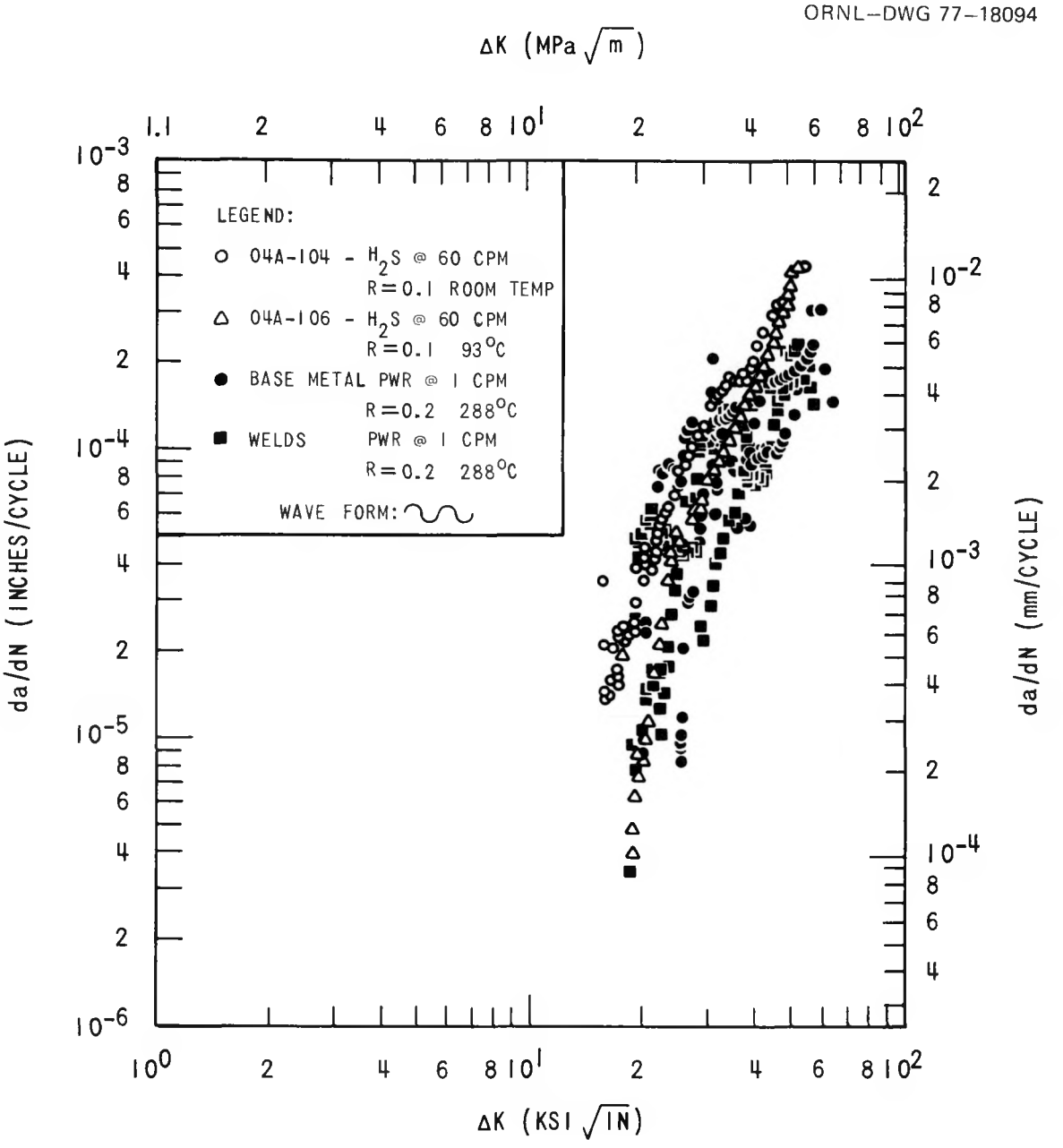

Fig. 3.5. Comparison of fatigue crack growth in pressure vessel steels in hydrogen sulfide and in a PWR environment — low R ratio.

similar tests in a PWR environment rather well. The H_2S data show a somewhat curved behavior through the low and intermediate ΔK range, as do the PWR data, but at the higher ΔK values the PWR data bend over significantly, while the H_2S data continue upward. The H_2S data also show

significant crack growth rate reversals at the beginning of each test, a behavior which is at present unexplained.

A third test was conducted in the same H_2S environment at an R ratio equal to 0.7, and results are compared with similar PWR data in Fig. 3.6.

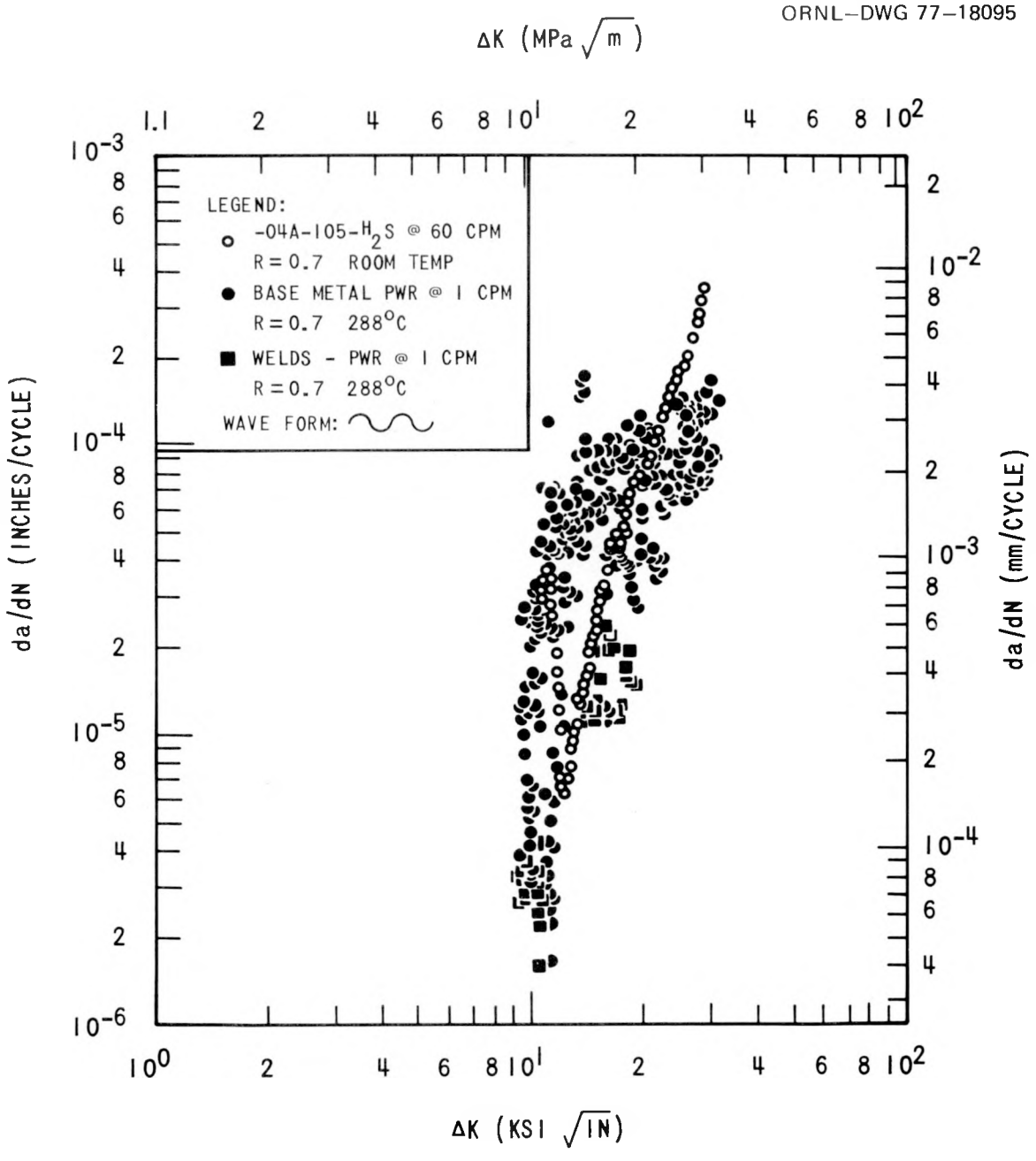

Fig. 3.6. Comparison of fatigue crack growth in pressure vessel steels in hydrogen sulfide and in a PWR environment — high R ratio.

Note that in this test the initial crack growth rate reversal is extremely pronounced, but again the data after the reversal follow approximately through the center of the PWR data.

A study of the fracture surfaces of the H_2S specimens shows a mixture of cleavage and ductile striations, as pictured in Fig. 3.7. Studies are

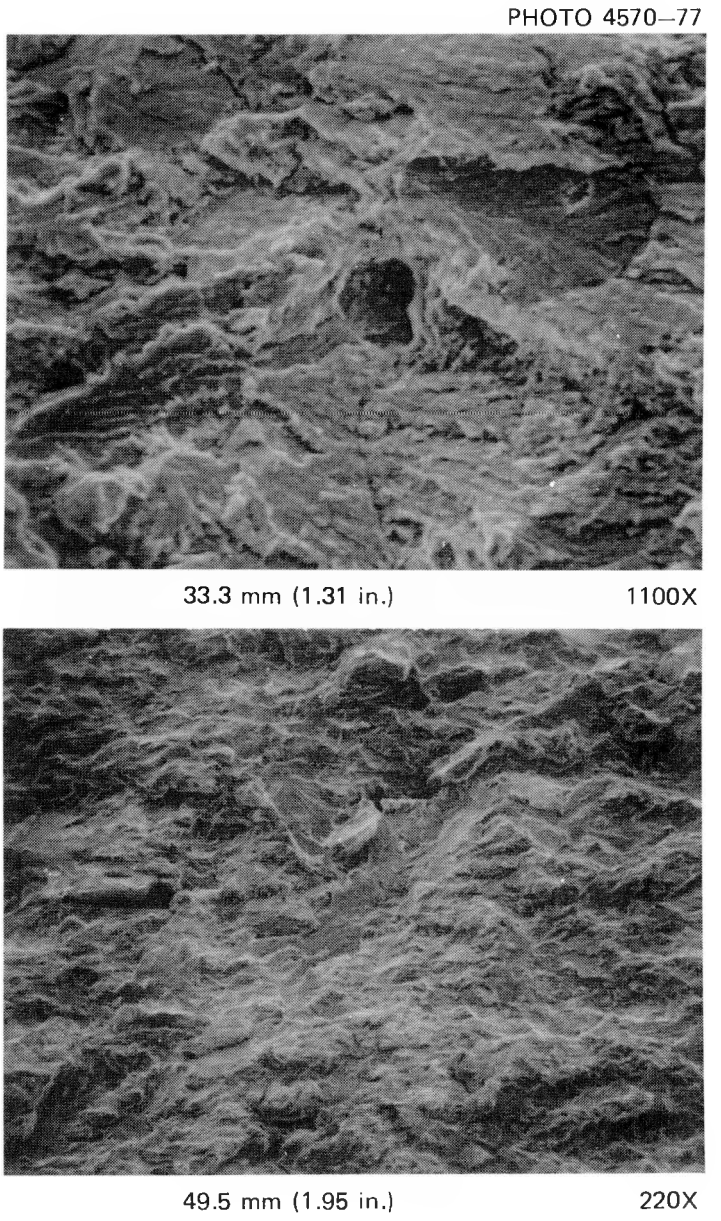

Fig. 3.7. Fracture surface of specimen 04A-106 (A533B class 1 plate).

in progress to measure the striation spacing in these specimens and determine the amount of crack growth enhancement that is due to cleavage. In previous specimens tested in a PWR environment, no incidence of cleavage-type cracking was noted, all the crack growth being accounted for by ductile striations. This result suggests that the very high concentration of hydrogen produced in the specimen by the H_2S environment alters the mechanism of crack growth and may not be typical of the processes occurring in a PWR water environment.

Results of this pilot study of crack growth in an H_2S environment indicate that there are many similarities between the crack growth data produced in an H_2S environment and that produced in a PWR environment. Because of the enormous time savings in the testing process, the H_2S environment could be a valuable tool in studying certain parameters in the present testing program; but it is precisely because of the difference in kinetics and mechanisms of the crack growth process that great care should be exercised in such studies.

References

1. H. E. Watson, F. L. Loss, and B. H. Menke, "Fatigue Crack Propagation in LWR Materials," in *Structural Integrity of Water Reactor Pressure Boundary Components — Progress Report Ending May 31, 1977*, Naval Research Laboratory, Washington, D.C.

2. J. D. Atkinson and T. C. Lindley, "The Effect of Frequency and Temperature on Environmentally Assisted Fatigue Crack Growth Below K_{ISCC} in Steels," in *The Influence of Environment on Fatigue*, Institute of Mechanical Engineers, London, 1977.

3. G. D. Whitman, *Heavy-Section Steel Technology Program Quart. Prog. Rep. January–March 1977*, ORNL/NUREG/TM-120.

4. INVESTIGATION OF IRRADIATED MATERIALS

4.1 Toughness Investigations of Irradiated Materials

R. G. Berggren T. N. Jones D. A. Canonico

Following the completion of irradiation on Mar. 23, 1977, of the three capsules comprising the second 4T CT irradiation study,[1] the capsules were stored in the Bulk Shielding Reactor (BSR) pool for one month to permit decay of the shorter half-life activities. The capsules were then disassembled in a hot cell, and the positions of specimens and dosimeters in the capsules were verified. Analyses of the dosimeters and the temperature history are in progress.

Preparations for slow bend and Charpy impact testing in a hot cell were completed, and a sufficient number of unirradiated (control) specimens are on hand to initiate the testing program. Assembly of the irradiation capsules for the third 4T CT irradiation study is under way, with one capsule nearing completion.

4.2 Assessment of the Ductile Fracture Toughness of Pressure Vessel Steel Using Small Specimens*

J. A. Williams† W. J. Mills†

4.2.1 Introduction

The HSST Small Specimen Utilization (SSU) Program has the objective of determining the degree to which small specimens can be employed in assessing the ductile fracture toughness of irradiated pressure vessel steels for use in reactor safety analysis. The current work of this Hanford Engineering Development Laboratory (HEDL) program is to develop fracture mechanics testing methodology for assessing ductile fracture toughness properties of J_{Ic} at initiation and crack extension by the R curve. Two aspects of ductile fracture toughness characterization were investigated

*Research performed under Purchase Order 11Y-50917V for the Oak Ridge National Laboratory, operated by Union Carbide Corporation under contract to the U.S. Energy Research and Development Administration.

†Hanford Engineering Development Laboratory.

during the past quarter: these were initial tests on ASTM A533-B1 using the unloading compliance method for J-R curve development and the use of precracked Charpy V geometry specimens for developing R curve information.

4.2.2 J-R curve methodology using 0.394T compact specimens in the unloading compliance method to assess ductile fracture toughness of ASTM A533-B1

Unloading compliance test methods as described by Clarke et al.[2] were used to determine the J-R curve for ASTM A533-B1. The material was from HSST plate 02, oriented in the TR direction, and was tested at a temperature of 121°C (250°F). The specimens were 0.394T compact specimens.

The tests were conducted using dual LVDT load-line extensometers, which are described in detail in Ref. 3. Grips with round holes and subsize [4.7 mm (0.185 in.)] pins were used for loading. Loading was by stroke control using a closed-loop electrohydraulic test machine. The extensometer was calibrated to better than 1.27×10^{-3} mm (5×10^{-5} in.), NBS traceable, to produce accurate load-deflection records needed to determine changes in compliance due to crack extension. The measured crack extensions, fatigue and ductile, were determined after testing by heat-tinting the specimen and then fracturing it at subzero temperature. A nine-point average of the crack fronts was used to determine initial and final crack lengths.

Dual chart recordings were made to collect data. One X-Y chart was set to record overall load and overall load-line deflection for J-integral determination, while the second was scaled to read only the periodic unloading cycle for compliance measurement. For the unloading cycle details, the recorder was set to record 0.0127 mm (0.0005 in.) load-line deflection per 25.4 mm (1 in.) of chart and 9.08 kg (20 lb) load per 25.4 mm of chart. Unloading cycles were conducted at approximately every 0.13 mm (0.005 in.) to 0.26 mm (0.010 in.) of load-line displacement. Multiple loadings and unloadings were conducted in the elastic region to determine the initial compliance, c_0, corresponding to a_0, the initial crack length.

The load-deflection curve for specimen 02GA 51-1 is shown in Fig. 4.1; the curve for the second specimen was similar except that deflection was extended beyond maximum loading to 1.78 mm (0.070 in.). The J-integral was determined for the area under the curve at each unloading step. For

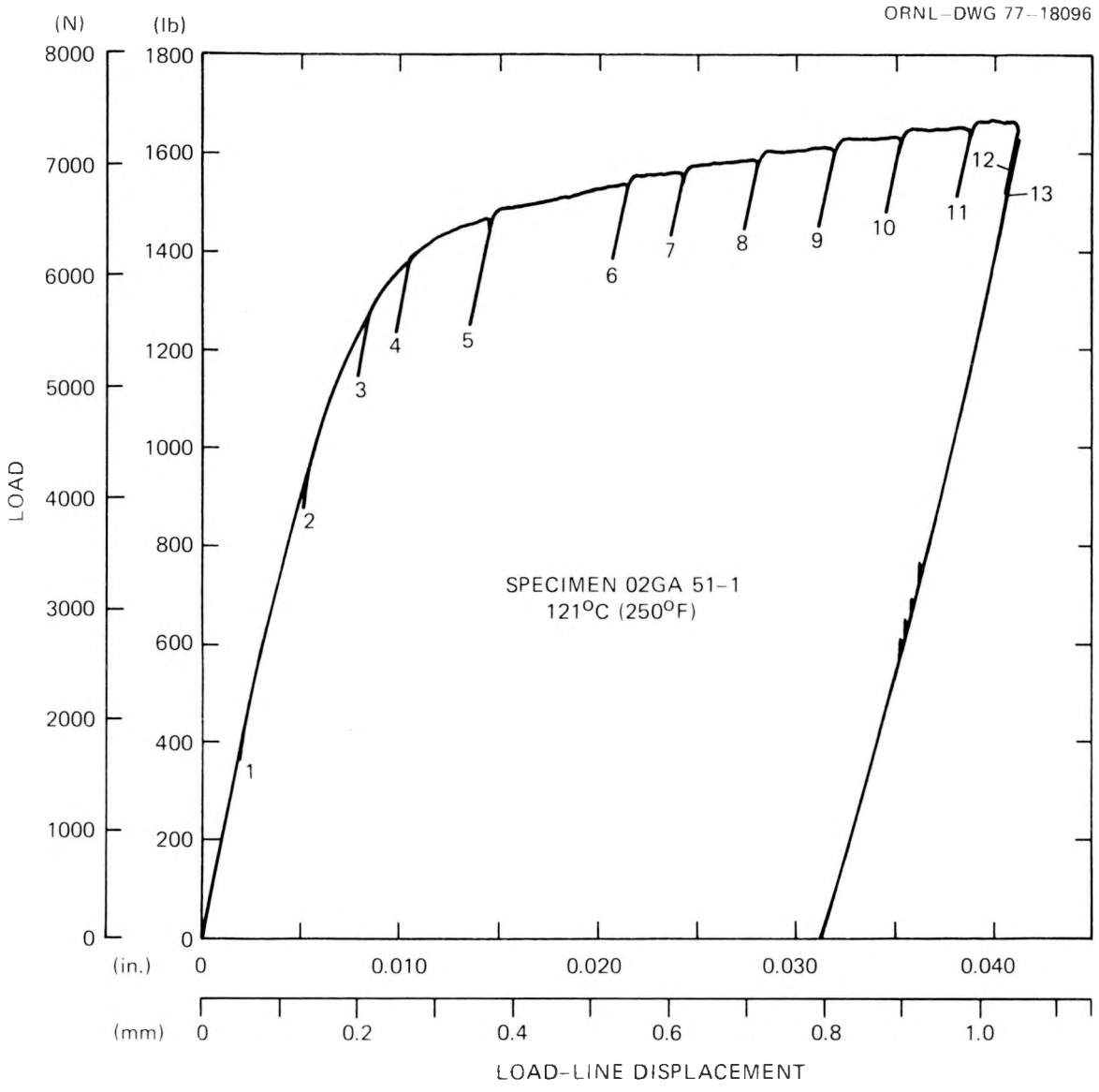

Fig. 4.1. Test record for the unloading compliance method of determining J-R curve of ASTM A533-B1. A second record is used to record the details of each unloading cycle and calculate compliance. (1 in. = 25.4 mm; 1 lb_f = 4.448 N.)

each unloading, crack extension, Δa, was calculated[2] by

$$\Delta a = \frac{W - a_0}{2} \frac{\Delta c}{c_0} ,$$

where $W - a_0$ is the ligament length and Δc is the change in compliance from c_0.

Subsequently, the J-R curve of Fig. 4.2 was constructed. The data are in excellent agreement[4] with multiple-specimen data reported previously. In the crack-blunting region, the initial negative Δa determined is not unique to this study; also, absolute calculated accuracy appears limited to approximately ±0.05 mm (0.002 in.), and equivalent accuracy should be expected at longer crack extensions. Crack lengths were calculated and compared to those measured to assess the accuracy of the compliance measurements. The results shown in Table 4.1 indicate agreement between calculated and measured values to within 3 to 4% for the initial and final crack lengths.

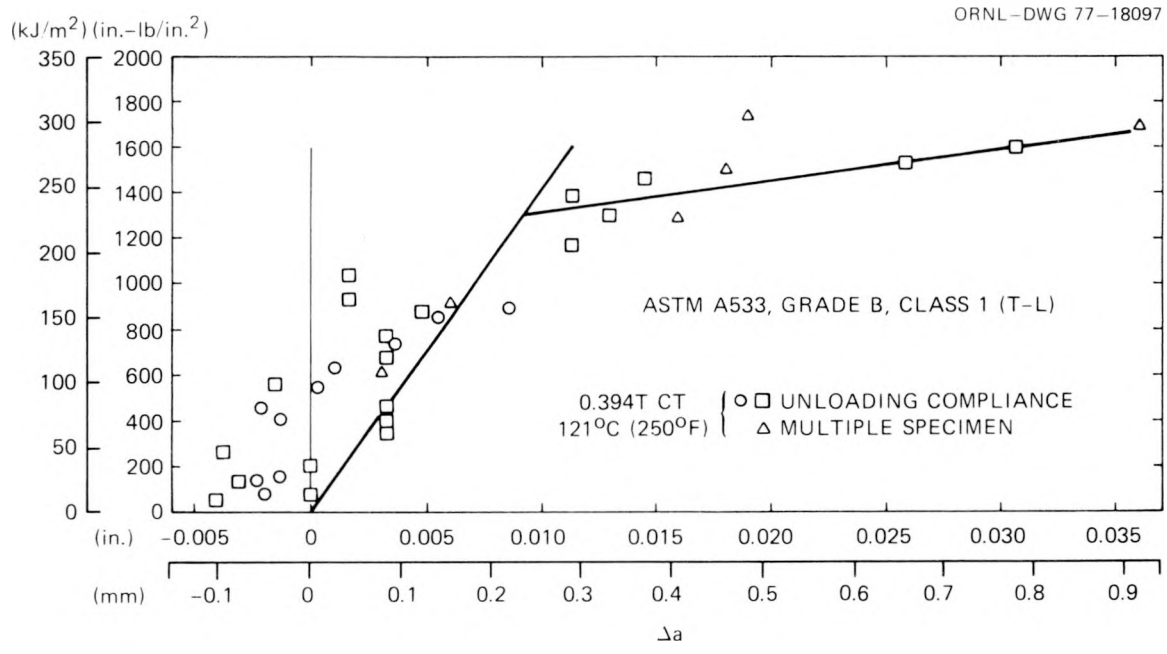

Fig. 4.2. J-R curve for ASTM A533-B1 compared for multiple-specimen and unloading compliance techniques for 0.394T compact specimens tested at 121°C (250°F). (1 in. = 25.4 mm; 1 in.-lb/in.^{2} = 175.13 J/m^2.)

4.2.3 Ductile fracture toughness determinations using Charpy geometry bend specimens

The current investigation was undertaken to develop a technique for determining the J_{Ic} and R curve fracture toughness information on ASTM A533, grade B, class 1 (HSST plate 02) pressure vessel steel using precracked Charpy specimens. The intial bend specimens being tested are

Table 4.1. Comparison of measured and calculated crack lengths from unloading compliance J-R curve test

Material: ASTM A533, grade B, class 1
Test temperature: 121°C (250°F)
Specimen size: 0.394T CT

	Specimen 51-1	Specimen 51-2
Crack length [mm (in.)]		
Calculated		
Initial	11.51 (0.453)	11.63 (0.458)
Final	11.68 (0.460)	12.34 (0.486)
Change	0.18 (0.007)	0.71 (0.028)
Measured		
Initial	11.91 (0.469)	11.99 (0.472)
Final	12.06 (0.475)	12.75 (0.502)
Change	0.15 (0.006)	0.76 (0.030)
Percent error		
Initial	−3.4	−3.0
Final	−3.2	−3.2
Change	+17	−6.7
Crack length change [mm (in.)]		
After Clarke et al.[a]	0.22 (0.0086)	0.78 (0.031)
After Tada et al.[b]	0.19 (0.0074)	0.68 (0.027)

[a] G. A. Clarke et al., "Single Specimen Tests for J_{Ic} Determination," *Mechanics of Crack Growth*, ASTM STP 590, American Society for Testing and Materials, 1976, pp. 27–42.

[b] H. Tada et al., *The Stress Analysis Handbook*, Del Research Corp., Hellerton, Pa., 1973.

geometrically similar to a standard Charpy specimen with a thickness of 25.4 mm (1 in.). Thus, R curve and maximum load toughness can be compared in these different size specimens and also can be compared with those previously determined using compact specimens as part of the SSU program. The four-point-bend test fixture used is shown in Fig. 4.3. Loads were applied to the bend specimen through 12.7-mm-diam (0.5-in.) loading pins, with the major span equal to 111.8 mm (4.4 in.) and the

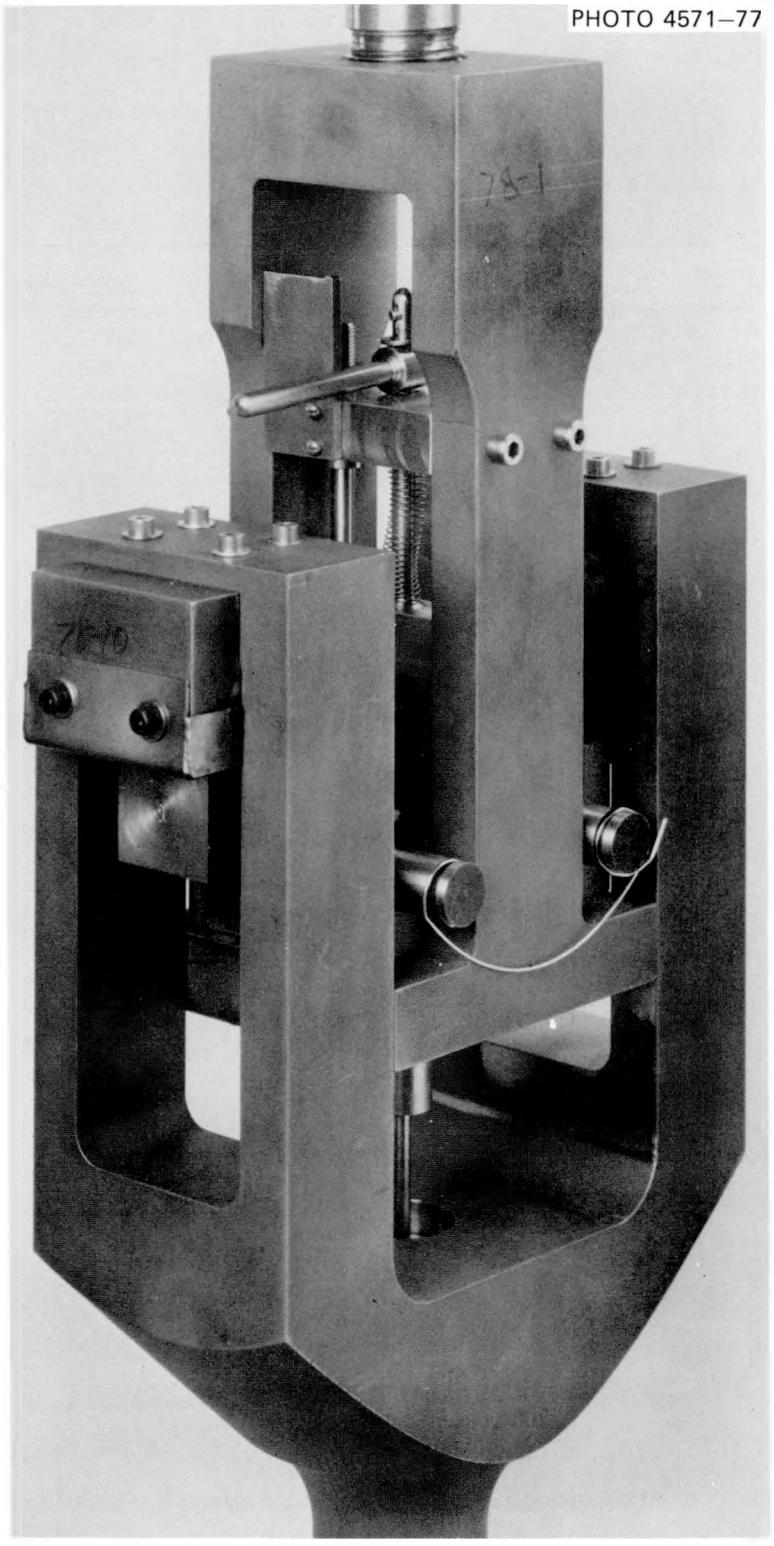

Fig. 4.3. Four-point-bend test fixture for testing 25.4-mm-thick (1-in.) precracked Charpy V geometry specimens.

minor span equal to 50.8 mm (2.0 in.). Load-point displacements were monitored by a single LVDT mounted inside the lower loading fixture.

Fracture tests were performed on deeply cracked 25.4-mm-thick (1-in.) bend bars oriented in the WR direction and fatigue precracked to $a/W > 0.55$ at a maximum stress-intensity factor of 17.6 MPa $\sqrt{m}$ (16 ksi $\sqrt{in.}$). These specimens were tested on an electrohydraulic closed-loop machine in stroke control at 121°C (250°F). Load-deflection records required for the J-integral analysis were produced by continuously plotting load-point displacement as a function of applied load.

In accordance with the recommended procedure for establishing J_{Ic} outlined by Landes and Begley,[5] the multiple-specimen J-R curve technique was used to characterize the ductile fracture toughness behavior of A533 grade B steel at 121°C (250°F). More specifically, a number of deeply cracked compact specimens were loaded to various displacements producing different amounts of crack extension Δa and then unloaded. After unloading, each specimen was heat tinted in order to discolor the crack growth region and subsequently broken open so that the fracture surface morphology could be examined.

The value of J for each specimen was determined from the load vs load-line displacement curve by the following equation:[6,7]

$$J = \frac{2A}{Bb} ,$$

where A is area under the experimental load vs load-line displacement curve minus the component due to Brinelling of the loading pins and compliance of the test fixtures, B is specimen thickness, and b is unbroken ligament length. The R curve was then constructed by plotting values of J as a function of crack extension Δa.

Preliminary data obtained using the four-point-bend technique are shown in Fig. 4.4. These two data points (specimens 02CC11 and 02CC13) were found to be in relatively good agreement with data generated with compact specimens ranging in size from 0.394T to 4T (Ref. 4). It should be noted, however, that the four-point-bend specimens yield slightly higher J values than the compact specimens. This phenomenon is attributed to the effect of axial forces acting in combination with the bending moment

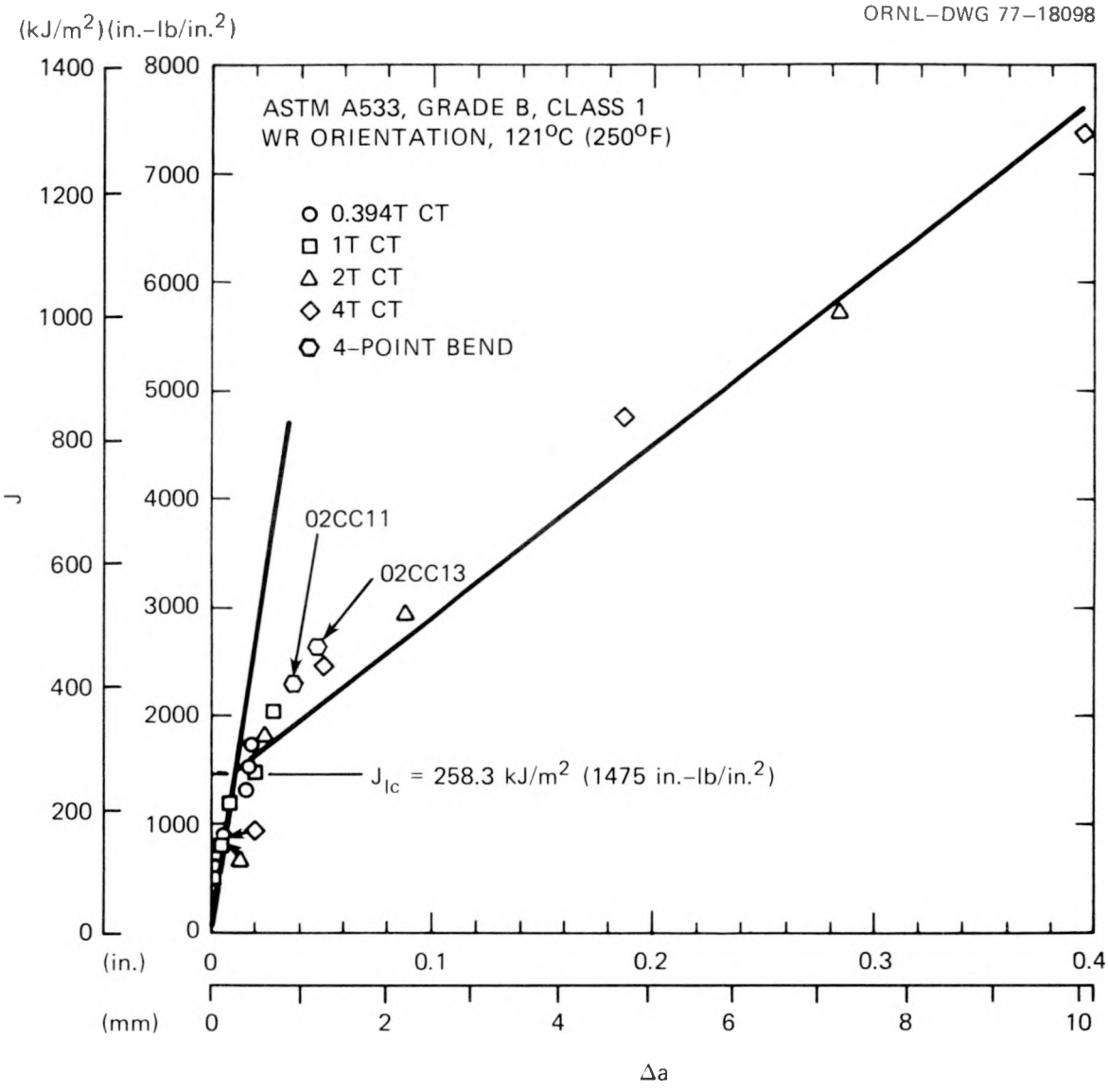

Fig. 4.4. Test results of precracked Charpy V geometry specimens, 25.4 mm (1 in.) thick, tested in four-point bending compared to results of tests with compact specimens of ASTM A533-B1 steel.

in the compact specimens. Consequently, better agreement would be expected if the Merkle-Corten adjustment,[8] which takes into account the tension plus bending components, were applied to the compact specimen data.

Additional four-point-bend data are currently being generated in order to complete the R curve for ASTM A533 grade B steel at 121°C (250°F). In addition, development of a three-point-bend, single-speciment J_{Ic} technique is continuing.

References

1. R. G. Berggren, T. N. Jones, and D. A. Canonico, "Toughness Investigation of Irradiated Materials," *Heavy-Section Steel Technology Program Quart. Progr. Rep. January–March 1977*, ORNL/NUREG/TM-120, pp. 31–32.

2. G. A. Clarke et al., "Single Specimen Tests for J_{Ic} Determination," *Mechanics of Crack Growth*, ASTM STP 590, pp. 27–42, American Society for Testing and Materials, 1976.

3. W. J. Mills, L. A. James, and J. A. Williams, "A Technique for Measuring Load Line Displacements of Compact J_{Ic} Specimens at Elevated Temperatures," HEDL-SA-1176 (to be published).

4. J. A. Williams, "Assessment of the Ductile Fracture Toughness of A533 Pressure Vessel Steel Using Small Specimens," *Heavy-Section Steel Technology Program Quart. Progr. Rep. October–December 1976*, ORNL/NUREG/TM-94, April 1977.

5. J. D. Landes and J. A. Begley, "Test Results from J-Integral Studies: An Attempt to Establish a J_{Ic} Testing Procedure," *Fracture Analysis*, ASTM STP 560, pp. 170–86, American Society for Testing and Materials, 1974.

6. J. R. Rice, P. C. Paris, and J. G. Merkle, *Progress In Flaw Growth and Fracture Toughness Testing*, ASTM STP 536, pp. 231–45, American Society for Testing and Materials, 1973.

7. J. E. Srawley, *Int. J. Fract.* 12, 470–74 (1976).

8. J. G. Merkle and H. T. Corten, "A J Integral Analysis for the Compact Specimen Considering Axial Force as Well as Bending Effects," *Trans. ASME, Ser. J., J. Pressure Vessel Technol.* 96, 286–92 (1974).

5. PRESSURE VESSEL INVESTIGATIONS

Pressure vessel investigations involve the testing of intermediate pressure vessels, primarily to validate methods of fracture analysis and demonstrate the behavior of flawed structures in which the materials, geometry, and state of stress are similar to those found in actual reactor pressure vessels.

Preparations for testing intermediate pressure vessel V-7B are nearly complete. This will be the third test performed with this vessel, the objective of the latest test being to demonstrate the structural integrity of a vessel containing a flaw located in the heat-affected zone (HAZ) of an in-service repair weld. Investigations are continuing on the planning for the V-8 test. Vessel V-8 contains an in-service repair weld in the region of the cylindrical section axial fabrication weld. Residual stress measurements and materials properties are being obtained to determine if a pressure test can be performed in the transition regime to maximize the residual stress effect of flawed-region behavior.

A third model has been tested to evaluate the feasibility of performing a crack-arrest test on an intermediate vessel. The plan involves insertion of lower-toughness crack-starter material in the center section of a vessel; a fast-running crack initiated in the center section would be arrested by the adjacent tougher material. The material properties required to achieve such a result are still being investigated.

5.1 Preparations for HSST Vessel Test V-7B

P. P. Holz

The machined slot in vessel V-7B was sharpened by electron-beam (EB) welding. The specially prepared ceramic 0.1-T (1000-G) permamagnets were used successfully to trim the magnetic flux in the center region of the slot during the EB welding.[1] Maximum preweld flux densities were held to 2.6×10^{-4} T (2.6 G). The EB welding had to be done in separate steps: first, along the bottom of the trapezoidal slot and vertically upward along each slope thereafter. Tungsten target blocks were used to segment the weld. Upslope welding is required to maintain the molten metal puddle

behind the weld gun and attain uniform, rapid chilling so that the core of the weld bead will be highly prestressed. The highly stressed state ensured cracking in a sharply spiked bead on subsequent electrochemical hydrogen charging.

Gaussmeter checks performed after the welding indicated a change in magnetic flux patterns within the entire trapezoidal cavity. However, additional ceramic magnet trimming brought flux levels back down to levels less than 2.6×10^{-4} T.

A welding energy of 190 J/mm (4830 J/in.) was used for the flaw welding, with sharp focus at the surface; EB gun potential, current, and speed were 40.5 kV, 178 mA, and 2300 mm/min (90 in./min).

The hydrogen charging operation was monitored by three acoustic-emission transducers spaced along the interior surface of the vessel directly below the ligament. Previous experience with vessel 7 and the prototype specimen (in vessel parent metal) implied that the crack should form in 8 to 10 hr. The flaw in the heat-affected zone of 7B, however, appeared to have cracked after only $\sim$4 hr of charging and after emitting only about one-third of the anticipated sound events. Charging was continued for an additional 4 hr, since initial optical and visual observations did not confirm continuous cracking along the EB path. Discontinuities were noted along the bottom of the trapezoid and on the slope toward the hemispherical end of the vessel. Complete weld cracking continuity was finally confirmed after 8 hr of total charge time, following several base solution and water flushes and installation of improved lighting.

A repeat of the earlier Westinghouse Tampa Division postweld ultrasonic inspection was performed at ORNL nearly three months after the shop repair welding to check for possible delayed hydrogen cracking. No defects were detected.

Test preparations at the intermediate pressure vessel test facility K-702 (at K-25) continued on schedule, with facility restoration work completed and improved acoustic-emission, instrumentation and control, and data-collection system installations essentially complete. The vessel has been completely instrumented and placed into the test cell. The vessel platecoil system installation is under way, and the instrument trailer

system checkout and preliminary patch pressurization system checkout have begun.

5.2 V-7B Residual Stress Measurements

G. C. Smith

Prior to machining of the large trapezoidal cavity that was to become the V-7B flaw, nine strain gages were attached to the inside surface of the V-7 vessel. The gages were centered on what was to become the ligament at the base of the machined flaw. The location and orientation of these gages relative to the weld repair outline on the vessel inside surface are shown in Fig. 5.1. The changes in strain resulting from machining the cavity are listed in Table 5.1, along with the changes in hoop stress along the length of the ligament. These values were calculated

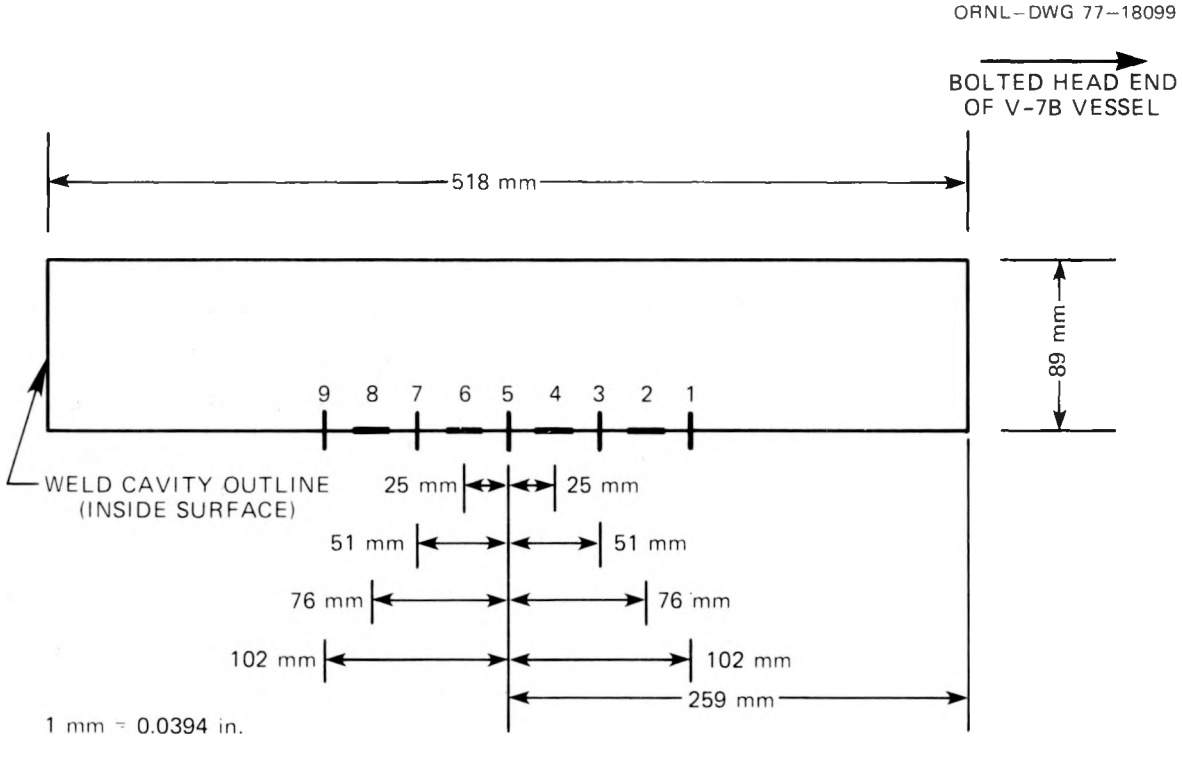

Fig. 5.1. Location of strain gages used to monitor stress redistribution resulting from machining a large trapezoidally shaped flaw in the V-7B vessel.

Table 5.1. Strain and stress changes resulting from machining the V-7B trapezoidal cavity

Location[a]	Δε (microstrain)	Δσ [MPa (ksi)]
1	−731	−183 (−27)
2	−373	
3	−757	−192 (−28)
4	−464	
5	−720	−187 (−27)
6	−478	
7	−788	−200 (−29)
8	−399	
9	−802	−200 (−29)

[a]See Fig. 5.1.

from the expression

$$\Delta\sigma = \frac{E}{1-\nu^2}\left(\Delta\varepsilon_c + \nu\Delta\varepsilon_a\right) , \tag{5.1}$$

where E and ν are Young's modulus and Poisson's ratio, respectively, and $\Delta\varepsilon_c$ and $\Delta\varepsilon_a$ are the changes in circumferential strain and axial strain (average of two adjacent axial strain measurements where appropriate). These data suggest that the introduction of the flaw into the vessel resulted in a significant redistribution of stress and that the residual stress in the ligament at the base of the flaw could have been reduced by as much as 200 MPa (29 ksi).

5.3 Characterization of the Repair Weld in Vessels V-7B and V-8

W. J. Stelzman D. A. Canonico

5.3.1 Hardness investigations

A microhardness traverse across the base metal—repair weld heat-affected zone (HAZ) of the V-7B prototype half-bead repair weld in the V-8 prolongation was completed. Figure 5.2, an 9× enlargement of the

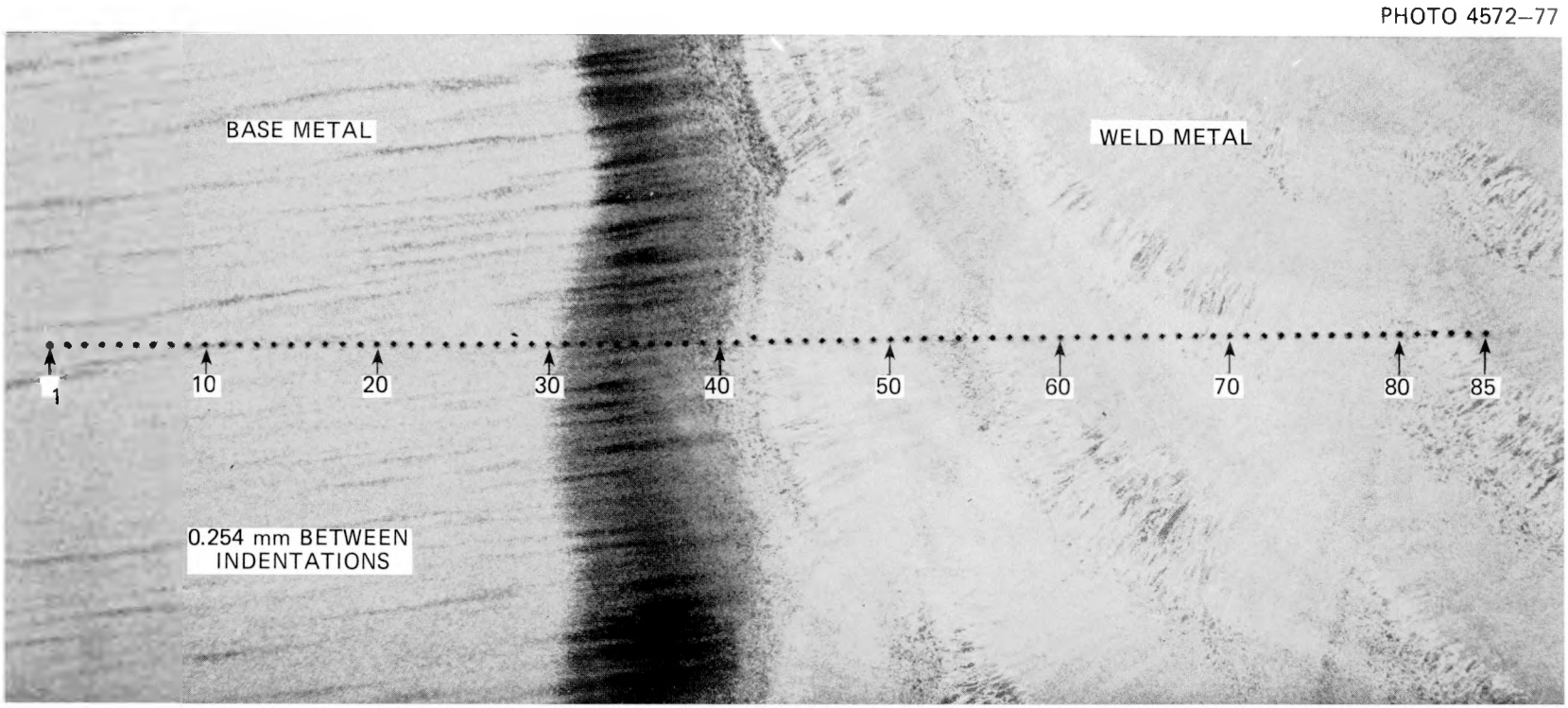

Fig. 5.2. Location of diamond pyramid hardness indentations across the heat-affected zone and adjacent areas of a cross-section of the V-7B prototype half-bead weld repair in intermediate test vessel V-8 prolongation.

region where the penetrations were made, identifies the location of the indentations. The diamond pyramid hardness values (DPH) are plotted in Fig. 5.3. The highest hardness values occur in a 2.29-mm-wide (0.090-in.) region, which is the approximate width of the dark etched band that identifies the HAZ in the base metal. The highest DPH value, 314 (R_C 31.6), occurs twice within 0.254 mm (0.010 in.) of each other. This is in agreement with previous hardness data[2] obtained from three traverses across a similar HAZ in the V-7A prototype weld in the V-9 prolongation.

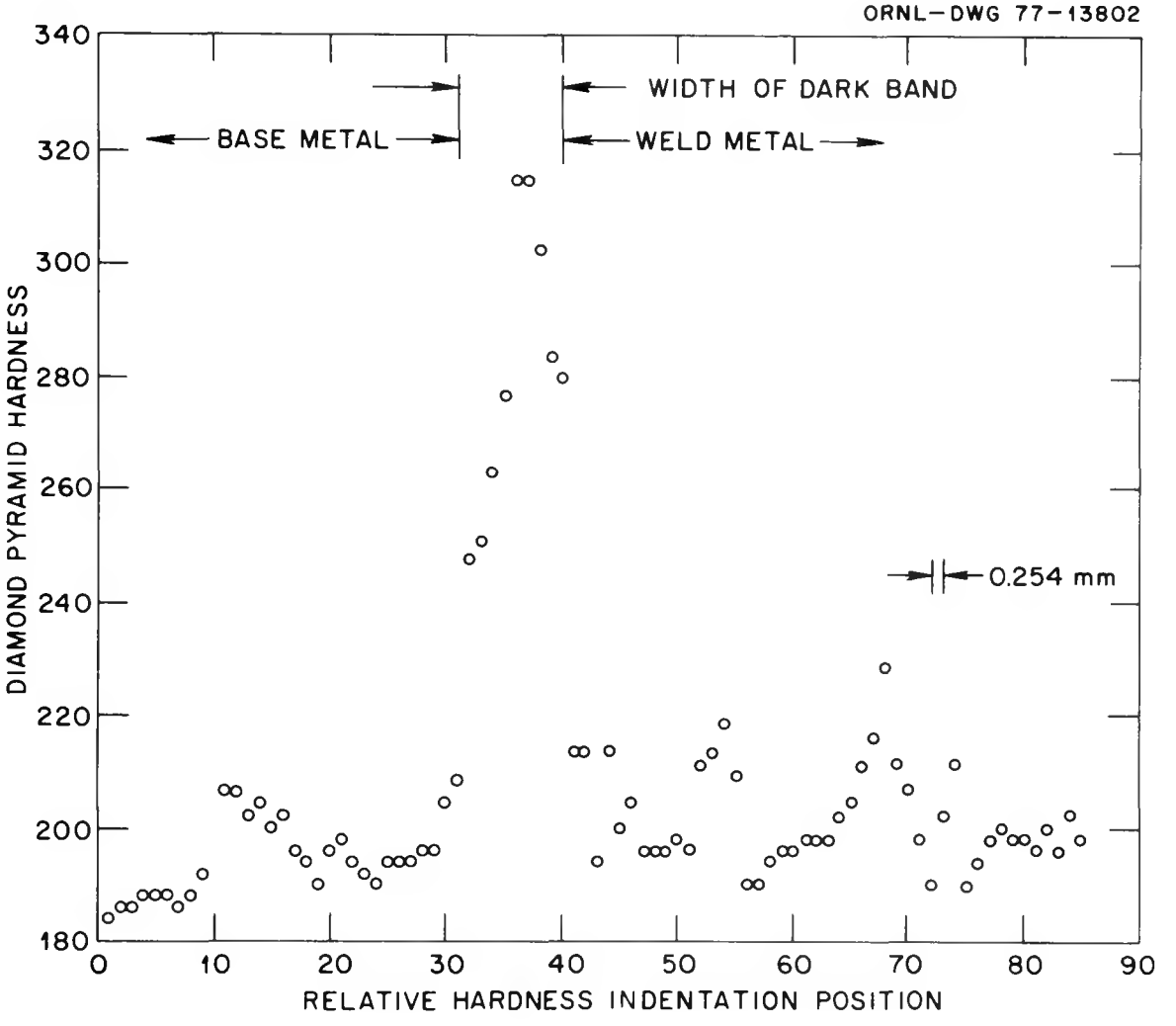

Fig. 5.3. Hardness traverse of the heat-affected zone and adjacent areas of a cross-section of the V-7B prototype shielded-metal-arc half-bead weld repair in the V-8 prolongation.

5.3.2 Fracture toughness investigations

Static fracture toughness (K_{Icd}) results were obtained using precracked Charpy V specimens with the tip of the fatigue crack located in the base metal, in the HAZ, and in the weld metal of the prototype V-7B and V-8 half-bead repair weldments made in the V-8 prolongation. Table 5.2 lists the test results obtained from four regions in the V-7B prototype weldments and seven regions in the V-8 prototype weldments. All the fatigue crack tip location measurements were made from the edge of the dark etched band (HAZ) abutting the weld metal. This is more clearly illustrated in Fig. 5.4 as the HAZ reference edge. Figure 5.5 illustrates approximate specimen orientation and depth locations in both weldments. These will vary slightly in successive partitioning of the weldment, depending upon the straightness of the HAZ for specimen alignment. Two temperature ranges were investigated: 66 to 121°C (150 to 230°F) and −18 to −101°C (0 to −150°F), which bracket the proposed V-7B and V-8 test temperatures, respectively.

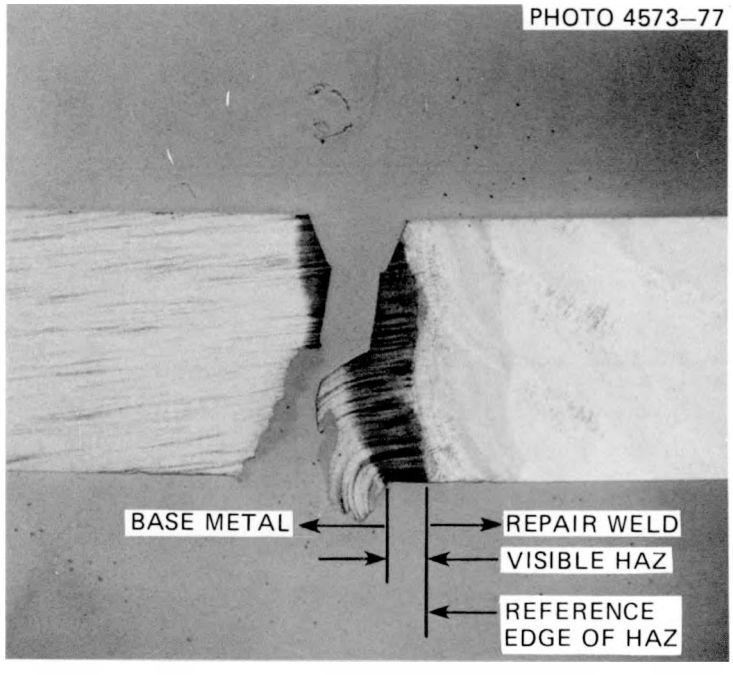

Fig. 5.4. Identification of reference edge cited in Table 5.2.

Table 5.2. Precracked Charpy V static fracture toughness at various distances from the visible HAZ of the prototype V-7B and V-8 half-bead repair welds in the V-8 prolongation

Specimen No.	Depth[a]	Temperature [°C (°F)]	K_{Icd}, static fracture toughness [MPa $\sqrt{m}$ (ksi $\sqrt{in.}$)]	Distance of fatigued crack tip from HAZ reference edge [cm (in.)]
		V-7B type (in HAZ)		
V7W10	0.21	−45.6 (−50)	172 (157)	0
V7W4	0.41	65.6 (150)	241 (219)	0.16 (0.06)
V7W5	0.49	93.3 (200)	307 (279)	0.11 (0.04)
V7W35	0.65	−45.6 (−50)	173 (157)	0
V7W26	0.68	65.6 (150)	360 (328)	0.14 (0.05)
V7W36	0.73	−45.6 (−50)	286 (260)	0.15 (0.06)
V7W27	0.76	121 (250)	299 (272)	0.06 (0.02)
V7W28	0.84	93.3 (200)	382 (348)	0.09 (0.03)
V7W72	0.86	93.3 (200)	362 (329)	0.04 (0.02)
V7W76	0.87	93.3 (200)	254 (231)	0.13 (0.05)
V7W29	0.92	93.3 (200)	280 (255)	0.06 (0.02)
		V-7B type (in base metal)		
V7W39	0.09	−45.6 (−50)	202 (184)	3.89 (1.53)
V7W40	0.19	−45.6 (−50)	247 (225)	3.40 (1.34)
V7W41	0.27	−45.6 (−50)	234 (213)	2.56 (1.01)
V7W42	0.35	−45.6 (−50)	224 (204)	2.10 (0.82)
V7W43	0.43	−45.6 (−50)	203 (185)	1.40 (0.55)
V7W44	0.52	−45.6 (−50)	235 (214)	1.21 (0.47)
V7W37	0.81	−45.6 (−50)	271 (247)	0.28 (0.11)
V7W38	0.90	−45.6 (−50)	280 (255)	0.48 (0.19)
		V-7B type (in repair weld metal)		
V7W31	0.22	−45.6 (−50)	301 (274)	0.41 (0.16)
V7W11	0.29	−45.6 (−50)	115 (105)	0.15 (0.06)
V7W33	0.42	−45.6 (−50)	284 (258)	0.28 (0.11)
V7W13	0.45	−101 (−150)	238 (217)	0.04 (0.01)
V7W34	0.57	−45.6 (−50)	236 (215)	0.19 (0.07)
		V-7B type (weld centerline)		
V7W17	0.86	93.3 (200)	219 (199)	
V7W18	0.92	−73.3 (−100)	173 (157)	
		V-8 type (in base metal)		
V8W44	0.07	−45.6 (−50)	242 (220)	2.76 (1.08)
V8W11	0.08	−45.6 (−50)	247 (225)	0.15 (0.06)
V8W45	0.15	−45.6 (−50)	224 (204)	2.69 (1.06)
V8W12	0.16	−45.6 (−50)	274 (249)	0.47 (0.18)
V8W46	0.24	−45.6 (−50)	273 (248)	3.33 (1.31)
V8W13	0.25	−45.6 (−50)	255 (232)	0.19 (0.07)
V8W47	0.32	−45.6 (−50)	173 (157)	2.76 (1.08)
V8W48	0.40	−45.6 (−50)	252 (229)	2.13 (0.84)
V8W49	0.48	−45.6 (−50)	256 (233)	2.82 (1.11)
V8W50	0.63	−45.6 (−50)	242 (220)	1.21 (0.47)
V8W51	0.71	−45.6 (−50)	251 (228)	2.22 (0.87)
V8W52	0.79	−45.6 (−50)	187 (170)	2.98 (1.17)
V8W53	0.88	−45.6 (−50)	268 (244)	1.80 (0.71)

Table 5.2 (continued)

Specimen No.	Depth[a]	Temperature [°C (°F)]	K_{Icd}, static fracture toughness [MPa $\sqrt{m}$ (ksi $\sqrt{in.}$)]	Distance of fatigued crack tip from HAZ reference edge [cm (in.)]
		V-8 type (in base metal—repair weld HAZ)		
V8W2	0.15	−17.8 (0)	334 (304)	0.08 (0.03)
V8W3	0.23	−45.6 (−50)	280 (255)	0.10 (0.04)
V8W4	0.31	−73.3 (−100)	327 (298)	0.04 (0.02)
V8W5	0.39	−101 (−150)	366 (333)	0.08 (0.03)
		V-8 type (in repair weld metal near base metal)		
V8W1	0.06	10.0 (50)	173 (157)	0.04 (0.02)
V8W14	0.33	−45.6 (−50)	124 (113)	0.04 (0.02)
V8W25	0.35	−45.6 (−50)	225 (205)	0.15 (0.06)
V8W15	0.41	−45.6 (−50)	111 (101)	0.47 (0.19)
V8W26	0.43	−45.6 (−50)	271 (247)	0.42 (0.17)
		V-8 type (center of repair weld metal)		
V8W10	0.51	−17.8 (0)	185 (168)	
		V-8 type (in repair weld near fabrication weld)		
V8W16	0.08	−45.6 (−50)	153 (139)	0.44 (0.17)
V8W17	0.16	−45.6 (−50)	278 (253)	0.19 (0.07)
V8W18	0.25	−45.6 (−50)	205 (187)	0.03 (0.01)
		V-8 type (in repair weld—fabrication weld HAZ)		
V8W6	0.12	−17.8 (0)	266 (242)	0.18 (0.17)
V8W7	0.21	−45.6 (−50)	213 (194)	0.08 (0.03)
V8W8	0.29	−45.6 (−50)	232 (211)	0.10 (0.04)
V8W9	0.37	−73.3 (−100)	209 (190)	0.04 (0.02)
		V-8 type (in fabrication weld metal)		
V8W54	0.06	−45.6 (−50)	123 (112)	2.69 (1.06)
V8W55	0.05	−45.6 (−50)	204 (186)	3.07 (1.21)
V8W56	0.23	−45.6 (−50)	88 (80)	2.76 (1.08)
V8W57	0.31	−45.6 (−50)	82 (75)	2.06 (0.81)
V8W19	0.33	−45.6 (−50)	108 (98)	0.15 (0.06)
V8W58	0.39	−45.6 (−50)	44 (40)	2.12 (0.83)
V8W20	0.41	−45.6 (−50)	221 (201)	0.38 (0.15)
V8W59	0.48	−45.6 (−50)	117 (107)	1.69 (0.67)

[a]Fraction of wall thickness from outer surface to tip of fatigued crack. Wall thickness is 159 mm (6 1/4 in.).

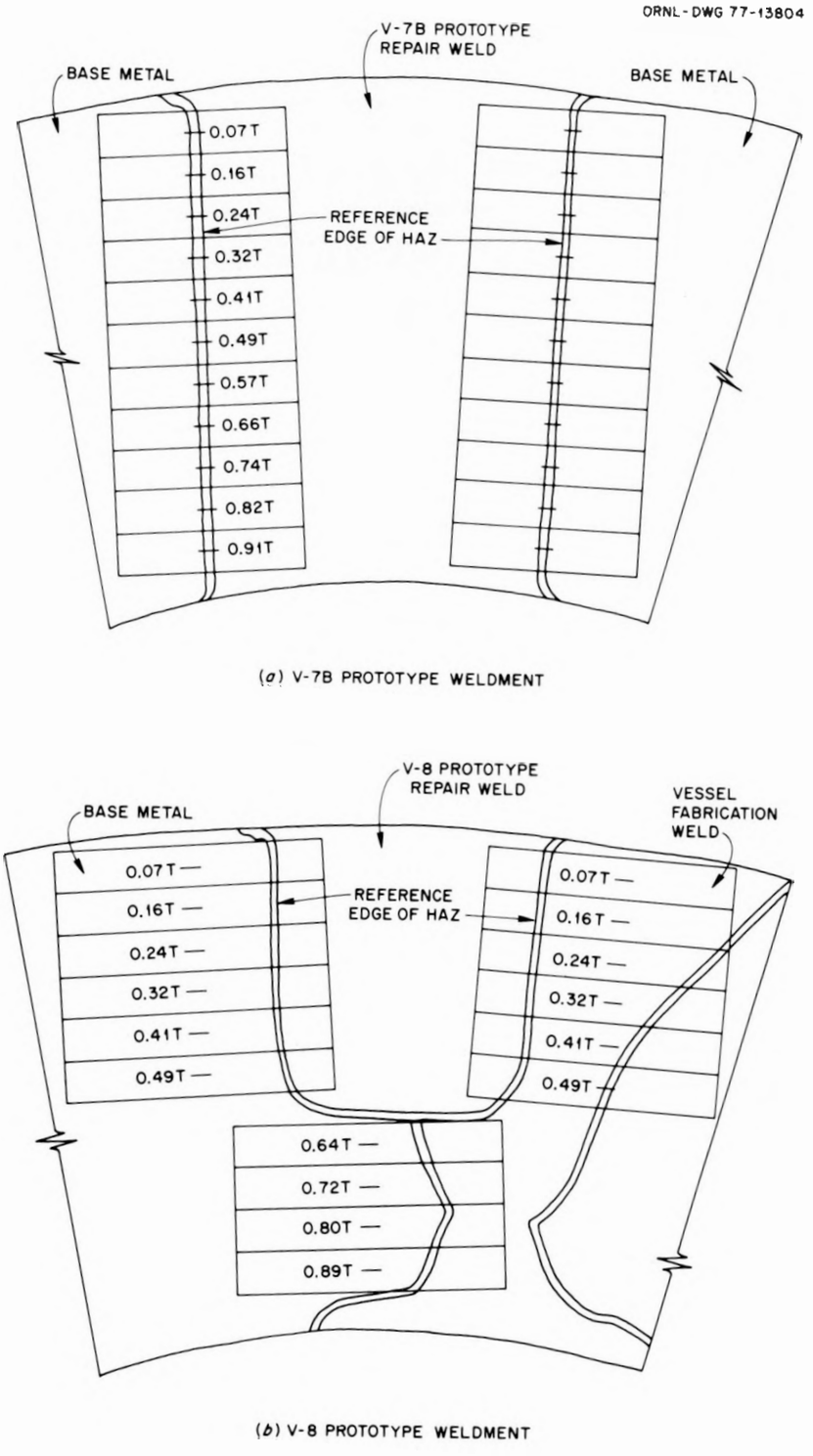

Fig. 5.5. Cross-sections of the prototype half-bead-technique weld repairs in the V-8 prolongation.

Static fracture toughness (K_{Icd}) results from the V-7B weldment specimens tested indicate a range from 115 to 301 MPa $\sqrt{m}$ (105 to 274 ksi $\sqrt{in.}$) at −46°C (−50°F). Both extremes occur in the repair weld metal. In the 66 to 121°C (150 to 250°F) temperature range, the K_{Icd} values ranged between 219 and 382 MPa $\sqrt{m}$ (199 and 348 ksi $\sqrt{in.}$). The highest toughness values occur in the base metal—repair weld HAZ and the lower values in the repair weld metal.

The results obtained in static fracture toughness tests of the V-8 weldment specimens indicate a range from 44 to 366 MPa $\sqrt{m}$ (40 to 333 ksi $\sqrt{in.}$) in the −18 to −101°C (0 to −150°F) temperature region. The lowest K_{Icd} values were obtained from specimens removed from the original prolongation fabrication weld metal, and the highest values were obtained in the base metal—repair weld HAZ. In the repair weld, the lower K_{Icd} values occur adjacent to the HAZ (in the weld metal), and the highest K_{Icd} values occur in the fabrication weld—repair weld HAZ. All the values that fell below 110 MPa $\sqrt{m}$ (100 ksi $\sqrt{in.}$) were obtained in the original prolongation fabrication weld. Additional testing of the fabrication weld is planned.

An extensive metallographic examination of the fractures that occurred in the precracked Charpy V-notch specimens is under way. To date, the examination indicates that the crack propagation in specimens whose fatigue cracks lie in the visible HAZ identified in Fig. 5.4 is through the base metal. Figure 5.6 illustrates the type of fracture behavior noted in this study. The fatigue crack front is seen to lie near the middle of the visible HAZ. There is evidence that the crack tip lies in a region whose hardness is fairly high, approximately 250 to 300 DPH. The crack propagation is along the interface between the visible HAZ (dark band) and the (apparently) unaffected base metal. The hardness in the region where the crack propagated is approximately 210 DPH. (The hardness values are approximated from the traverse shown in Figs. 5.2 and 5.3.) A similar fracture behavior was not noted for specimens whose fatigue crack front is in the weld metal. In those specimens, cracks tended to propagate in a direct path or to follow the contour of a weld pass. Figure 5.7 shows the results of the examination of precracked Charpy V-notch tests where the crack tip is in the weld metal. Figure 5.7a is a photomacrograph of a specimen whose crack tip is in the repair weld adjacent to the half-bead repair weld and

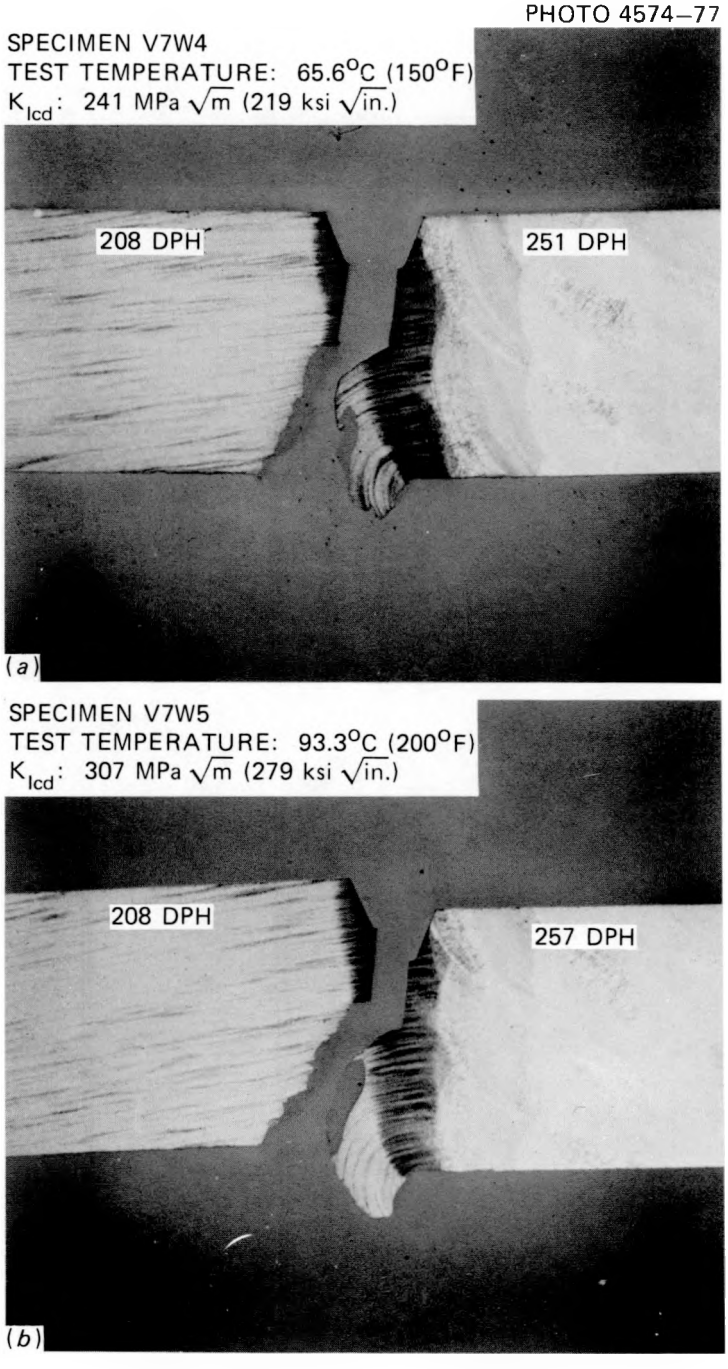

Fig. 5.6. Typical crack propagation mode for precracked Charpy V-notch specimens whose fatigue cracks lie in the heat-affected zone between the base metal and the half-bead weld repair. Failure consistently occurs through the lower-hardness base metal.

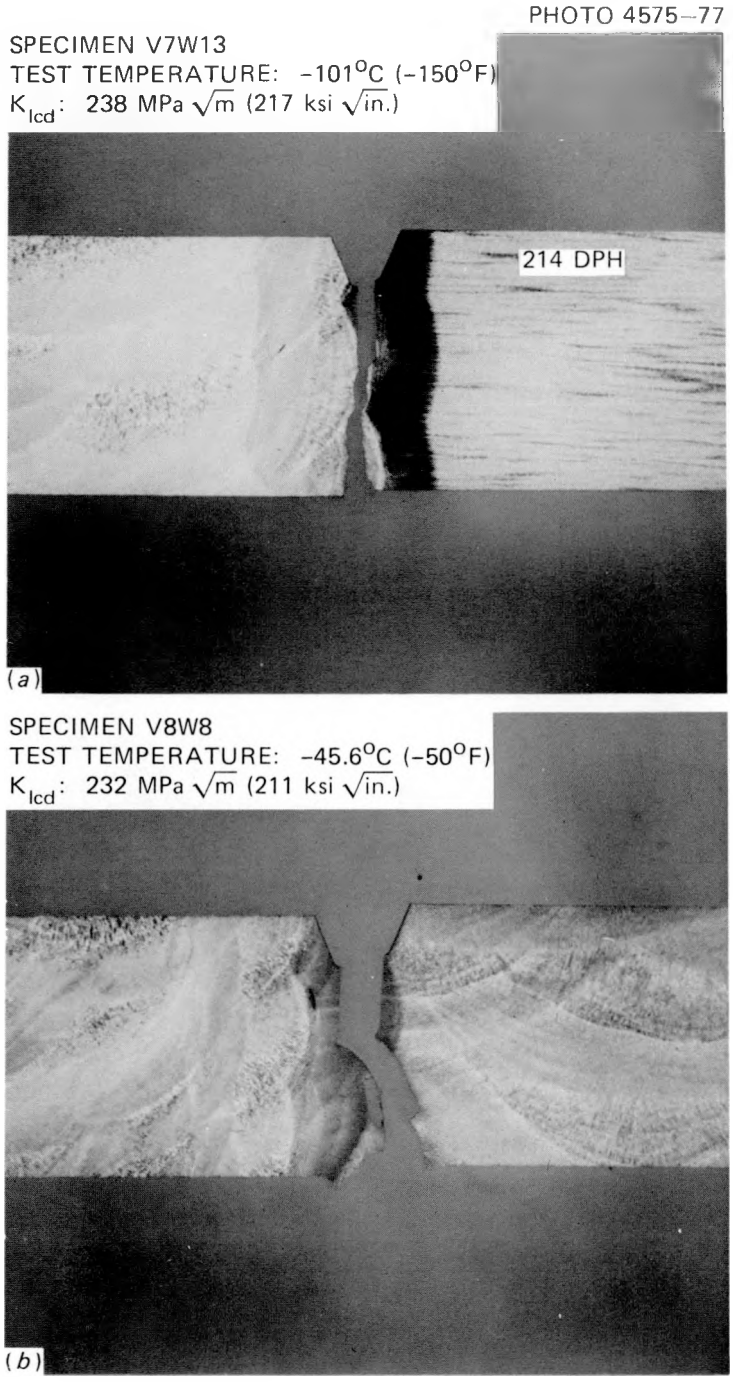

Fig. 5.7. Fracture in precracked Charpy V-notch specimens whose fatigue crack lies in weld metal propagates through the weld. (a) Crack located in weld metal adjacent to the base metal–half-bead repair weld fusion line. (b) Crack located in heat-affected zone between fabrication weld and half-bead repair weld.

base metal fusion line. The propagation path is essentially straight through the specimen. Figure 5.7b is a photomacrograph of a precracked Charpy V-notch specimen where the fatigue crack lies in the HAZ in the fabricated weld. This HAZ occurs as a consequence of the half-bead weld repair. The crack initiated in the HAZ and appears to have run into and propagated through the fabrication weld. There is evidence, as shown in Table 5.2, that the least-tough material in the vessels repaired with half-bead welds is the fabrication weld.

5.4 V-7C Crack-Arrest Model Studies

5.4.1 Material characterization (W. J. Stelzman, D. A. Canonico)

We have continued to characterize the quenched-only 44-mm-thick (1 3/4-in.) sections cut from HSST plate section 03JZ[3] and have begun to characterize the quenched-only 38-mm-thick (1 1/2-in.) sections cut from HSST plate section 04BE.[4] Precracked Charpy V fracture toughness (K_{Icd} and K_{Idd}) and Charpy V impact results were obtained from 04BE, and dynamic fracture toughness (K_{Idd}) results were obtained from 03JZ. The static fracture toughness results from 03JZ were previously reported.[3]

Charpy V impact test results from WT-oriented specimens of 04BE are shown in Fig. 5.8 together with previous results from 03JZ. The impact

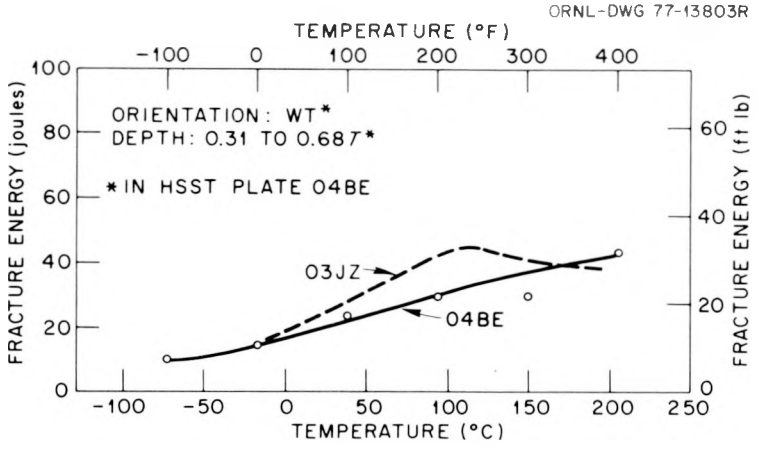

Fig. 5.8. Variation of Charpy V impact energy with temperature for 38.1-mm-thick (1 1/2-in.) through-the-thickness slices from plate section 04BE after reaustenitizing for 1 1/2 hr at 871°C (1600°F) and water quenching.

properties of 04BE appear to be poorer than those of 03JZ when both are in the quenched-only condition. Based upon the fracture appearance of the 04BE specimens, the transition region is between −46 and 149°C (−50 and 300°F), and the onset of the upper-shelf energy is about 37 J (27 ft-lb). The use of the upper case "T" and the lower case "t" to identify the through-the-thickness depth location is consistent with previous reporting.[3] All the specimens tested came from the 1/3t and 2/3t depth locations in the quenched-only plates.

Static and dynamic fracture toughness results from WT-oriented specimens of 04BE are shown in Fig. 5.9. The dynamic fracture toughness

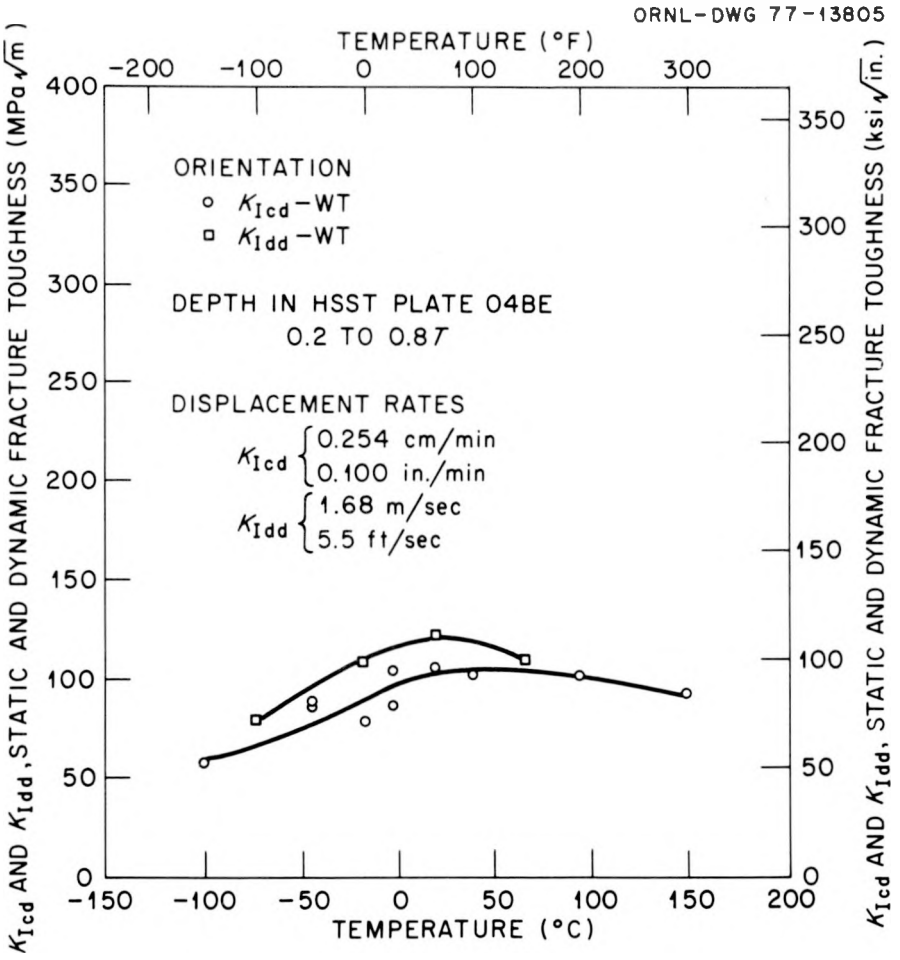

Fig. 5.9. Variation of precracked Charpy static and dynamic fracture toughness with temperature for 38.1-mm-thick (1 1/2-in.) through-the-thickness slices from plate section 04BE after reaustenitizing for 1 1/2 hr at 871°C (1600°F) and water quenching.

is superior to the static fracture toughness in the transition region [−18°C (0°F)]. The K_{Idd} and K_{Icd} toughness values are 110 and 90 MPa $\sqrt{m}$ (100 and 82 ksi $\sqrt{in.}$), respectively, at −18°C (0°F). Dynamic fracture toughness results from RT-oriented specimens of 03JZ are shown in Fig. 5.10 together with previously reported static fracture toughness values. The differences in K_{Icd} and K_{Idd} properties of 03JZ are not significant in the transition region. Comparison of the K_{Icd} results indicates that the static fracture toughness of 04BE is somewhat poorer than that of 03JZ.

Additional dynamic fracture toughness and compact tension data are being obtained.

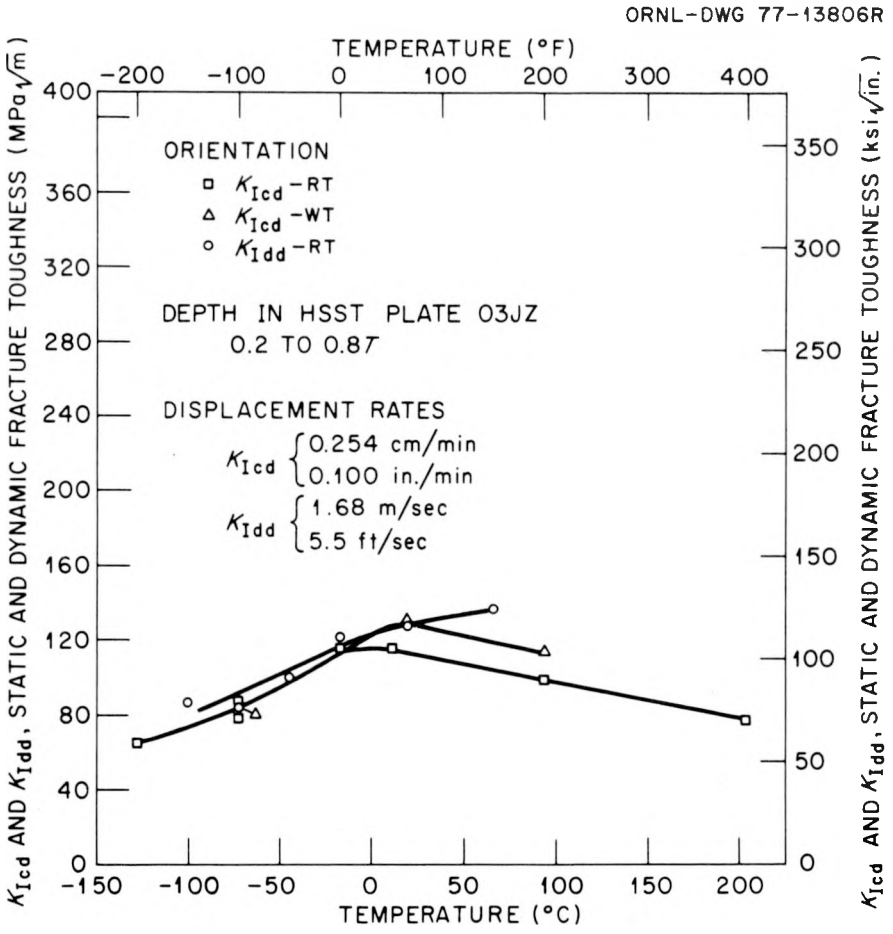

Fig. 5.10. Variation of precracked Charpy static and dynamic fracture toughness with temperature for 44.1-mm-thick (1 3/4-in.) through-the-thickness slices from plate section 03JZ after reaustenitizing for 1 1/2 hr at 871°C (1600°F) and water quenching.

5.4.2 Third crack-arrest model test (G. C. Smith)

During this reporting period, the third in a series of crack-arrest models was tested. The model was pressurized on two occasions. The first pressurization, at a test temperature of −22°C (−7°F), resulted in a small stable extension of the flaw. The second pressurization, at a test temperature of −47°C (−52°F), resulted in fast fracture and destruction of the model.

All three of the crack-arrest models tested thus far had the configuration shown in Fig. 5.11. The first model test, conducted at 91°C (196°F), resulted in slow, stable crack extension through the brittle starter section and subsequent arrest at the brittle-to-tough material interface. The second model, tested at 4°C (39°F), exhibited substantially the same response as the first model with the exception of two short bursts of fast crack extension followed by arrest. Crack extensions in the first and second models were initially detected at 93 MPa (13,400 psi) and 76 MPa (11,000 psi), respectively. As the pressure in the models was increased, the cracks slowly extended to and through the electron-beam welds joining the brittle sections to the tough sections.

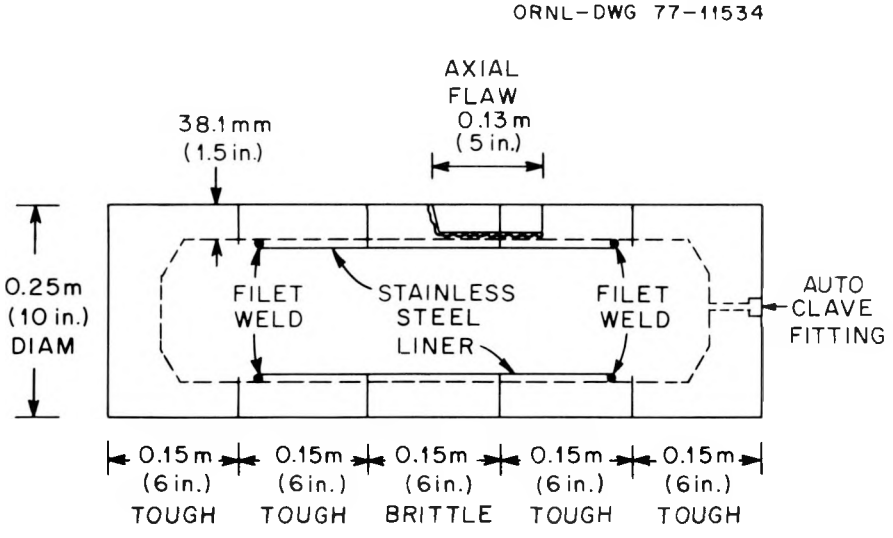

Fig. 5.11. Cross section of the crack-arrest model configuration. The center section was A533 that had been reaustenitized and water quenched. The other four sections were A533, grade B, class 1.

The maximum pressure achieved in each test was 103 MPa (15,000 psi). This pressure was held for a minimum of 5 min without any further indication of crack extension. Further discussion of the first two model tests can be found in Ref. 5.

The only significant difference between the first two models and the third one was that the brittle center section of the third model had inferior Charpy impact energy and inferior slow-bend precracked Charpy specimen toughness relative to the first two models. The difference apparently stemmed from the fact that the center sections of the first two models were machined from HSST plate 03, while the center section of the third model was machined from HSST plate 04. Both plates were A533, grade B, class 1 and are described in Ref. 6. After the center cylinders were machined, they were reaustenitized at 872°C (1602°F) for 1.5 hr and water quenched. The Charpy impact energies of the two materials are shown in Fig. 5.8, and the slow-bend precracked Charpy specimen toughness data are shown in Fig. 5.12.

The temperature shift evident in Figs. 5.8 and 5.12 was the motivation for using HSST plate 04 quenched-only material for the third model test. Since sustained unstable crack growth had not been achieved in the first two model tests, it seemed that the third model would require blunting of the crack (thereby increasing the stored energy and making the flawed vessel less stable), further reduction of the test temperature (thereby increasing the brittleness of the material), or use of a more brittle material for the center section. It was decided that for the third model test both a more brittle quenched-only plate 04 center section and a lower test temperature would be employed to improve the chances of fast fracture. A test temperature of −22°C (−7°F) was chosen because it was estimated to offer the best chance of fast fracture followed by arrest as the crack extended into the tough material.

The third model was initially tested on May 26, 1977, at −22°C (−7°F). Crack extension of more than 3.5 mm (0.14 in.) but less than 9.8 mm (0.39 in.) was indicated at 91 MPa (13,200 psi) by the ladder gages described in Ref. 5. Pressurization was continued up to 103 MPa (15,000 psi), as had been done in the first two model tests. However, unlike the first two model tests, further crack extension did not occur. A posttest visual

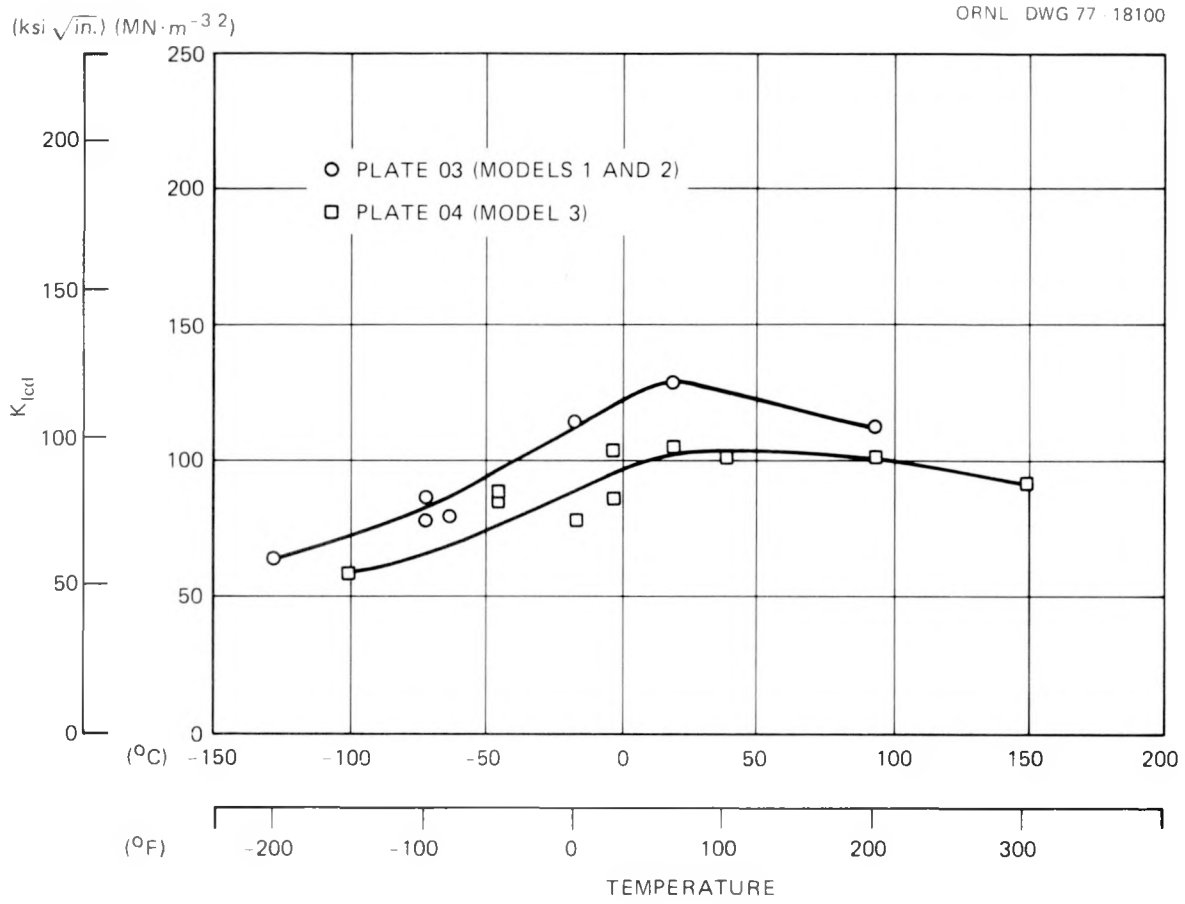

Fig. 5.12. Slow-bend precracked Charpy specimen toughnesses for HSST plate 03 (model tests 1 and 2) and HSST plate 04 (model test 3).

inspection of the crack confirmed the ladder gage indications. Because unstable crack extension did not then appear likely at the −22°C (−7°F) test temperature and the third model was intact and had experienced only slight crack extension, it was decided that a subsequent continuation of the test at a lower temperature should be conducted in order to achieve fast fracture. Crack arrest was considered very unlikely at the test temperature in that the initiation toughness was quite close to the arrest toughnesses for A533, grade B, class 1, which have been published by Battelle Columbus Laboratories (BCL)[7] and Materials Research Laboratory (MRL).[8]

The third crack-arrest model was retested on June 2, 1977, at −47°C (−52°F). Unstable crack extension occurred at 102 MPa (14,800 psi). Figure 5.13 is a photograph of the failed vessel. Although it is not readily

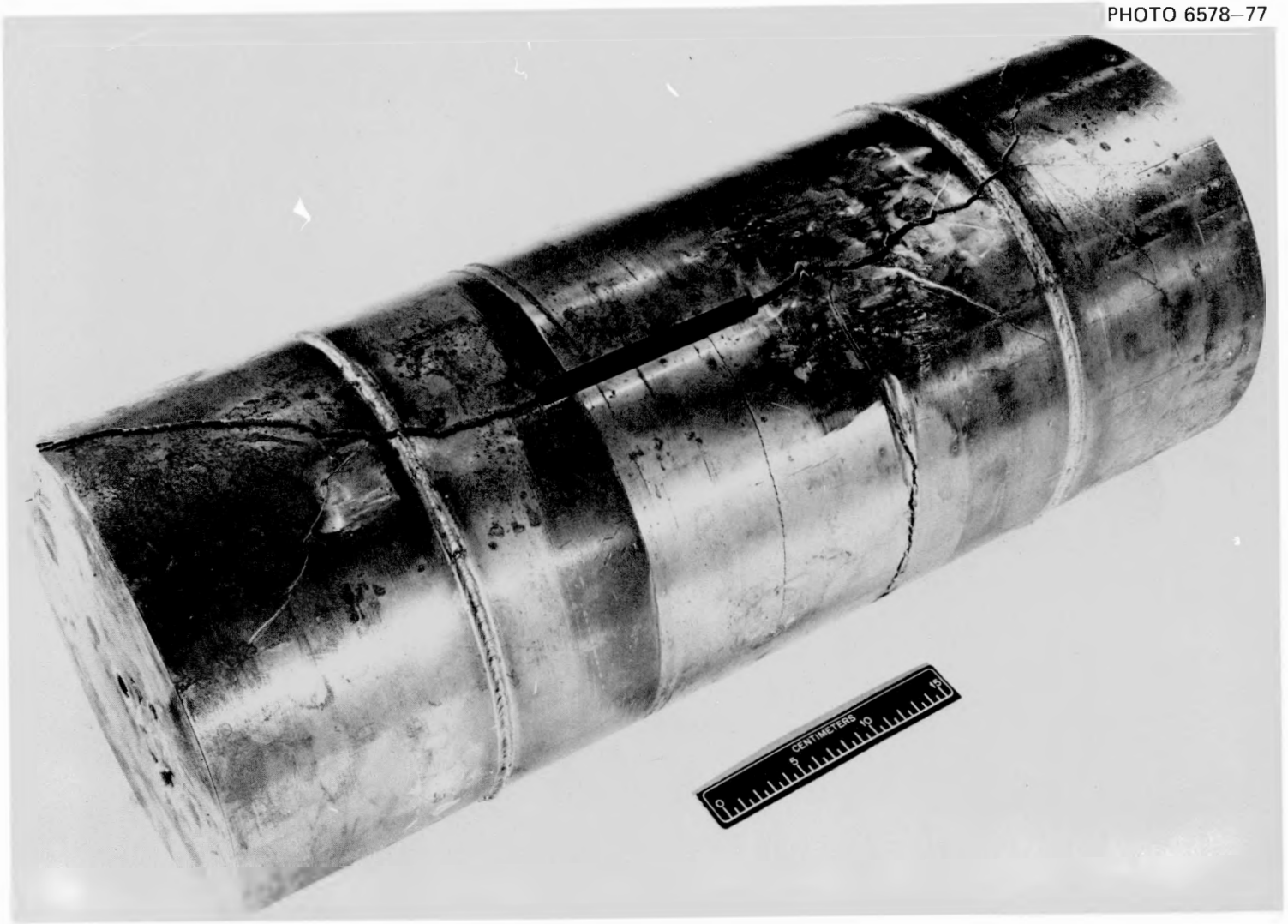

Fig. 5.13. Third crack-arrest model tested to failure at −47°C (−52°F) (1 cm = 0.394 in.).

apparent from the photograph, there are four electron-beam circumferential welds in the model. The two welds joining the brittle center section to the tough sections were ground flush in order that the weld bead would not interfere with crack extension. The two electron-beam weld beads that are apparent in the photograph are between the tough sections and the flat-head caps.

From Fig. 5.13, it can be seen that axial cracks propagated from each end of the machined slot. The axial crack that propagated to the right of the slot was the crack in brittle material which had been sharpened and which had experienced very slight extension during the initial test of the model at the higher temperature. Figure 5.14 shows plots of crack extension as indicated by the ladder gages and the response of two circumferential strain gages located along an axial line bisecting the machined slot (shown schematically) as a function of time measured from the first indication of unstable crack extension. It can be seen from

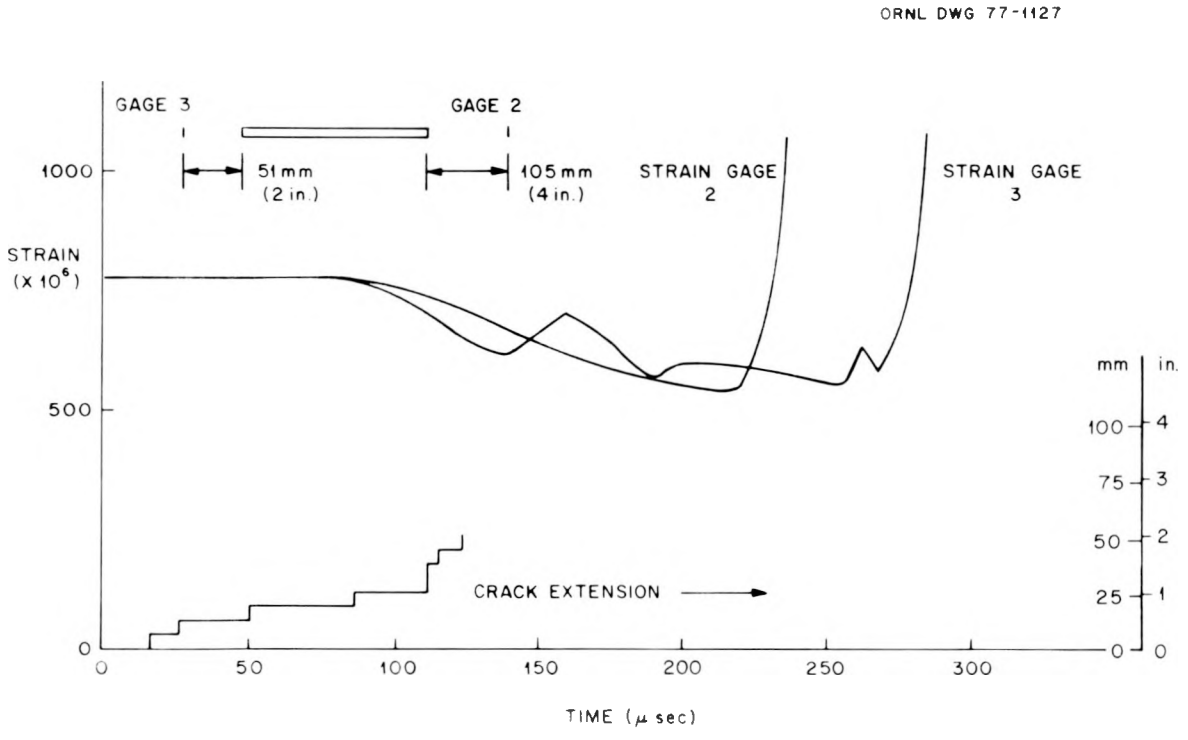

Fig. 5.14. Circumferential strains and crack extension as a function of time for the third crack-arrest model test. Test temperature of —47°C (—52°F).

the plot of crack length vs time that the crack had an average velocity of 410 m/sec (16,140 in./sec). The reduction in strain during crack extension would seem to be due to a drop in pressure. The pressure transducers used in the third model test had integral signal amplifiers with slow response times (i.e., on the order of a millisecond or slightly less). Therefore, the pressure indicated by those transducers during the drop to zero can only be considered as an upper bound. The steep rise in strain after the initial reduction is probably due to the influence of the crack tips as they approached each gage. It was observed that the cracks did propagate through the gages. If it is assumed that the crack running to the left had somewhat the same velocity as that running right, it follows that the right-running crack started much earlier and, in fact, induced the subsequent cracks that are seen in Fig. 5.13.

There are two circumferentially oriented cracks in Fig. 5.13 that propagated approximately 180° about the model, one of which was close to the electron-beam weld. When the model was sectioned, a void [91 mm (3.6 in.) by 19 mm (0.75 in.)] was found in the electron-beam weld. The void was 71 mm (2.8 in.) from the line of initial crack extension. It would therefore seem that, because of its distance from the point of crack initiation, the void did not affect the initial crack extension but could have been a contributing factor to crack extension through the weld. The other circumferential crack initiated at a point along the machined slot. There was no apparent flaw or stress concentrator that would contribute to the initiation of that flaw. However, multiple cracks are not an unknown phenomenon and are usually attributed to stress waves.[9]

The stress-intensity factor K at initiation of crack extension can be found by applying the bulging factor correction to the flat-plate stress-intensity factor, giving

$$K = \left(1 + 1.61 \frac{a^2}{R_{av}\, t}\right)^{1/2} \frac{PR}{t} \sqrt{\pi a} \,, \tag{5.2}$$

where

P = pressure at failure,

R_{av} = average radius,

R = inside radius,

a = crack half-length,

t = wall thickness.

Using Eq. (5.2), the stress-intensity factor is found to be 171 $MN \cdot m^{-3/2}$ (155 $ksi \cdot in.^{1/2}$) at the initiation of unstable crack extension. This exceeds the small specimen fracture toughness at the test temperature of −47°C (−52°F), which is shown in Fig. 5.12. This difference is likely due to the blunting and warm prestressing that occurred during the pressurization of the model on May 26, 1977, at −22°C (−7°F). The stress-intensity factor at initiation also exceeds the arrest toughness (MRL)[8] and the minimum dynamic toughness (BCL)[7] for A533 at the test temperature. Since the stress-intensity factor increases with crack length at constant pressure, crack arrest at the brittle-tough interface was not to be expected.

5.4.3 Metallographic examinations of crack-arrest models (R. Crouse, D. A. Canonico)

The scanning electron microscope (SEM) was employed to perform an extensive examination of the fracture surfaces from the crack-arrest model (CAM) tests conducted to date. Photographs of the fracture surfaces and the cutting plan are shown for CAM-1, -2, and -3 in Figs. 5.15, 5.16, and 5.17, respectively. The sectioning was planned in order to permit examination of the crack-initiation, crack-propagation, and, where possible, crack-arrest regions of the fracture surfaces. Models CAM-1 and -2 were tested at 91°C (196°F) and 4°C (39°F), respectively. The crack-initiation and crack-propagation regions of these two model tests exhibited a dimple fracture mode. Figure 5.18 shows SEM photomicrographs representative of the crack-propagation region in CAM-1; the dimple mode of fracture is evident in Fig. 5.18b. A similar fracture mode was observed in the propagation region of CAM-2. Figure 5.19 shows SEM photomicrographs of this region; the dimple fracture is evident in Fig. 5.19b. When the propagating crack of CAM-2 reached the EB fabrication weld, the fracture mode changed to cleavage. Figure 5.20 contains a SEM photomicrograph of a typical area in the EB fabrication weld where the cleavage model of fracture is evident. Additional SEM studies are being conducted.

Crack-arrest model test 3 was conducted at −47°C (−52°F). Figure 5.21 shows SEM photomicrographs of the propagation region of CAM-3. The fracture exhibits a cleavage mode.

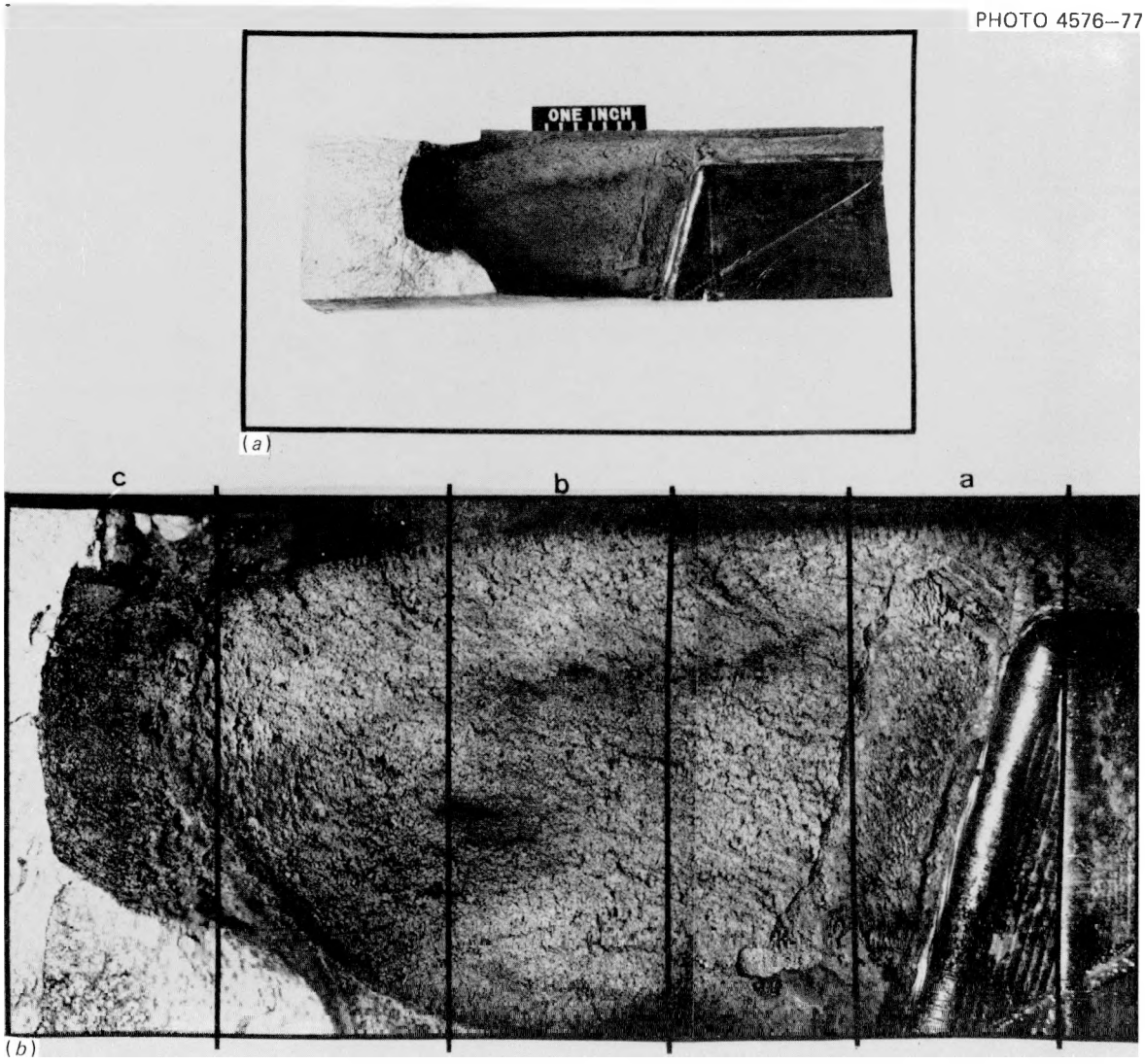

Fig. 5.15. Sectioning procedure for preparing SEM samples from crack-arrest model 1 (CAM-1). This test was conducted at 90°C (196°F). The fracture surface sample is shown in (A). The sample was sectioned in three pieces as shown in (B) and the specimens identified as CAM-1a, -b, and -c, which represent the crack-initiation, crack-propagation, and crack-terminus regions, respectively.

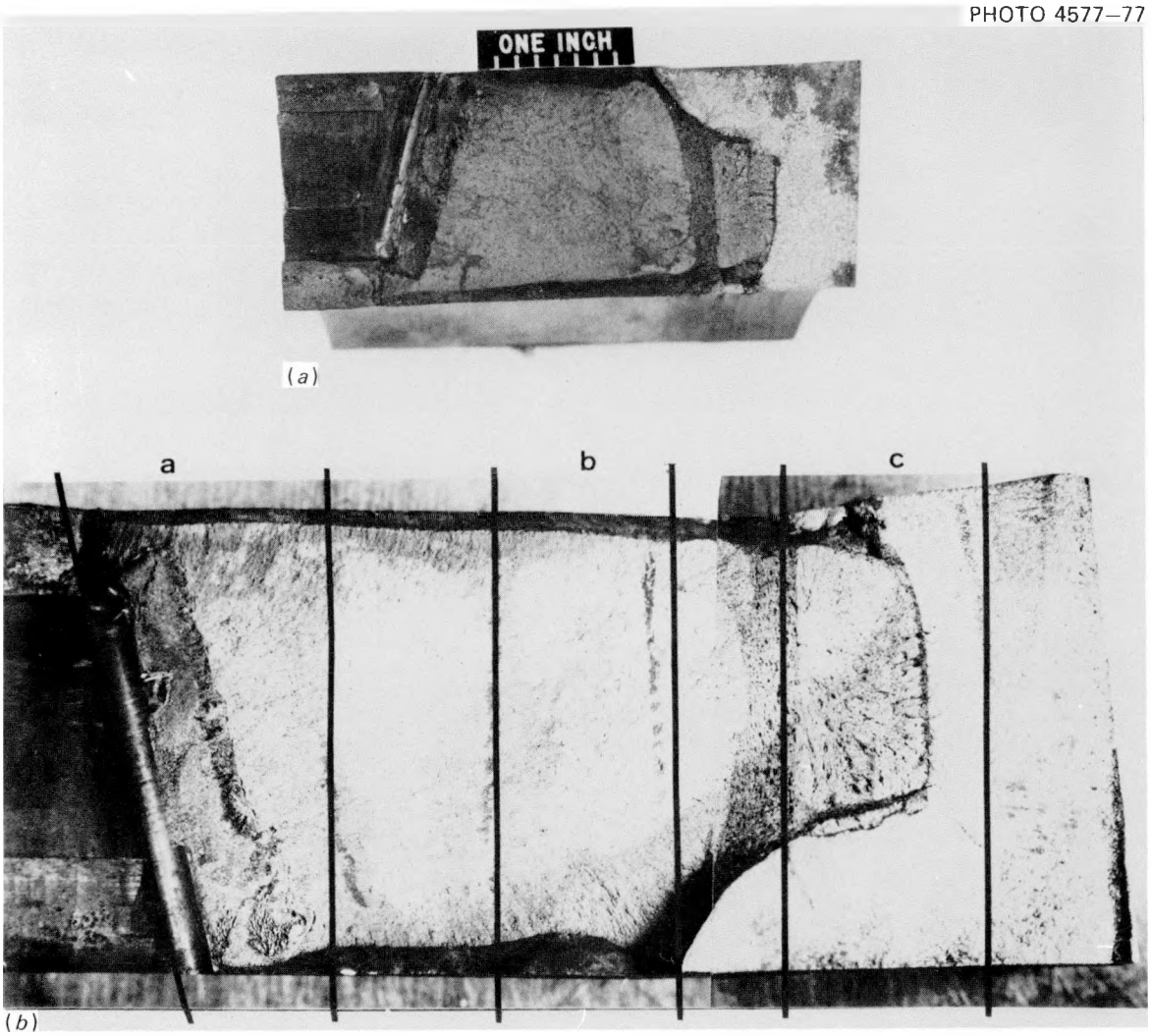

Fig. 5.16. Sectioning procedure for fracture surface from crack-arrest model test 2 (CAM-2). This test was conducted at 4°C (39°F). The fracture surface is shown in (A); the sectioning plan and specimen identification are shown in (B). The specimens CAM-2a, -b, and -c represent the crack-initiation, crack-propagation, and crack-arrest regions of the fracture.

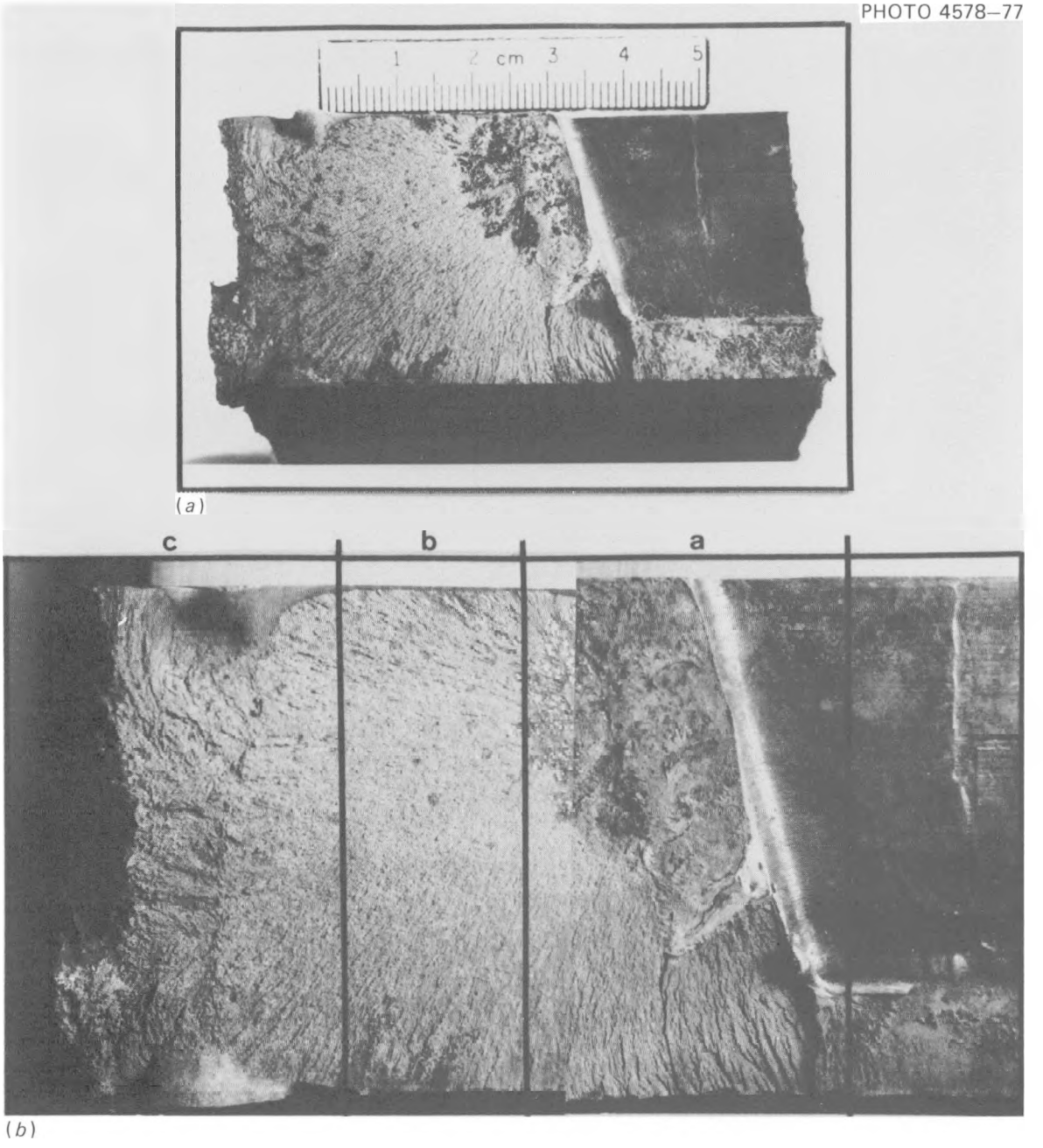

Fig. 5.17. Sectioning procedure for fracture surface from crack-arrest model test 3 (CAM-3). The test was started when the vessel was at −22°C (−8°F). After what appeared to be an initial ductile tear, the test was halted; the vessel cooled to −50°C (−52°F), and the test was completed. The fracture surface is shown in (A). The sample was sectioned as shown in (B) and the specimens identified as CAM-3a, -b, and -c, which represent the crack-initiation, crack-propagation, and crack-arrest regions, respectively.

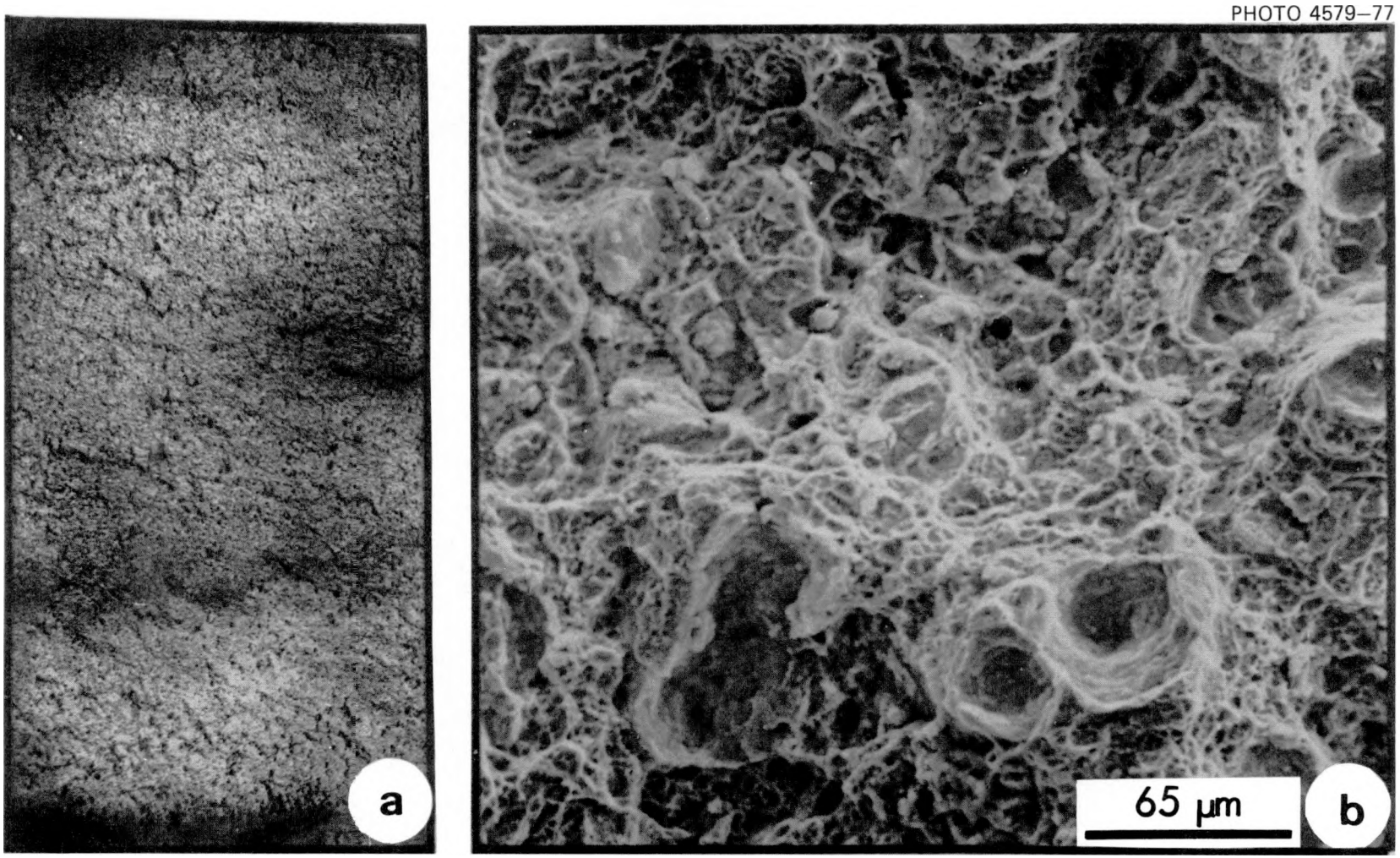

Fig. 5.18. Scanning electron micrographs of the crack-propagation region (CAM-1b) of crack-arrest model test 1. This region exhibits a dimple fracture mode.

PHOTO 4580–77

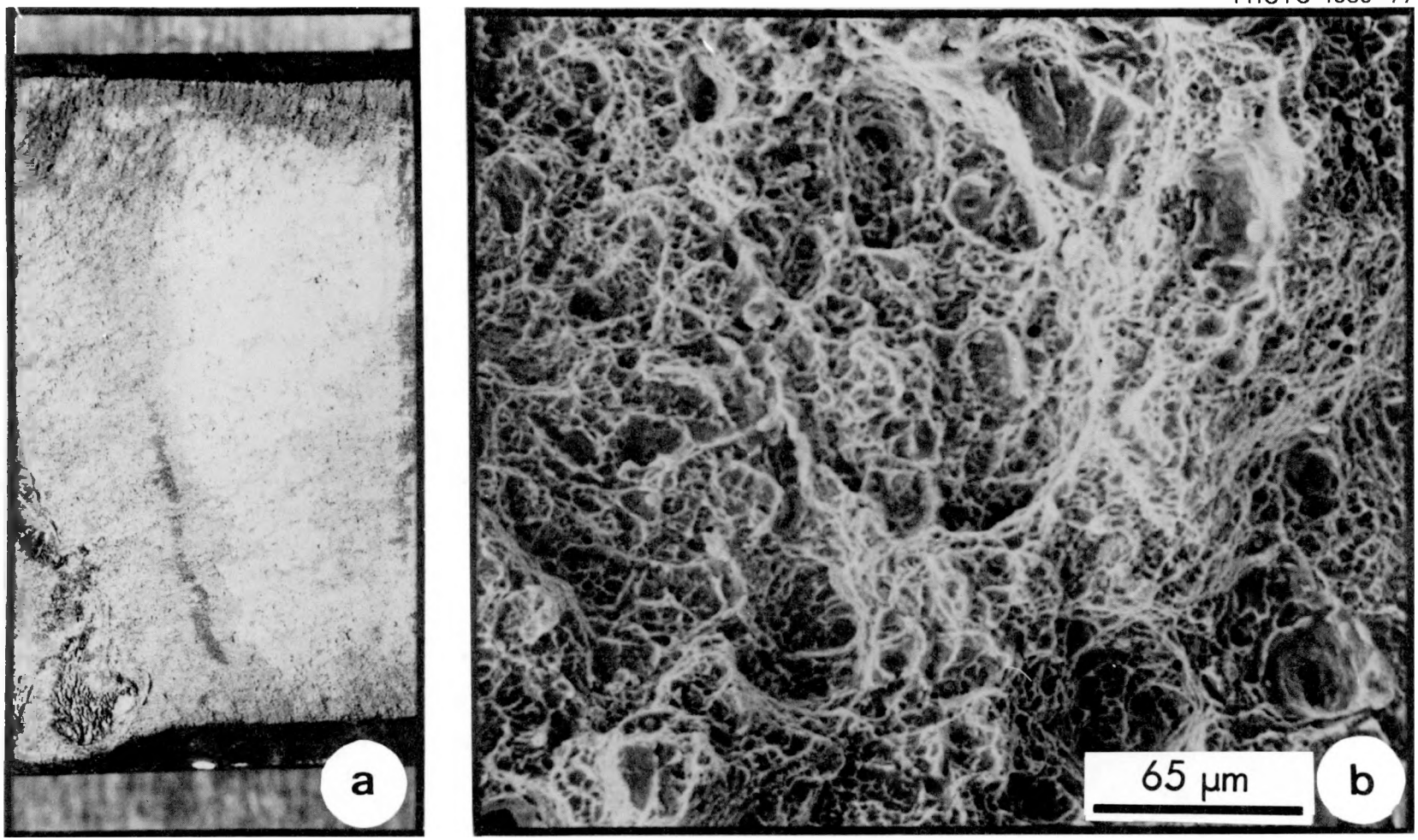

Fig. 5.19. Scanning electron micrographs of the crack-propagation region in crack-arrest model test 2, which was conducted at 4°C (39°F). This region exhibits a dimple fracture mode.

PHOTO 4581–77

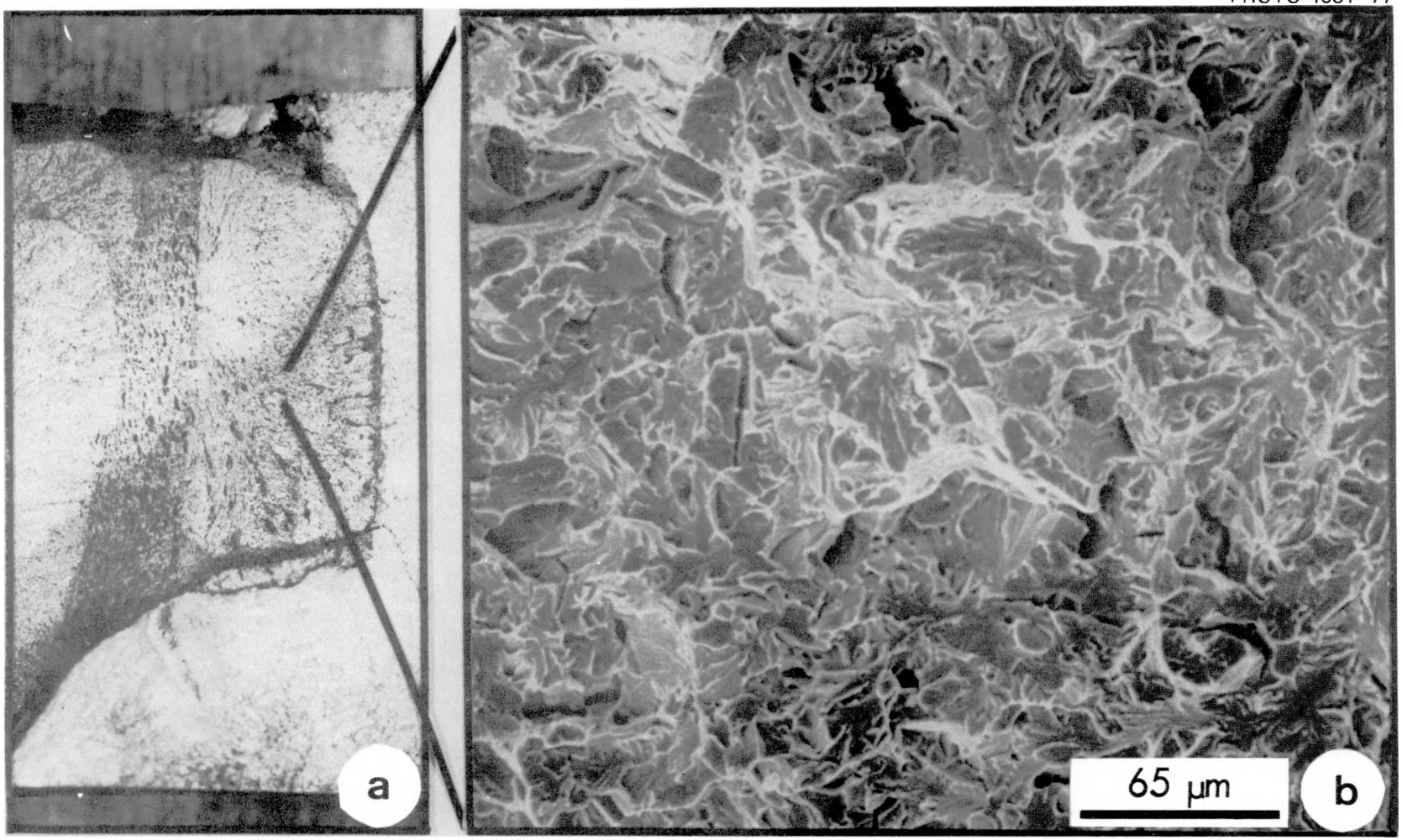

Fig. 5.20. Scanning electron micrograph of the crack-propagation region within the electron-beam fabrication weld in crack-arrest model test 2. The fracture in this region was by the cleavage mode.

PHOTO 4582–77

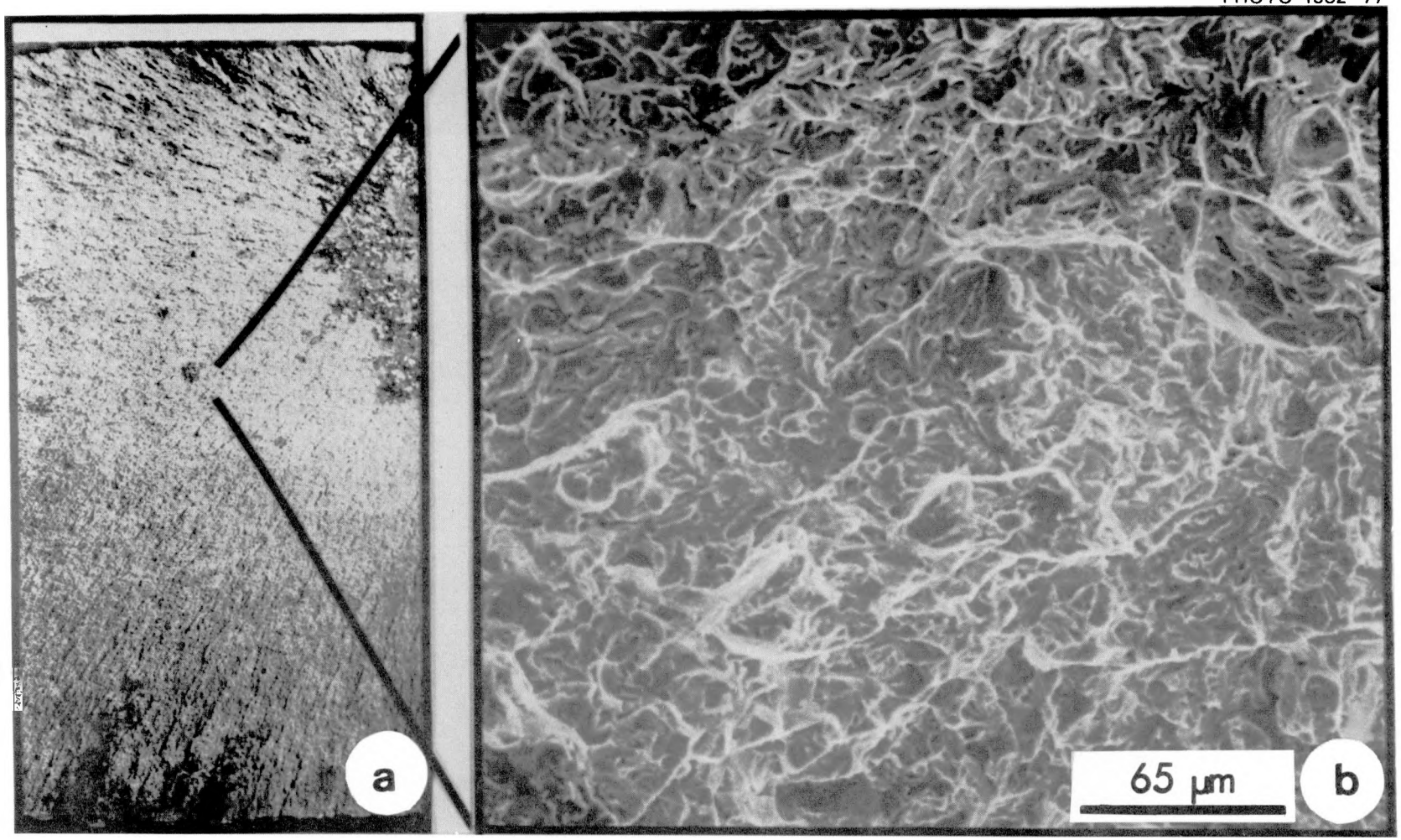

Fig. 5.21. Scanning electron micrographs of the crack-propagation region of the fracture from crack-arrest model test 3. The model was tested at −47°C (−52°F). This region fractured by the cleavage mode.

References

1. P. P. Holz, "Preparations for HSST Intermediate Vessel Tests V-7B and V-8," *Heavy-Section Steel Technology Program Quart. Prog. Rep. January–March 1977*, ORNL/NUREG/TM-120, pp. 36–39.
2. W. J. Stelzman and D. A. Canonico, "Characterization of the Repair Weld in Vessel V-7," *Heavy-Section Steel Technology Program Quart. Prog. Rep. July–September 1976*, ORNL/NUREG/TM-64, pp. 50–55.
3. W. J. Stelzman and D. A. Canonico, "Material Tests for Small Crack Arrest Vessels," *Heavy-Section Steel Technology Program Quart. Prog. Rep. October–December 1976*, ORNL/NUREG/TM-94, pp. 51–52.
4. W. J. Stelzman and D. A. Canonico, "Material Tests for Small Crack-Arrest Vessels," *Heavy-Section Steel Technology Program Quart. Prog. Rep. January–March 1977*, ORNL/NUREG/TM-120, pp. 64–66.
5. G. C. Smith and P. P. Holz, "V-7C Crack-Arrest Model Tests," *Heavy-Section Steel Technology Program Quart. Prog. Rep. January–March 1977*, ORNL/NUREG/TM-120, pp. 44–61.
6. C. E. Childress, *Fabrication History of the Third and Fourth ASTM A533 Steel Plates of the Heavy-Section Steel Technology Program*, ORNL-4313-2 (February 1970).
7. G. T. Hahn et al., *Critical Experiments, Measurements, and Analyses to Establish a Crack Arrest Methodology for Nuclear Pressure Vessel Steels*, BMI-NUREG-1959, pp. 5–14, October 1976.
8. P. B. Crosley and E. J. Ripling, "Plane Strain Crack Arrest Characterization of Steels," *Trans. ASME, Ser. J, J. Pressure Vessel Technol.* 97, 291–98 (1975).
9. J. Miklowitz, "Elastic Waves Created During Tensile Fracture — The Phenomenon of a Second Fracture," *J. Appl. Mech.* 20, 122–30 (1953).

6. THERMAL SHOCK INVESTIGATIONS

R. D. Cheverton S. E. Bolt

6.1 Introduction

During this reporting period for the LOCA-ECC Thermal Shock Program, studies were continued in connection with the possible use of cryogenic quenching in a demonstration of warm prestressing, and further progress was made in the development of a three-dimensional finite-element fracture mechanics code.

6.2 Cryogenic Quenching

6.2.1 Scope of ORNL studies

The possibility of thermally shocking flawed cylindrical test specimens with liquid nitrogen was considered early in the thermal shock program. However, at that time we were not aware of a practical means for eliminating the vapor blanket (film boiling) that normally insulates a specimen from the liquid nitrogen until the superheat falls below a few degrees. For that reason, the concept was abandoned in favor of the present alcohol-water loop,[1] which has been satisfactory for the four thermal shock experiments (TSE-1, -2, -3, -4) conducted thus far.

Now we are considering the possibility of demonstrating warm prestressing in a cylinder under thermal shock conditions. The present test facility is not adequate for the task,[2] but the French have recently acquainted us with a way of substantially increasing the rate of heat transfer when using liquid nitrogen. A thin layer of insulating material is applied to the heat transfer surface so that initially the heat flux will be low enough to prevent formation of the vapor blanket. Results of experiments conducted by the French in connection with their thermal shock program show that the corresponding initial heat transfer coefficient is large compared to that for a vapor blanket and increases with decreasing surface temperature.

The French experiments were limited to conditions that are not necessarily typical of our thermal shock test situation, and thus we instigated a modest cryogenic-quench thermal-hydraulic experimental program at ORNL to obtain additional data. Parameters that needed to be included were initial temperature of the test specimen, specimen configuration (hollow cylinders with various length-to-diameter and flow-area-to-surface-area ratios), and a means of applying the coolant to the surface (submergence, forced convection, spray, etc.). The French data were limited to an initial temperature of 30°C (86°F) and to submergence of a 16-mm-diam by 48-mm-long (0.63-in.-diam × 1.89-in.-long) solid cylinder.

As discussed in Ref. 3, French heat transfer data were used by ORNL in a calculation of warm-prestress parameters associated with a cryogenic quench of a 991-mm-OD × 686-mm-ID (39-in.-OD × 27-in.-ID) thermal shock test specimen. Warm prestressing did not take place, apparently because the initial temperature was too low. Even if the low initial temperature had been adequate, it is suspected that the heat transfer coefficient would have been affected by differences in hydrodynamics between the French experiment and the internal quenching of a relatively large hollow cylinder. Certainly the question of axial uniformity must be answered.

The specific material for the thin insulating coating is another parameter of interest. Ideally, the material should have a very low thermal conductivity and, once applied, should have a high density of nucleation sites; also, it must be able to withstand the necessary initial temperature and the severe thermal shock imposed during a warm-prestress experiment. The French tried several coatings and found 3M-Brand Spray Adhesive 77 (3M-77) made by Minnesota Mining and Mfg. Co. to be suitable. It provided a substantial increase in the heat transfer coefficient and remained intact after several thermal shocks. This material is not necessarily the best, but a search for a better one could be very time consuming and is not an active part of our program at this time.

Our approach to obtaining appropriate heat transfer data has been to first repeat the French experiments with a 13-mm-diam (0.51-in.) solid steel cylinder and then to graduate to successively larger hollow cylinders that in most cases would be insulated on the outside and quenched on the inside. Initially, the specimens would be submerged, allowing maximum natural

convection; but eventually submerged, restricted-flow experiments would be conducted, and, if necessary, other means of applying the coolant would be considered.

Thus far, four different test specimens have been used in the testing program:

1. a 13-mm-diam × 50-mm-long (0.5-in.-diam × 2-in.-long) solid cylinder,
2. a 67-mm-ID × 89-mm-OD × 127-mm-long (2.6-in.-ID × 3.5-in.-OD × 5-in.-long) cylinder,
3. a 146-mm-ID × 168-mm-OD × 152-mm-long (5.8-in.-ID × 6.6-in.-OD × 6-in.-long) cylinder — referred to as the 6 × 6 cylinder,
4. a 127-mm-ID × 178-mm-OD × 508-mm-long (5-in.-ID × 7-in.-OD × 20-in.-long) cylinder — referred to as the 7 × 20 cylinder.

Testing of these specimens is essentially complete, and plans are under way to conduct thermal-hydraulic experiments with TSV-F [241-mm-ID × 533-mm-OD × 914-mm-long (9.5-in.-ID × 21-in.-OD × 36-in.-long) cylinder]. A photograph of the smaller test specimens is shown in Fig. 6.1; the 7 × 20 specimen and the tank in which all specimens are submerged are shown in Fig. 6.2.

Based on the information obtained to date, it appears that a warm prestress experiment will be possible with a 686-mm-ID × 991-mm-OD × 1370-mm-long (27-in.-ID × 39-in.-OD × 54-in.-long) cylinder, using an initial temperature of 127°C (256°F). However, testing of TSV-F is required to confirm this tentative conclusion. Pertinent results obtained with the 6 × 6 and 7 × 20 cylinders during this reporting period are discussed in the following subsections.

6.2.2 Optimum thickness of coating

There is an optimum thickness of the insulating coating associated with a minimum quench time, and it appears that this thickness increases with increasing initial temperature. Measurements of the thickness have not been very accurate, and the method of spraying has not always been consistent, since the techniques are still being developed. Thus, accurate values of thickness vs initial temperature are not available. However, for the early experiments, which were conducted with initial temperatures

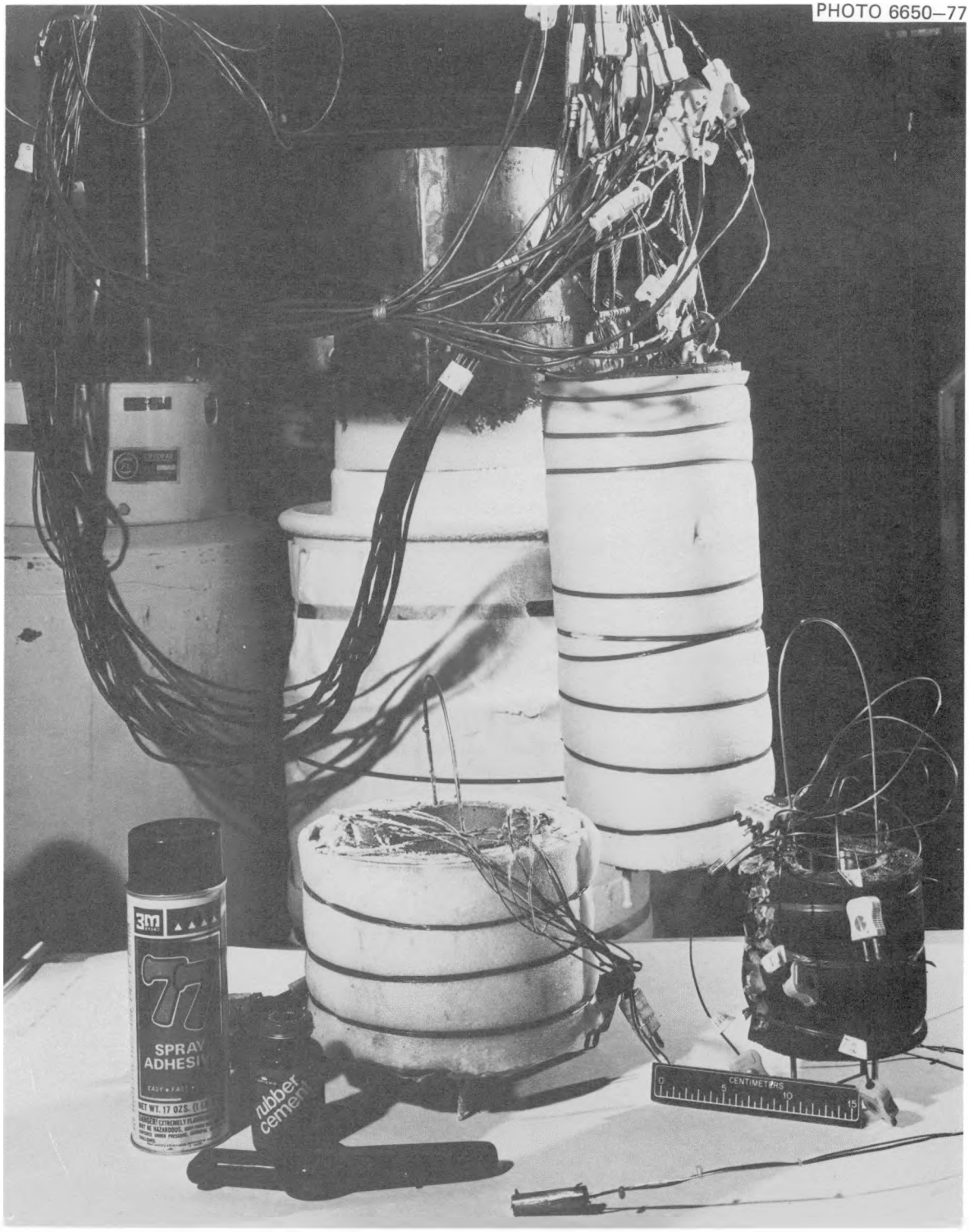

Fig. 6.1. Cylindrical test specimens used in the initial cryogenic-quench thermal-hydraulic experiments.

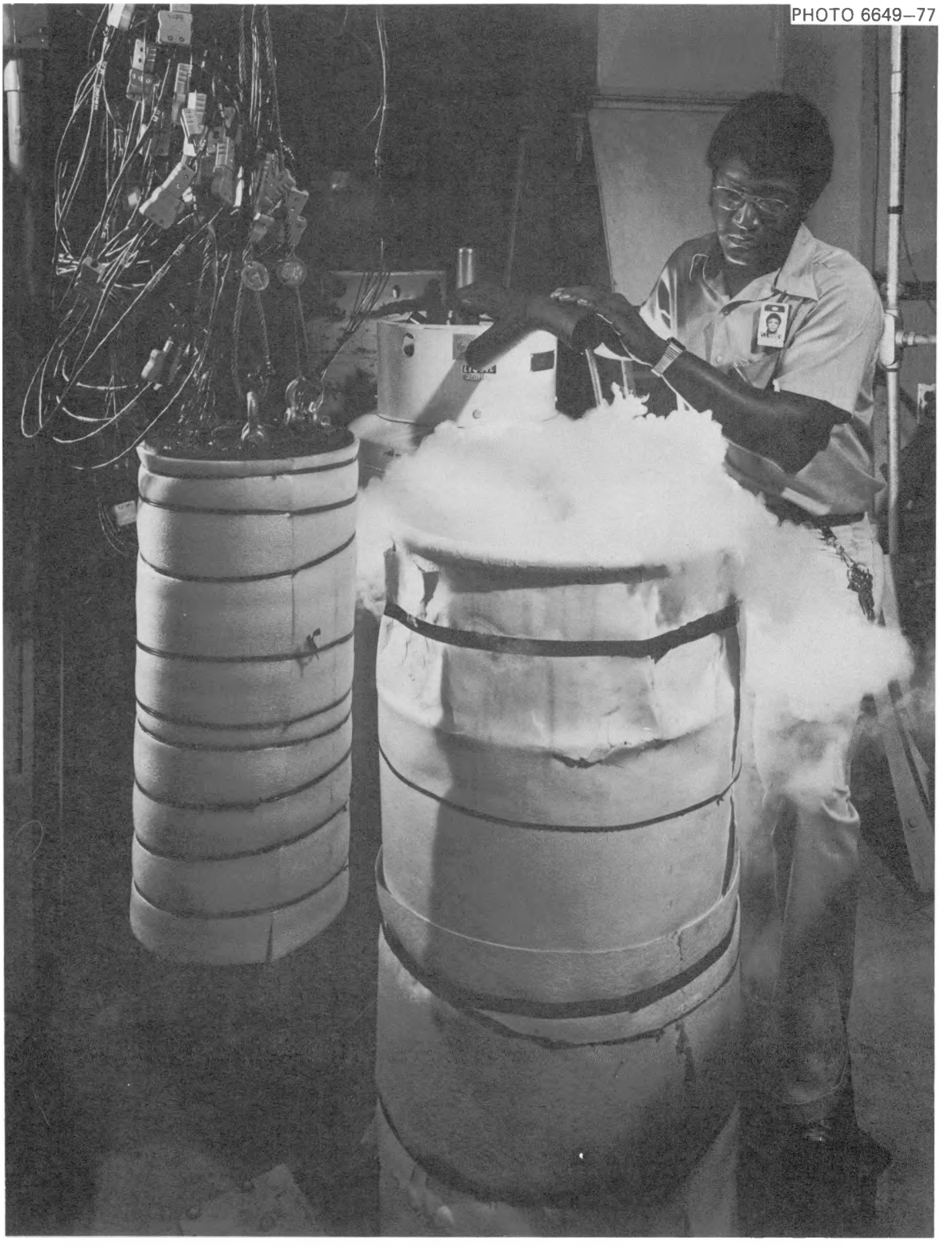

Fig. 6.2. Photograph of the 7 × 20 cryogenic-quench test cylinder and the insulated liquid nitrogen tank in which the test specimens are submerged.

of ∿25°C (77°F), it appeared that the optimum coating of 3M-77 on the 6 × 6 cylinder consisted of "two coats" sprayed from a distance of ∿450 mm (18 in.) with 5 min of drying time between coats. A single coat consisted of spraying for ∿6 sec through the top opening and ∿6 sec through the bottom opening.

Since it became apparent that an initial temperature of ∿120°C (250°F) would be required to achieve the desired warm-prestress characteristics, a greater effort was expanded to determine the optimum thickness of 3M-77 for an initial temperature of 120°C. The coating was applied to the inner surface of the 6 × 6 cylinder in the manner described above. Plots of temperature vs time [temperature measured at a distance of 0.56 mm (0.022 in.) from the inner surface] for five through ten coats are shown in Fig. 6.3. Based on quench time, eight coats is the optimum number.

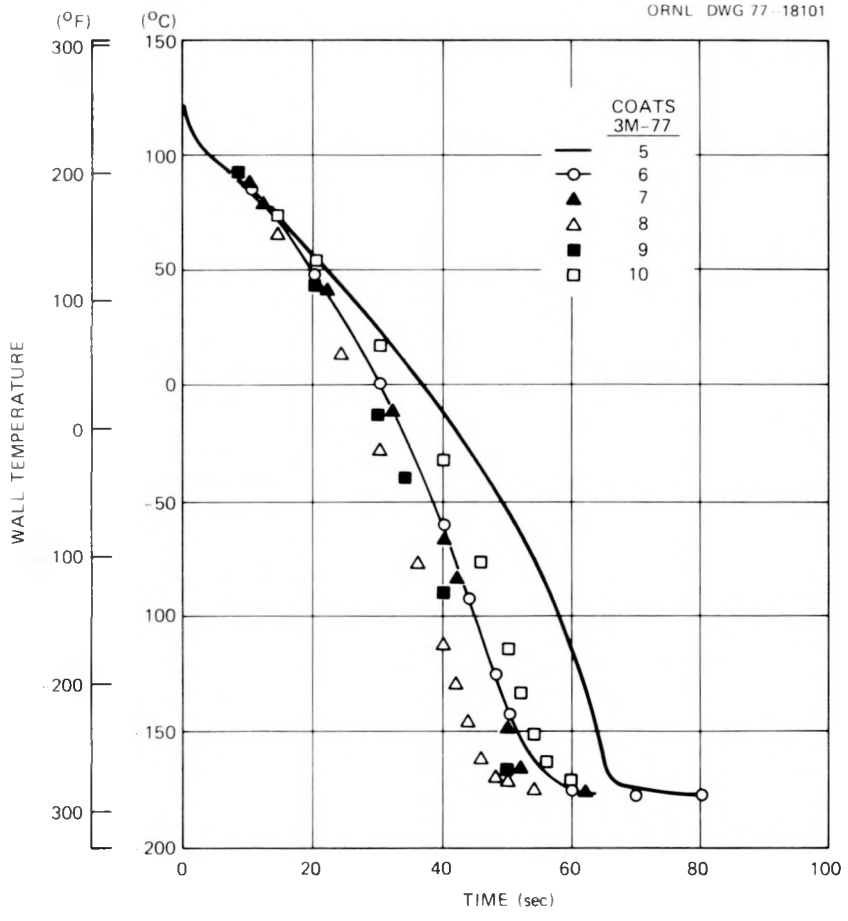

Fig. 6.3. Determination of optimum coating thickness for 3M-77 based on minimum quench time (wall temperature vs time). Temperature measured at a radial distance from inner wall of 0.56 mm (0.022 in.).

Following the application of each coating, attempts were made to measure the coating thickness using a magnetic device (Mikrotest, Nordson Corporation; see Fig. 6.1). It appears that the thickness of a single coating is ∿0.05 mm (0.002 in.), and thus the optimum thickness for an initial temperature of 120°C (250°F) would be ∿0.4 mm.

An exact interpretation of coating thickness, using the magnetic device, is difficult because the coating surface is quite rough, as it should be to create nucleation sites. In an effort to obtain more specific information with which to duplicate coating thickness, the coating was removed mechanically from the 6 × 6 cylinder following the above optimization study and weighed. The 10 coatings weighed 0.13 mg/mm^2.

6.2.3 Effect of initial temperature

Experiments were conducted using the 6 × 6 cylinder with initial temperatures of 24°C (75°F), 66°C (150°F), 93°C (200°F), ∿121°C (250°F), and 149°C (300°F). Near-optimum coatings of 3M-77 were applied for each initial temperature. Heat transfer coefficients as a function of metal surface temperature for initial temperatures up to 129°C (267°F) were deduced from the quench experiments and were found to be in good agreement over the applicable temperature ranges. A curve of heat transfer coefficient vs metal surface temperature for an initial temperature of 129°C (267°F) is shown in Fig. 6.4. This curve corresponds to six coats of 3M-77.

Experiments conducted with an initial temperature of ∿150°C (302°F) indicated considerably lower heat transfer coefficients over the entire temperature range. It appears that the characteristics of 3M-77 coating suffer a permanent change at temperatures above ∿130°C (266°F).

Fracture mechanics calculations were made for the 991-mm-OD (39-in.) cylinder with a long axial crack using different initial temperatures and the corresponding heat transfer vs temperature curves. The results are presented in Fig. 6.5 in the form of K_I vs time for a fractional crack depth (a/w) of 0.5, showing the times at which a K ratio (K_I/K_{Ic}) of unity is achieved. A fractional crack depth equal to 0.5 is about the largest that should be considered from the standpoint of the accuracy of the linear elastic fracture mechanics method of analysis; for smaller

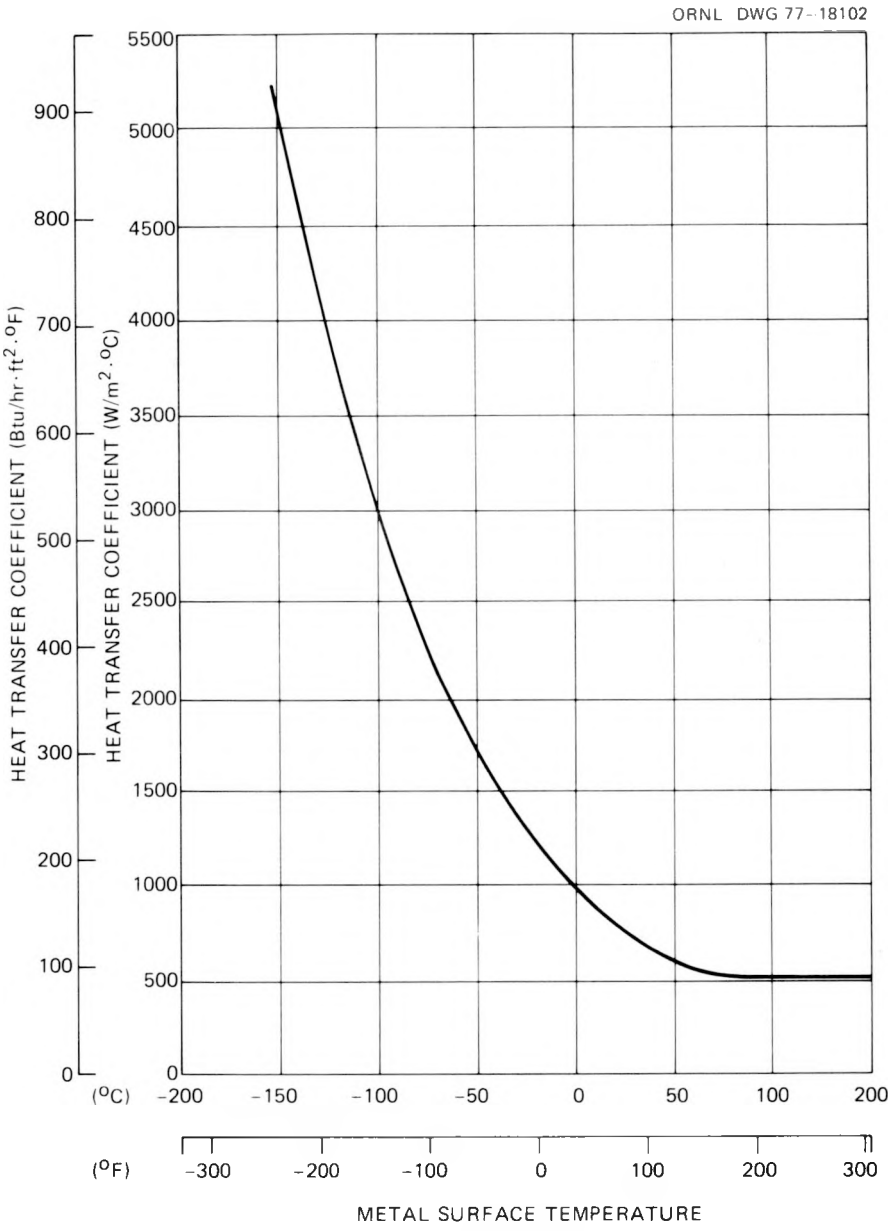

Fig. 6.4. Heat transfer coefficient vs metal surface temperature as derived from cryogenic-quench (liquid nitrogen) experiments with the 6 × 6 cylinder with near-optimum coating thickness of 3M-77 and with an initial temperature of 129°C (264°F).

values, the point of $K_I/K_{Ic} = 1$ is farther to the left of the peak in the K_I vs t curve. Thus, Fig. 6.5 indicates approximately the maximum degree of warm prestressing that can be achieved as a function of initial temperature. [For T_i = 93°C (200°F), the coating characteristics were substantially less than optimum.] These results show that increasing the initial

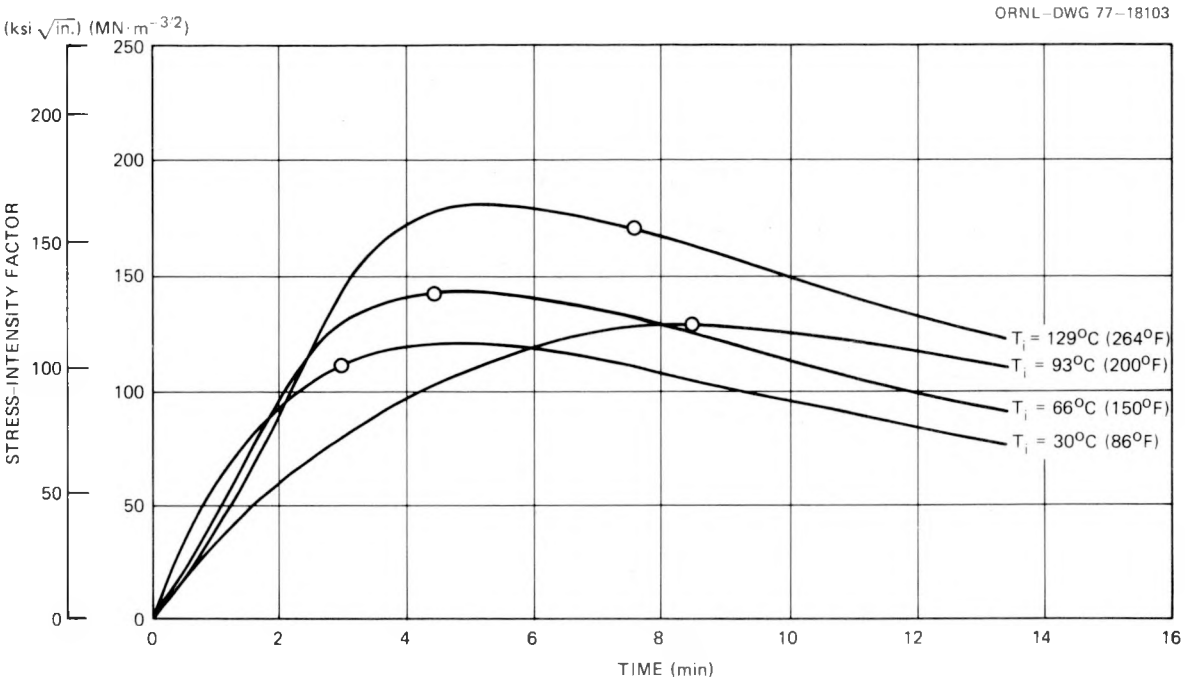

Fig. 6.5. Stress-intensity factor vs time for a long axial crack (fractional depth 0.50) in the 991-mm-OD (39-in.) specimen when the specimen is subjected to a liquid nitrogen quench. Initial temperature is a parameter, and the corresponding times at which $K_I/K_{Ic} = 1$ are indicated by open circles.

temperature increases the degree of warm prestressing, at least up to 129°C (264°F). The primary effect of increasing the temperature is to increase the material toughness and thus postpone the time at which the K ratio achieves unity. In this regard, it is of interest to note that the K_{Ic} vs temperature curve used in these calculations corresponds to tempered material (the same used for the PWR reference calculational model[1] assuming $RT_{NDT} = 0°F$) rather than the as-quenched material used in TSE-1, -2, -3, and -4.

6.2.4 Fracture mechanics calculations for an initial temperature of 129°C (264°F)

On the basis of the cryogenic-quench studies conducted thus far, it appears that the degree of warm prestressing increases with increasing initial temperature, that the 3M-77 coating is limited to an upper temperature of ∿130°C (265°F), and that warm prestressing can be achieved

with this initial temperature in the 991-mm-OD (39-in.-OD) cylinder. However, for such an experiment to be feasible, the calculated degree of warm prestressing must be sufficient to cover uncertainties in the predicted thermal shock, K_I, and K_{Ic}, so that the time of occurrence of $K_I/K_{Ic} = 1$ will indeed be after the time that K_I reaches a maximum. Furthermore, the calculated maximum value of K_I/K_{Ic} must be large enough to ensure that the flaw will propagate in the absence of warm prestressing. Otherwise, the experiment would not be valid.

Detailed thermal and fracture mechanics calculations were made for the 991-mm-OD (39-in.) cylinder assuming a long axial flaw, tempered material as referenced above, an initial temperature of 129°C (264°F), and the heat transfer coefficient vs temperature curve obtained with the 6 × 6 cylinder (Fig. 6.4) and corresponding to an initial temperature of 129°C. Figure 6.6 shows plots of K_I, K_I/K_{Ic}, and temperature vs time, with fractional crack depth (a/w) and RT_{NDT} as parameters. As indicated, the degree of warm prestressing increases with increasing crack depth and decreasing RT_{NDT}, while $(K_I/K_{Ic})_{max}$ decreases. It is also of interest to note that for $RT_{NDT} = -17.7°C$ (0°F), the temperature at the tip of the crack corresponding to $K_I/K_{Ic} = 1$ is ∿10°C (∿50°F), which is in the transition region. This is similar to the situation for which calculations were made for the PWR reference calculational model (see Ref. 2) assuming the minimum crack depth that will result in warm prestressing (a/w = 0.2).

Acceptable minimum values of $(K_I)_{max}/(K_I)_1$, where $(K_I)_1$ is the K_I value when $K_I/K_{Ic} = 1$, and $(K_I/K_{Ic})_{max}$ to account for the uncertainty in K_{Ic} are ∿1.1 and 1.4, respectively. As indicated in Fig. 6.6, there is no problem in achieving the minimum acceptable value of $(K_I/K_{Ic})_{max}$ for flaw depths up to ∿70%. If a maximum flaw depth of 50% is imposed, then $K_I)_{max}/(K_I) \geq 1.1$ for $RT_{NDT} \leq -29°C$ (−20°F).

6.2.5 Variation in quenching along length of cylinder

Since the test cylinder is being quenched with a boiling liquid (liquid nitrogen), there is no increase in liquid temperature along the length of the cylinder. However, a large volume of vapor is generated that could alter the heat transfer regime along the length. This possibility was investigated using the 7 × 20 cylinder, which has a length-to-diameter ratio

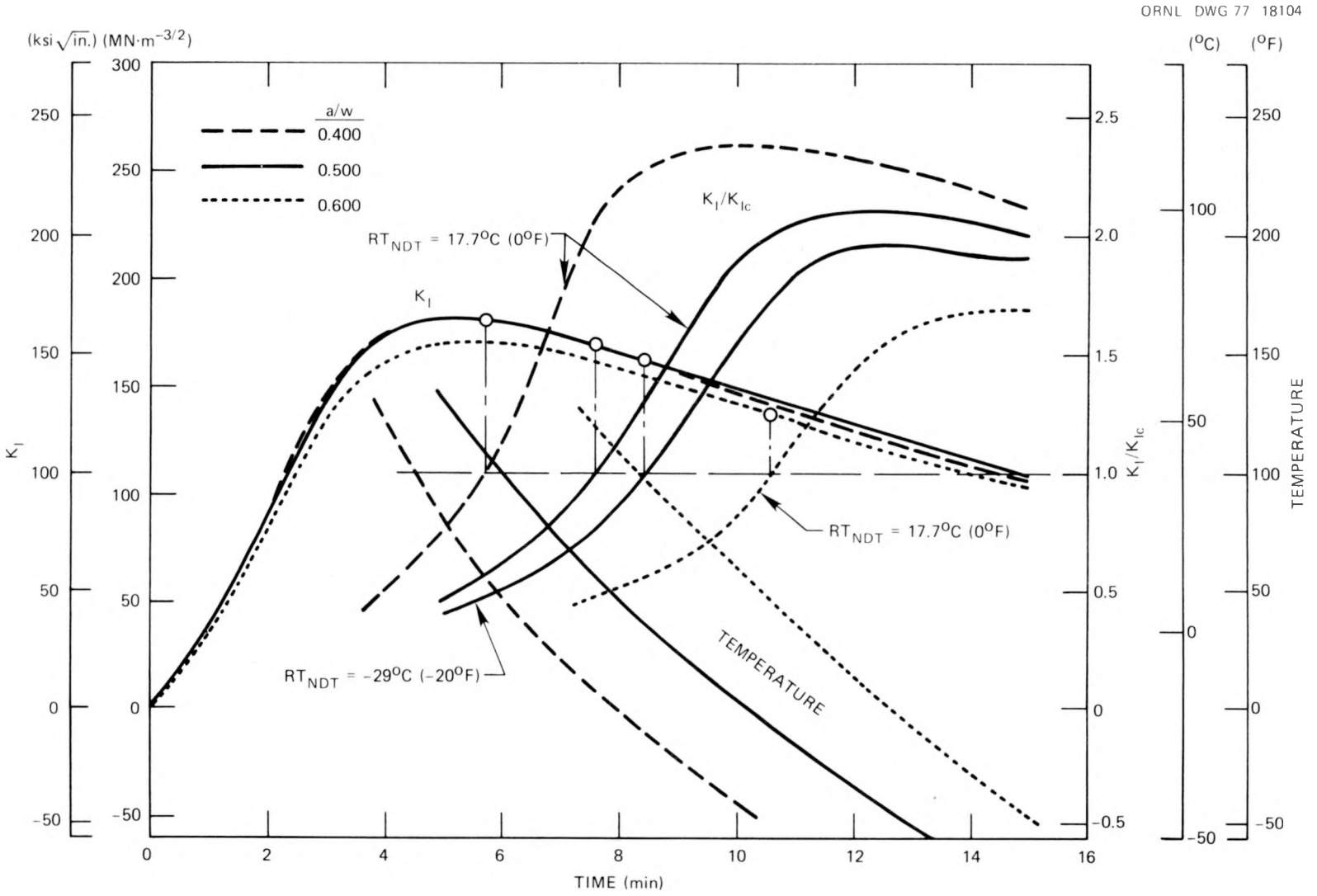

Fig. 6.6. K_I, K_I/K_{Ic}, and crack-tip temperature vs time for a liquid nitrogen quench of the 991-mm-OD (39-in.) cylinder in the tempered condition and containing a long axial crack. Fractional crack depth (a/w) and RT_{NDT} are parameters; the initial temperature was 129°C (264°F).

equal to that for the proposed 991-mm-OD (39-in.) test specimen but a smaller flow-area-to-surface-area ratio, which is proportional to the inside diameter. (This latter inequality tends to favor the larger specimen in terms of axial uniformity.)

The 7 × 20 cylinder was too small in diameter and too long for the inner surface to be sprayed with 3M-77. Thus, as was done in many very early experiments,[3] the inner surface was coated with rubber cement by filling the cavity with rubber cement and then letting the excess drain out the bottom. Rubber cement applied in this manner does not provide as many nucleation sites but otherwise serves as a satisfactory coating.

With a single coating of rubber cement, there was a wide variation in quenching time for different points along the length of the cylinder, the bottom end quenching faster than the upper, as shown in Fig. 6.7. Part of the nonuniformity was due to a slight taper in the coating thickness, which was determined by repeating the experiment with the cylinder inverted. However, most of the variation is a result of some thermal-hydraulic phenomenon.

The knees in the curves in Fig. 6.7 indicate that the coating thickness was less than optimum. For this reason, a second coat was applied, this time with the cylinder inverted to achieve a uniform total thickness, and then the experiments were repeated. The results are shown in Fig. 6.8. It is apparent that the quenching was quite uniform along the entire length. This is very encouraging because a larger-diameter cylinder with the same length-to-diameter ratio should have a more uniform temperature distribution. A possible exception could result from a higher heat removal rate (greater vapor generation rate) achieved in the larger cylinder with the 3M-77 coating. The only way to investigate this possibility is to conduct tests with larger cylinders, and this is planned.

6.2.6 Restricted flow

As mentioned earlier, it is undesirable to submerge the proposed 991-mm-OD (39-in.) test specimen, and without submergence the natural convection loop achieved with the smaller test specimens will not exist. It is planned to provide some forced convection with a cryogenic pump, the amount depending on the beneficial effects of the present natural

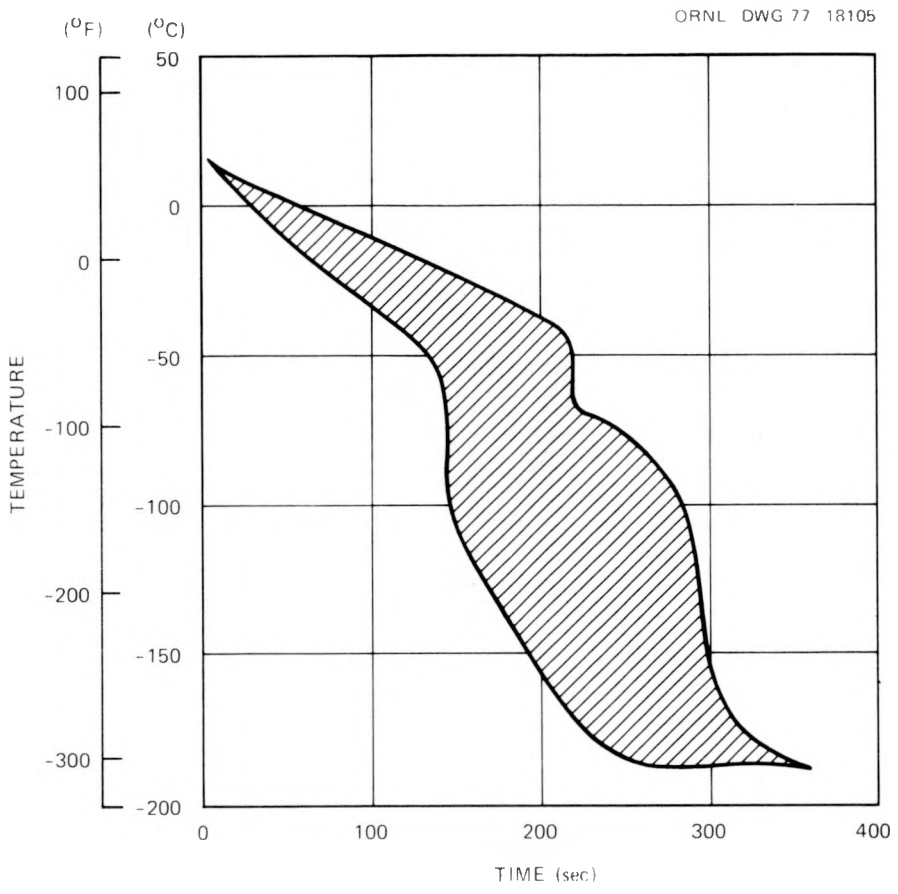

Fig. 6.7. Temperature vs time for several positions along the length of the 7 × 20 cylinder during a liquid nitrogen quench from room temperature with one coat of rubber cement applied. The radial positions of the thermocouples are in the range 0.30 to 0.58 mm (0.012 to 0.023 in.) from the inner surface.

convection, to compensate for this lack of natural convection. Restricted flow experiments were conducted with the 6 × 6 and the 7 × 20 cylinders to determine the extent to which the open-ended configuration enhances the heat transfer coefficient. Figure 6.9 shows plots of temperature vs time for the 6 × 6 cylinder with the bottom of the cylinder open and also with it closed. As indicated, the open-bottom condition is beneficial but not to a large degree. Figure 6.10 shows plots of temperature vs time for the 7 × 20 cylinder with the bottom closed. This figure shows a greater spread in axial temperatures than Fig. 6.8, which indicates a beneficial effect of the greater degree of convection with the bottom open.

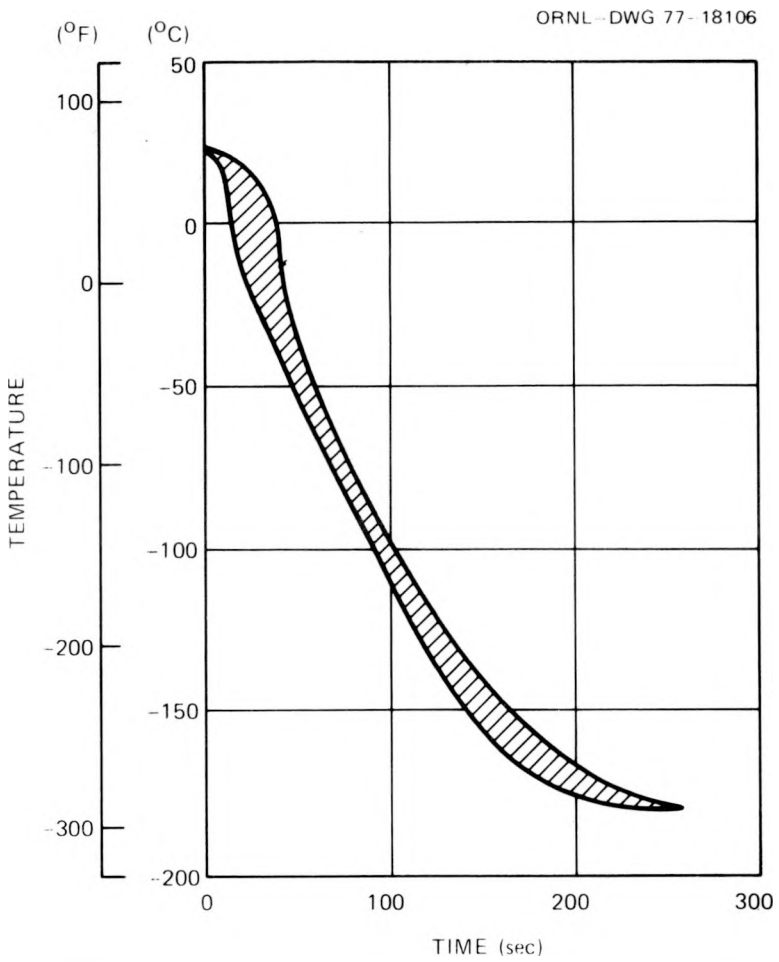

Fig. 6.8. Temperature vs time for several positions along the length of the 7 × 20 cylinder during a liquid nitrogen quench from room temperature with two coats of rubber cement applied. The radial positions of the thermocouples are in the range 0.30 to 0.58 mm (0.012 to 0.023 in.) from the inner surface.

The above results indicate that some forced convection will be necessary in a closed-bottom experiment. The exact amount cannot be implied from these results, but is appears that a rather nominal flow rate will be sufficient. The necessary amount will be determined in a subsequent experiment.

6.2.7 Proposed experiments with TSV-F [533-mm-OD (21-in.) cylinder]

The next step in the cryogenic-quench thermal-hydraulic experiments is to conduct tests with TSV-F in a manner similar to that proposed for

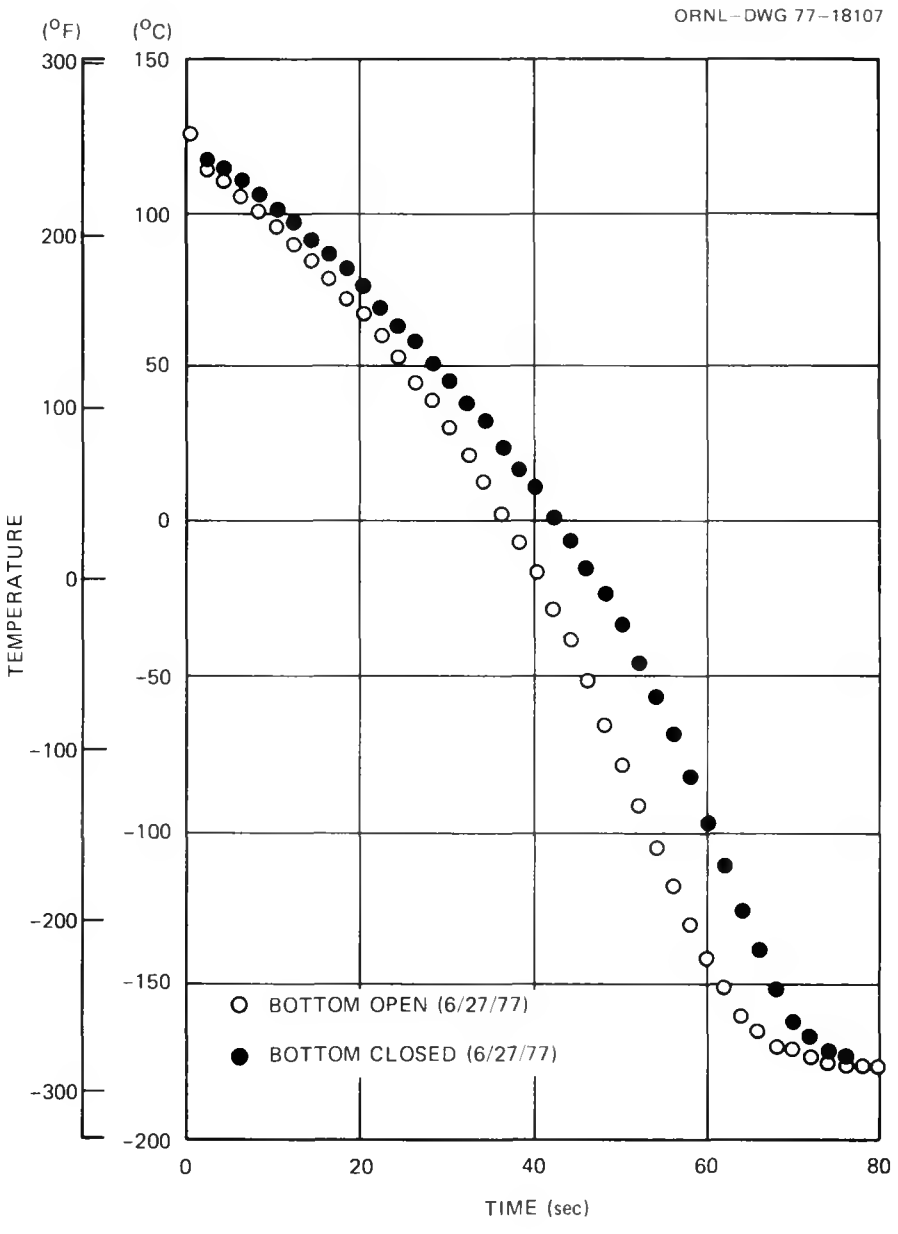

Fig. 6.9. Temperature at a depth of 0.56 mm (0.022 in.) vs time for the 6 × 6 cylinder quenched in liquid nitrogen from an initial temperature of ∿125°C (257°F) showing the effect of closing the bottom end to flow. The inner surface was covered with nine coats of 3M-77.

the 991-mm-OD (39-in.) cylinder. Furthermore, we must learn to apply a uniform coating of 3M-77 to TSV-F with an adequate surface density of nucleation sites. In this regard, preliminary experiments are being conducted with 250-mm-ID (10-in.) pipe. The pipe section is rotated in a lathe, and the 3M-77 spray can is fed through the pipe by the lathe

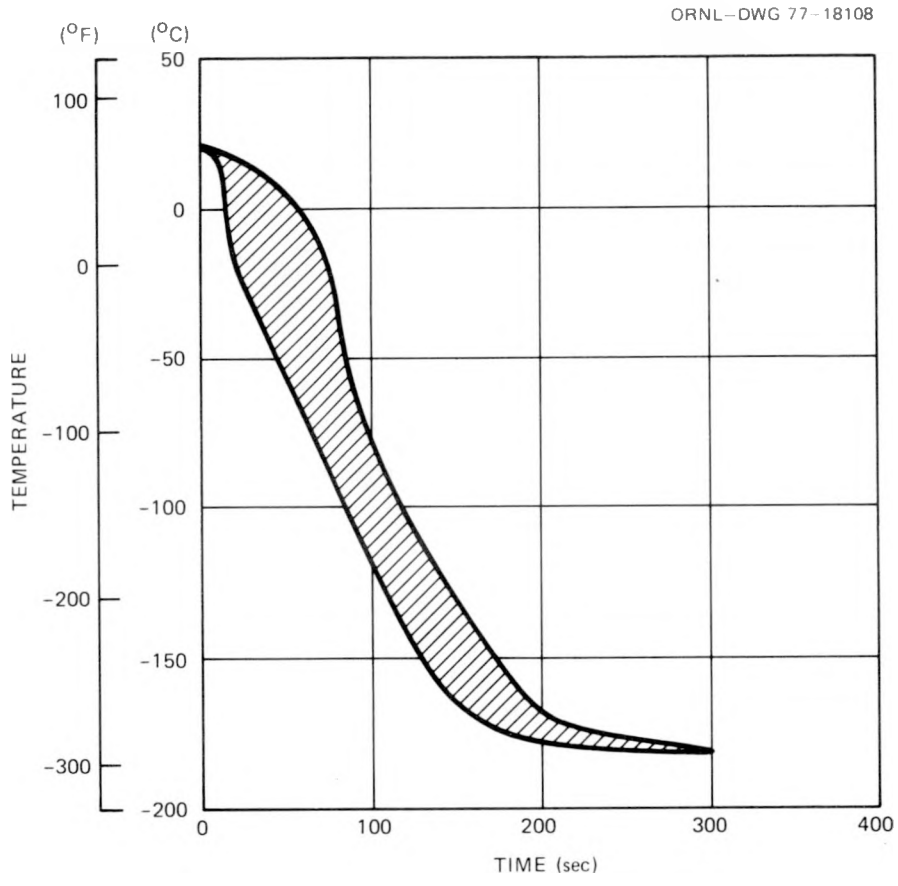

Fig. 6.10. Temperature vs time for several positions along the length of the 7 × 20 cylinder during a liquid nitrogen quench from room temperature with two coats of rubber cement applied. The radial positions of the thermocouples are in the range 0.30 to 0.58 mm (0.012 to 0.023 in.) from the inner surface. The bottom of the specimen was closed to flow.

carriage to which the can is attached. Results obtained thus far look encouraging.

A schematic of the cryogenic-quench TSV-F test facility is shown in Fig. 6.11. The test specimen (TSV-F) will be supported in the existing thermal shock test facility, but will not be hydraulically connected to the loop. Instead, a 300-mm-diam × 2-m-long (11.8-in. × 6.56-ft) liquid nitrogen reservoir will be attached to the top end of TSV-F. The reservoir cavity will initially be separated from the test specimen cavity by a rupture disk. Prior to the thermal shock, the test specimen will be heated to the desired initial temperature [∿125°C (257°F)] with the existing clamshell furnace, the reservoir will be filled with liquid nitrogen,

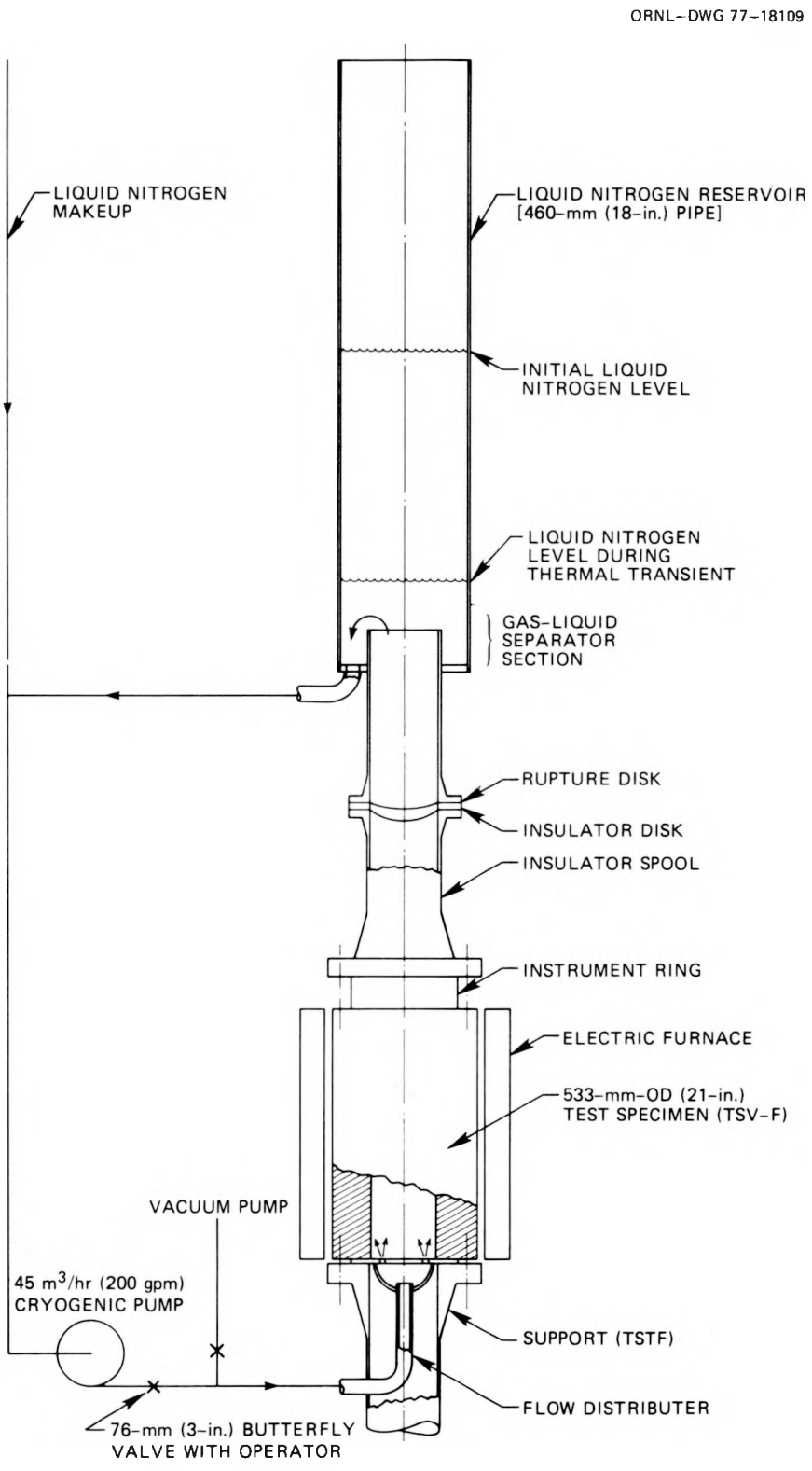

Fig. 6.11. Schematic of the test facility for subjecting TSV-F to a cryogenic thermal shock.

and a vacuum will be pulled in the test specimen cavity. The thermal shock will be initiated by mechanically rupturing the disk, thus allowing a slug of liquid nitrogen to drop into the test specimen cavity. Immediately following this event, the circulation pump will be put into operation, and liquid nitrogen makeup will be started. A paddle wheel attached to the shaft of a stirring motor will be used to centrifugally separate the liquid and vapor at the pump inlet connection to the reservoir. About 1.5 m^3 (400 gal) of liquid nitrogen will be consumed in the experiment. The necessary components for the facility are being acquired at this time.

6.3 Development of a Three-Dimensional Finite-Element Fracture Mechanics Code

S. K. Iskander

During this quarter, several studies have been made to assess the adequacy of the model to be used in the three-dimensional studies. Using the two-dimensional counterpart, the minimum number of elements (in two dimensions) that may be used has been determined.

The 8-node isoparametric element (the two-dimensional counterpart of the three-dimensional 20 node isoparametric brick element) has a quadratic interpolating function for the displacements that allows the use of fewer elements than the bilinear triangle or quadrilateral.

A mesh-generation program has been written that produces the necessary data for the ADINA finite-element computer program. By specifying the number of radial and circumferential elements as well as a geometric "progression" factor, data for meshes such as the one shown in Fig. 6.12 can be generated. Here, there are 6 elements radially, 12 circumferentially, and a circumferential progression factor of 0.9. Geometric progression factors allow either the radial or circumferential divisions to become progressively smaller as a region of high stress gradients is approached.

The temperature distribution in the cylinder is a function of the radial distance only; therefore, stress gradients are present in the radial direction only. Hence, the problem is determining the minimum

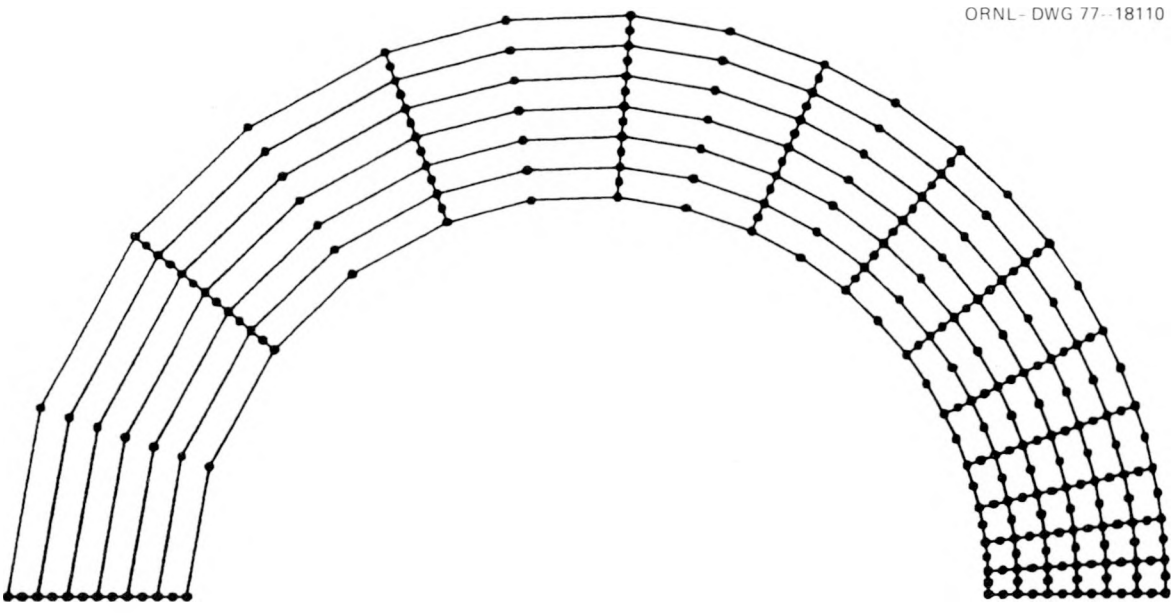

Fig. 6.12. Proposed basic model for three-dimensional analysis of an axial crack in a cylinder.

number of elements in the radial direction to adequately model the temperature gradient. The requirements in the circumferential direction are less stringent, being dictated by general finite-element considerations.

A small computer program was also written that will interpolate the temperature data generated by HEATING5 (Ref. 4) and produce temperature data in a form suitable for ADINA.

The results of these studies are shown in Fig. 6.13. The solid line labeled "Temperature" is obtained by fitting piecewise cubic splines through the temperature data produced by HEATING5. The solid line labeled "stress" is the circumferential stress obtained by numerically integrating the closed-form solutions for thick cylinders subjected to radial temperature gradients. For this reason, it may be considered to be an "exact" solution. Three, four, and six elements equally spaced radially were modeled. As can be seen, the three- and four-element models are inadequate for modeling the temperature distribution, and as a result, the stresses are also inaccurate compared to the closed-form solutions. In Fig. 6.13, the symbols represent the values calculated at the "Gaussian" sampling points by the computer program.

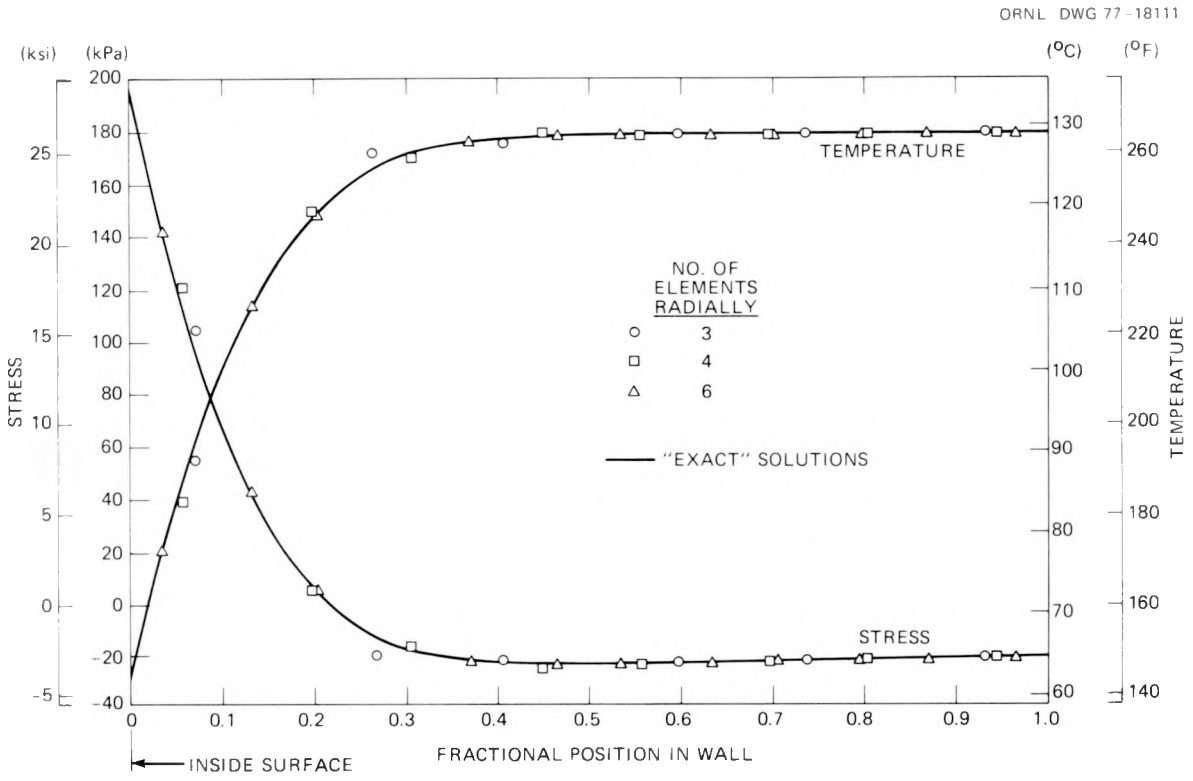

Fig. 6.13. Comparison between results of the ADINA finite-element solution and the closed-form solution for different numbers of radial elements.

In the next quarter, a crack will be modeled at a/w = 0.5, and the results will be compared to those obtained by a different computer analysis.[5] The model will then be extended to three dimensions by converting the same basic model of the 8-node element to its 20-node counterpart.

References

1. R. D. Cheverton, *Pressure Vessel Fracture Studies Pertaining to a PWR LOCA-ECC Thermal Shock: Experiments TSE-1 and TSE-2*, ORNL/NUREG/TM-31 (September 1976).
2. R. D. Cheverton, *Heavy-Section Steel Technology Program Quart. Prog. Rep. July–September 1976*, ORNL/NUREG/TM-64, pp. 85–90.
3. R. D. Cheverton, *Heavy-Section Steel Technology Program Quart. Prog. Rep. January–March 1977*, ORNL/NUREG/TM-120, pp. 88–97.
4. W. D. Turner, D. C. Elrod, and I. I. Siman Tov, *HEATING5 – An IBM 360 Heat Conduction Program*, ORNL/CSD/TM-15 (March 1977).

5. S. K. Iskander, *The Calculation of Stress Intensity Factors in Thick Cylinders Subjected to Transient Temperature Gradients by the Finite Element Method*, K/CSD/TM-2 (April 1976).

7. FOREIGN RESEARCH

W. L. Greenstreet

The objective of this task is to systematically collect, maintain, and review products of foreign research that are applicable to safety of light-water reactor (LWR) systems. The areas to be covered are fracture mechanics, metallurgy, welding, and structures fabrication. The validity and usefulness of the results of foreign research for application to the safety and licensing of LWRs are to be identified and recommendations made to the Nuclear Regulatory Commission concerning the application of pertinent well-founded research results.

Lists of foreign reports published in *Nuclear Safety* through Vol. 18, No. 4, have been reviewed to identify topics of interest in the metallurgy and materials areas. An arrangement has been made whereby translated copies will be obtained through the office of A. Spano, Assistant to the Director, Office of Nuclear Regulatory Research. Translated copies of 18 reports have been requested, and original-language copies of 10 of these non-English-language documents were acquired. Projects of interest listed in the reports, *OECD, Nuclear Energy Agency — International Energy Agency, Nuclear Safety Research Index,* 1976, and *European Community Light Water Reactor Safety Research Projects, Experimental Issue,* EUR 5394e, 1975, have been identified, and descriptive summaries have been compiled to aid in the following activities being carried out by the various organizations in different countries.

On June 7 and 8, 1977, Klaus Rahka of the Technical Research Center of Finland visited Oak Ridge National Laboratory and discussed high-temperature mechanical property studies on structural alloys; fuel cladding studies; and data acquisition, storage, and retrieval methods with personnel in the Metals and Ceramics Division. He also discussed research activities under the major task areas of the HSST program with appropriate program personnel. One objective of his visit was to gain information for better defining areas for information exchange between the Nordic Group (Denmark, Finland, Norway, and Sweden) and the U.S. Nuclear Regulatory Commission in order to consummate an agreement which embraces HSST

program—related areas. Up to this time, proposals made by the Nordic Group have lacked needed specificity.

8. PCRV TENDON CORROSION STUDIES

J. C. Griess

During this quarter, an analysis of the corrosion of prestressing steel tendons in concrete pressure vessels was completed. This analysis consisted of a review of the literature on the corrosion of high-strength steels in aqueous solutions, in concretes, and in protective organic greases, and an identification of areas in which additional experimental work is required. Because of the alkaline nature of concretes, steel tendons will be inert in correctly formulated and applied grouts, but at sufficiently high concentrations of certain impurities (such as chloride, nitrate, or sulfide) stress corrosion cracking can occur. Furthermore, electrically coupling high-strength steels to more active metals such as aluminum or zinc (galvanized surface) can result in hydrogen embrittlement of the steel even in correctly formulated grouts. Steel tendons should also be inert in protective greases or waxes, but isolated pockets of water around the tendons or between the strands of tendons might produce damaging corrosion. Galvanic effects should be at a minimum with the greases or waxes because these materials are nonconductors.

Areas in which there is incomplete information on the corrosion of tendon steels are:

1. effect of cathodic polarization, either from internal or external sources, on hydrogen embrittlement,
2. effect of acidifying dilute chloride and sulfate solutions (as would exist in pits) on stress corrosion cracking,
3. general corrosion rate of high-strength steels in dilute aqueous salt solutions and in pure water.

ORNL/NUREG/TM-147
Dist. Category NRC-5

Internal Distribution

1. R. G. Berggren
2. S. E. Bolt
3. R. H. Bryan
4. J. P. Callahan
5. D. A. Canonico
6. S. J. Chang
7. R. D. Cheverton
8. W. E. Cooper
9. J. M. Corum
10. W. B. Cottrell
11. G. G. Fee
12. M. H. Fontana
13. W. R. Gall
14. W. L. Greenstreet
15. R. C. Gwaltney
16. J. F. Harvey
17. M. R. Hill
18. P. P. Holz
19. H. W. Hoffman
20. S. K. Iskander
21. M. A. Karnitz
22. K. K. Klindt
23. Milton Levenson
24. R. E. MacPherson
25. R. W. McClung
26. J. R. McGuffey
27. J. G. Merkle
28. C. A. Mills
29. S. E. Moore
30. F. R. Mynatt
31. F. H. Neill
32. H. A. Pohto (Y-12)
33. G. C. Robinson
34. C. D. St. Onge (Y-12)
35-36. Myrtleen Sheldon
37. G. M. Slaughter
38. C. B. Smith
39. G. C. Smith
40. J. E. Smith
41. I. Spiewak
42. W. J. Stelzman
43. D. G. Thomas
44. H. E. Trammell
45. J. R. Weir, Jr.
46-99. G. D. Whitman
100. Patent Office
101-102. Central Research Library
103. Y-12 Document Reference Section
104-108. Laboratory Records Department
109. Laboratory Records, RC

External Distribution

110-117. Director, Office of Nuclear Regulatory Research, Nuclear Regulatory Commission, Washington, D.C. 20555
118. Director, Reactor Division, Department of Energy, Oak Ridge Operations Office
119. Director, Research and Technical Support Division, Department of Energy, Oak Ridge Operations Office
120-285. Special HSST Distribution
286-589. Given distribution under category NRC-5 (25 copies — NTIS)

☆ U.S. GOVERNMENT PRINTING OFFICE: 1977-748-189/329